Performance Improvement of an Optical Coherence Tomography System by use of an Optical Pupil Slicer

by

Jeffrey Thomas Meade

A thesis
presented to the University of Waterloo
in fulfillment of the
thesis requirement for the degree of
Doctor of Philosophy
in
Systems Design Engineering

Waterloo, Ontario, Canada, 2011

I hereby declare that I am the sole author of this thesis. This is a true copy of the thesis, including any required final revisions, as accepted by my examiners.

I understand that my thesis may be made electronically available to the public.

Acknowledgements

I would like to thank my supervisor, Dr. Arsen R. Hajian, for his invaluable insight into dispersed interferometry and spectroscopy, that of which I have learnt a great deal about in recent years. Also, without his support and hard work this research would not have been possible.

I would like to thank my committee members, Dr. Paul Calamai, Dr. Maud Gorbet, Dr. Glenn Heppler, and Dr. Edward Vrscay, for providing valuable comments on my comprehensive exam, research proposal, and thesis. Also my external examiner, Dr. Kenneth Burch, for accepting this responsibility on such late notice.

I would like to thank Andrew Cenko for so many valuable discussions and support throughout my thesis; from staying up all night watching glue dry to building and aligning complex optical system. Without his help this thesis would truly not have been possible.

I would like to thank Dr. Bradford Behr for his work and dedication to optical slicers, and for helping with the design of the device used in this thesis.

I have had many professors over my university years I would like to thank and acknowledge, but none stand out as much as Dr. Roger Easton of the Center for Imaging Science at the Rochester Institute of Technology. For it was he that inspired me to pursue the study of optics.

I would like to thank my funding sources: the Natural Sciences and Engineering Council of Canada (NSERC), the Ontario Student Assistance Program (OSAP), the Thunder Bay Regional Research Institute (TBRRI)—a research partner of the Thunder Bay Regional Health Sciences Centre (TBRHSC)—and the University of Waterloo (UW). Without their funding and support this research would not have been possible.

Finally I would like to thank my large family and numerous friends for providing moral support throughout the years of my higher education.

Dedication

I dedicate this thesis to my Mother and my Father, who have provided so much love, support, comfort, growth, leadership, and wisdom in my life

I also dedicate this thesis to the memory of my Grandfather and his code of life:

> *–Do all the good you can, in all the ways you can, for as many people as you can, for as long as you can*

Finally I dedicate this thesis to all the fond memories and outstanding people, past and present, at Big Gull Lake

Abstract

Spectral domain optical coherence tomography (SD-OCT) is a dispersed interferometric technology used to obtain tomographic images, typically of tissue for medical applications. OCT is a competing technology with confocal microscopy (CM) and confocal fluorescent microscopy (CFM), which are both used for biopsy imaging for pathology as the gold standard. OCT offers several advantages over CM/CFM: it is able to acquire a full 3D image in a single pass, it requires little or no sample preparation time, and the axial (depth) and lateral (transverse) resolution are not dependent on one another. SD-OCT is limited in imaging depth to a few millimetres due to the quality performance of the spectrograph section of the instrument–that which determines the sensitivity of the SD-OCT system.

In this thesis a design for an SD-OCT system is presented that is suitable for biopsy imaging for pathological studies, i.e. an OCT microscope. The purpose of this system is to provide a fast diagnosis to be made in a surgical environment to reduce the amount of tissue removed from a patient and lower the chance of a returned visit at a later date due to insufficient tissue removal. The secondary purpose of the SD-OCT microscope is to serve as a research testbed system for implementing novel hardware advancements. One such technology, called an optical pupil slicer (OPS), will be implemented in the instrument to improve the depth imaging performance of the SD-OCT system over conventional SD-OCT systems. The OPS is a device that generally improves the performance of a dispersive-type spectrograph by increasing the spectral resolution without a loss in throughput, thereby increasing the sensitivity of the SD-OCT system.

Table of Contents

List of Tables **xv**

List of Figures **xvii**

List of Symbols **xxi**

1 Introduction **1**

1.1 Medical Imaging 1

1.2 Dispersed Interferometry 3

1.3 Motivation 4

1.4 Scope and Thesis Structure 5

2 Background **7**

2.1 Geometrical Optics 7

2.1.1 Snell's Law 8

2.1.2 Paraxial Region 9

2.1.3 Ray Tracing Equations 10

2.1.4 Optical Aberrations 13

2.1.5 Radiometry 17

2.2 Wave Optics 19

2.2.1 The Wave Equation 19

2.2.2 Interference 20

2.2.3 Diffraction 22

2.2.4 Optical Coherence . . . 25
2.3 Statistical Optics . . . 28
2.3.1 Tissue Optics . . . 29
2.3.2 Photon Statistics . . . 31

3 Optical Coherence Tomography **33**
3.1 Theory . . . 34
3.1.1 SD-OCT Signal . . . 35
3.1.2 Limiting Parameters . . . 41
3.2 Custom OCT System . . . 43
3.2.1 Optical Design . . . 43
3.2.2 Results . . . 48

4 Optical Slicers **53**
4.1 Spectroscopy . . . 54
4.2 History of Slicers . . . 66
4.3 Design of the Optical Pupil Slicer . . . 68
4.4 Performance Evaluation . . . 71

5 Slicer in OCT **77**
5.1 Justification . . . 78
5.1.1 System Simulation . . . 79
5.2 Results . . . 85
5.2.1 Physical Implementation . . . 86
5.2.2 Measurement of the Coherence Envelope . . . 92
5.2.3 Zemax Model of the Slicer . . . 100
5.2.4 Updated Simulation . . . 108
5.3 Required Improvements . . . 113
5.3.1 Spectrograph Improvements . . . 114
5.3.2 Slicer Improvements . . . 116
5.3.3 Predicted SD-OCT System Performance . . . 120
5.4 Diffraction Limited Slicer Design . . . 122

6 Conclusions **131**

6.1 List of Contributions 132

6.2 Relevance to Other Fields 133

6.3 Future Work 133

APPENDICES **135**

A Maximum Depth Derivation **137**

B Wiener-Khintchine Theorem **139**

Bibliography **143**

List of Tables

2.1 Description of the Fundamental Aberrations 14
2.2 Optical Properties of Tissue 29

3.1 SD-OCT Simulation Hardware 40
3.2 SD-OCT System Hardware (Interferometer, Spectrograph) 44
3.3 SD-OCT System Hardware (Trapeze) 46
3.4 SD-OCT System Imaging Parameters 49

4.1 Slicer Test Spectrograph Hardware Parameters 62
4.2 Optical Prescription of the 2X Refractive Slicer 69
4.3 Orientations of the 2X Refractive Slicer Elements 70

5.1 SD-OCT Simulation Model Input Variables 81
5.2 Spot Diagram Analysis Spot Size Results from Zemax 105
5.3 Zemax Image Simulation Input Parameters 106
5.4 Zemax Image Simulation Spot Widths Results 106
5.5 Directly Measured Spot Widths 112
5.6 Aberrated Spot Widths from Zemax 114
5.7 Aberration Factors from the Spectrograph and Slicer 114
5.8 Upgraded Spectrograph Custom Lens Prescription 115
5.9 Upgraded Spectrograph and Slicer Image Simulation Spot Widths 117
5.10 Upgraded Aberrated Spot Widths from Zemax 120
5.11 Aberration Factors from Upgraded Spectrograph and Upgraded Slicer . . . 120
5.12 Optical Prescription of the Diffraction Limited Slicer Elements 127
5.13 Orientations of the Diffraction Limited Slicer Elements 128

List of Figures

1.1 Medical Imaging Modalities Comparison Cartoon 2

2.1 Paraxial Region Approximation Error 10
2.2 Solid Angle Approximation Error 18
2.3 Cross Section of the 2D Airy Pattern 25

3.1 Interference Spectra to A-scan Illustration 39
3.2 Cartoon Diagram of SD-OCT System 44
3.3 Cartoon Diagram of Sample Scanning System (Trapeze) 45
3.4 Sensitivity Measurement of the SD-OCT System 50
3.5 Sensitivity Envelope Example of the SD-OCT System 51
3.6 En-Face Image of the 1951 USAF Target Through Chicken Breast 52

4.1 Throughput Efficiency of Collimating Optics 62
4.2 Resolving Power due to Collimating Optics 63
4.3 Quality Factor due to Collimating Optics 63
4.4 Throughput Efficiency of a Slit 65
4.5 Resolving Power of a Slit Spectrograph 65
4.6 Quality Factor of a Slit Spectrograph 66
4.7 Optical Design of the 2X Refractive Slicer 69
4.8 Focused Spot Images With and Without the Slicer 72
4.9 Throughput Efficiency and the Vertically Binned Spot Profiles 74
4.10 Atomic Line Emission Spectra With and Without the Slit 75

5.1 SD-OCT System Model Simulation Focal Plane Functions 82
5.2 SD-OCT System Model Simulation Pinhole Image 83
5.3 SD-OCT System Model Simulation Coherence Envelopes 84
5.4 SD-OCT System Model Simulation Coherence Envelopes Ratio 85
5.5 Physical Implementation Diagram of the Slicer in SD-OCT 87
5.6 Reference Spectra for for the Slicer and Non-Slicer 89
5.7 Slicer Alignment Procedure Example—Aligned Spectrum 91
5.8 Slicer Alignment Procedure Example—Unaligned Spectra 92
5.9 Aligned Slicer in SD-OCT Interference Spectrum Selection 93
5.10 Raw and Processed Spectra from the Non-Sliced Spectrograph 95
5.11 Raw and Processed Spectra from the Sliced Spectrograph 96
5.12 Spectral Coherence Envelopes for the SD-OCT Spectrograph 97
5.13 Gaussian Fitted Coherence Envelopes and Ratio Comparison 98
5.14 Spot Diagram 2X Slicer (800 nm) 102
5.15 Spot Diagram 2X Slicer (850 nm) 102
5.16 Spot Diagram 2X Slicer (900 nm) 103
5.17 Spot Diagram Non-Slicer (800 nm) 103
5.18 Spot Diagram Non-Slicer (850 nm) 104
5.19 Spot Diagram Non-Slicer (900 nm) 104
5.20 Zemax Image Simulation Input Uniform Circle Image 107
5.21 Zemax Image Simulation Results for Slicer and Non-Slicer 107
5.22 Vertically Binned Aberrated Images from Zemax 108
5.23 Updated Pinhole Image from IDL 110
5.24 Updated Coherence Envelopes and Ratio Comparison from IDL 111
5.25 Directly Imaged Spots of Non-Slicer and Slicer 112
5.26 Vertical Binned Profiles of the Directly Imaged Spots 112
5.27 Upgraded Spectrograph Custom Lens Optical Design 115
5.28 Upgraded Spectrograph & Slicer Simulated Images from Zemax 118
5.29 Vertically Binned Aberrated Images from Upgraded Spectrograph & Slicer 119

5.30 Upgraded Pinhole Image from IDL 122
5.31 Upgraded Coherence Envelopes and Ratio Comparison from IDL 123
5.32 Optical Design of the Diffraction Limited Slicer 125
5.33 3D Shaded Model of the Diffraction Limited Slicer 127
5.34 Simulated Perfect Images for the Reflective and Refractive 2X Slicer 128
5.35 Perfect Spot Diagrams for the Reflective and Refractive 2X Slicer 129

List of Symbols

2Θ	Angle separation between two plane waves used to create a transmission grating. Section 2.2.3
$\bar{u}$	Paraxial chief ray angle from the optical axis. Section 2.1.3
$\bar{y}$	Paraxial chief ray height from the optical axis. Section 2.1.3
$\cdot$	Vector dot product operator
$\Delta\Lambda$	The FWHM bandwidth of the system light source. Section 3.1.2
$\Delta\lambda$	The wavelength separation between adjacent pixels. Section 3.1.1
$\delta\lambda$	The FWHM bandwidth of a pixel, and the spectral resolution. Section 3.1.1
$\delta\lambda_j$	The spectral bandpass function for the j^{th} pixel. Section 3.1.1
$\Delta\phi$	Phase difference between two optical fields. Section 2.2.2
Δd	OPD between two optical fields. Section 2.2.2
Δx	The lateral resolution. Section 3.1.2
Δz	The axial resolution. Section 3.1.2
$\delta(\cdot)$	The Dirac delta function
ϵ	Dielectric material variable. Section 2.2.1
ϵ_0	The permittivity constant of free space. Section 2.2.1
ϵ_r	Relative dielectric material variable. Section 2.1.1
η	Quantum efficiency of a detector. Section 2.3.2
Γ	The mutual coherence function. Section 2.2.4

γ The normalized mutual coherence function. Section 2.2.4

λ Wavelength of light

λ_0 Centre wavelength of a bandpass function

λ_B The blaze wavelength of a diffraction grating. Section 2.2.3

λ_c Wavelength of light in a vacuum. Section 2.1.1

λ_j The centre wavelength for the j^{th} pixel. Section 3.1.1

$\langle\cdot\rangle_e$ The ensemble average given by $\langle z(t)\rangle_e = \lim_{N\to\infty}\left(\frac{1}{N}\sum_{j=1}^{N} z_r(t)\right)$

$\langle\cdot\rangle_t$ The time average operator given as $\langle z(t)\rangle_t = \lim_{T\to\infty}\left(\frac{1}{2T}\int_{t-T}^{t+T} z(t')dt'\right)$

μ Magnetic material variable. Section 2.2.1

μ_0 The permeability constant of free space. Section 2.2.1

μ_a Absorption coefficient. Section 2.3.1

μ_r Relative magnetic material variable. Section 2.1.1

μ_s Scattering coefficient. Section 2.3.1

μ_t Total attenuation coefficient. Section 2.3.1

Ω Solid angle. Section 2.1.5

ω Optical angular frequency. Section 2.1.1

Ω_{EP} Solid angle that the EP subtends on an observation point (typically focal point). Section 2.1.5

Ω_s Solid angle that a source subtends upon an optical system. Section 2.1.5

$\overline{\varepsilon}_H$ Average radial error in position of the image point. Section 2.1.4

$\overline{\varepsilon}_\vartheta$ Average angular error in position of the image point. Section 2.1.4

Φ Tilt angle of a transmission grating during exposure. Section 2.2.3

ϕ_s Scattering azimuthal angle. Section 2.3.1

ϕ_Ω Azimuthal angle component of a solid angle. Section 2.1.5

Π Aperture transmission function. Section 2.2.3

Ψ The cross-spectral density function. Section 2.2.4

ψ The spectral coherence envelope. Section 2.2.4

ρ Normalized radius of an object point in the exit pupil. Section 2.1.4

τ Time of flight difference between two optical fields. Section 2.2.2

θ Optical angle measured either from the optical axis or a surface normal

θ_B The blaze angle of a diffraction grating. Section 2.2.3

θ_i Incident angle. Section 2.1.1

θ_L The Littrow angle. Section 2.2.3

θ_s Scattering polar angle. Section 2.3.1

θ_t Transmitted angle. Section 2.1.1

θ_Ω Polar angle component of a solid angle. Section 2.1.5

$\times$ Vector cross product operator

$\underline{u}$ Paraxial marginal ray angle from the optical axis. Section 2.1.3

$\underline{y}$ Paraxial marginal ray height from the optical axis. Section 2.1.3

ε_H Radial error in position of the image point. Section 2.1.4

ε_ϑ Angular error in position of the image point. Section 2.1.4

ε_{x_i} Error in position of the image point along the X-axis. Section 2.1.4

ε_{y_i} Error in position of the image point along the Y-axis. Section 2.1.4

φ Optical power of a surface. Section 2.1.3

φ_L Optical power of a real lens. Section 2.1.3

ϑ Polar angle of an object point in the exit pupil. Section 2.1.4

$\vec{\mathcal{E}}$ The real part of the complex electric field vector. Section 2.2.2

$\vec{\nabla}$ The gradient vector operator given as $(\frac{\partial}{\partial x}, \frac{\partial}{\partial y}, \frac{\partial}{\partial z})$ in Cartesian coordinates. Section 2.2.1

$\vec{B}$ The complex magnetic displacement vector. Section 2.2.1

$\vec{D}$ The complex electric displacement vector. Section 2.2.1

$\vec{E_0}$ The complex amplitude vector of an electric field. Section 2.2.1

$\vec{E_i}$ Complex interference electric field vector. Section 2.2.2

$\vec{E}$ The complex electric field vector. Section 2.2.1

$\vec{H}$ The complex magnetic field vector. Section 2.2.1

$\vec{k}$ The wavenumber vector. Section 2.2.1

$\vec{r}$ Positional coordinate vector. Section 2.2.1

Ξ The étendue of an optical system. Section 2.1.5

* The complex conjugate operator

A An A-scan signal. Section 3.1.1

A_s Surface area of a source. Section 2.1.5

A_{2D} Surface area of a 2D object. Section 2.1.5

A_{3D} Surface area of a 3D object. Section 2.1.5

A_{EP} Surface area of the entrance pupil. Section 2.1.5

B The average spectral reflectivity. Section 3.1.1

C Period of constructive interference in a transmission grating. Section 2.2.3

c Velocity of light in a vacuum. Section 2.1.1

C_p Projected period of constructive interference in a transmission grating. Section 2.2.3

d Distance light travels. Section 2.1.3

D_a Diameter of a circular aperture stop. Section 2.2.3

D_b Diameter of a beam incident on a diffraction grating. Section 4.1

d_g Groove spacing in a diffraction grating. Section 2.2.3

d_L Thickness of a real lens. Section 2.1.3

d_o Distance from an object to an observation point. Section 2.1.5

d_r Path length travelled through the reference arm. Section 3.1.1

d_s Path length travelled through the sample arm. Section 3.1.1

D_{EP} Diameter of the entrance pupil of an optical system. Section 2.1.3

d_{EP} Distance from an object to the entrance pupil. Section 2.1.5

D_{sl} Diameter of the spectrograph source collimating lens. Section 4.1

D_{sp} Diameter of a sphere. Section 2.1.5

D_s Diameter of the collimated source beam in the spectrograph. Section 4.1

D_{XP} Diameter of the exit pupil. Section 2.1.4

E The complex electric field scalar. Section 2.2.3

$f/\#$ F-number of an optical system. Section 2.1.3

f_L Focal length of a real lens. Section 2.1.3

f_{cl} Focal length of the spectrograph camera lens. Section 4.1

f_{sl} Focal length of the spectrograph source collimating lens. Section 4.1

g Anisotropy factor. Section 2.3.1

H Normalized radius of an image point in the focal plane. Section 2.1.4

h Paraxial ray height from the optical axis. Section 2.1.3

h_i Height of an image measured from the optical axis. Section 4.1

h_o Height of an object measured from the optical axis. Section 4.1

I Optical intensity. Section 2.2.2

i Imaginary number representing $\sqrt{-1}$. Section 2.2.1

I_0 Incident optical intensity. Section 2.3.1

I_i Optical interference intensity. Section 2.2.2

I_j The total optical intensity in the j^{th} pixel. Section 3.1.1

I_r Intensity of the reference arm. Section 3.1.1

I_s Intensity of the sample arm. Section 3.1.1

J The number of pixels

J_1 Bessel function of the first kind, first order. Section 2.2.3

k Wavenumber. Section 2.1.1

k_i Incident wavenumber. Section 2.1.1

k_t Transmitted wavenumber. Section 2.1.1

L The radiance of an optical system. Section 4.3

m Diffraction order number. Section 2.2.3

n Index of refraction. Section 2.1.1

N_{res} The number of independent resolution elements. Section 4.1

O_L Lagrange invariant. Section 2.1.3

$O_{1,2}$ Optical invarient for any 2 paraxial rays. Section 2.1.3

P The mean number of photons. Section 2.3.2

Pr Probability density function

Q Quality factor for a dispersive spectrograph. Section 4.1

R Spectral resolving power. Section 4.1

R_p Radius of curvature of the paraxial wavefront. Section 2.1.4

R_s Radius of curvature of an optical surface. Section 2.1.3

r_s The radius of a circular source object. Section 4.1

R_{max} The maximum resolving power of a diffraction grating. Section 4.1

S The optical power spectrum. Section 2.2.4

T Throughput efficiency. Section 4.1

t Independent variable for time

U A random number uniformly distributed from 0 to 1. Section 2.3.1

u Paraxial ray angle from the optical axis. Section 2.1.2

V Visibility of interference. Section 2.2.2

v Velocity of light in a medium. Section 2.1.1

W Wavefront error coefficient. Section 2.1.4

w Width of the central lobe in the Airy pattern. Section 2.2.3

w_s The half-width of a slit. Section 4.1

x_B Position of the blaze wavelength in the image plane. Section 4.1

x_i X-coordinate independent variable in the image plane. Section 2.1.4

x_p X-coordinate independent variable in the pupil plane. Section 2.1.4

y_i Y-coordinate independent variable in the image plane. Section 2.1.4

y_p Y-coordinate independent variable in the pupil plane. Section 2.1.4

z The physical delay relative to the zero OPD location. Section 3.1.1

z_s Reflection depth location in the sample arm. Section 5.1.1

z_{max} Maximum unaliased imaging depth. Section 3.1.1

DOF Depth of focus. Section 3.1.2

EP Entrance pupil. Section 2.1.3

FT Fourier Transform

FWHM Full-width at half-maximum value

NA Numerical aperture for a cone of light. Section 2.1.3

OAD Off-axis distance. Section 5.4

OCT Optical coherence tomography

OPD Optical path difference

OPS Optical pupil slicer

RMS Root mean square

SD-OCT Spectral domain optical coherence tomography

SNR Signal-to-noise ratio. Section 2.3.2

SNR_{OCT} SNR defined in OCT is the square of the signal divided by the noise variance.

WSF Working slicing factor. Section 5.3

XP Exit pupil. Section 2.1.3

Chapter 1

Introduction

Optical coherence tomography (OCT) is an imaging modality based fundamentally on interferometry and spectroscopy. It has numerous applications in various areas, however the use of OCT is widely used for medical imaging to produce high-resolution 3D images of tissue. A significant advantage of an OCT instrument to other high-resolution medical optical imaging devices is that OCT is able to image several millimetres into tissue and still provide cellular resolution (< 10 μm). Despite the relatively large penetration depth of OCT, it is still a limiting factor of all OCT systems—this limitation is often dependent on the sensitivity of the OCT instrument [18].

The stated problem that we attempt to solve in this thesis is one of increasing the penetration depth and image quality of a specific implementation of an OCT instrument, called a spectral domain OCT (SD-OCT) instrument, by increasing the sensitivity beyond conventional techniques. An optical device known as an optical pupil slicer (OPS) is able to improve the quality of a dispersive spectrograph fundamentally. This fundamental improvement manifests itself as a sensitivity increase in SD-OCT because the sensitivity in SD-OCT is limited by the quality of the spectrograph section of the instrument [18, 35, 38, 39, 55, 63]. The topic of this thesis is to describe the nature of the problem regarding the sensitivity of SD-OCT and then attempt to fundamentally improve the instrumentation hardware by implementing the OPS.

1.1 Medical Imaging

The goal of medical imaging is to produce images for diagnostic or screening purposes to aid in the process of patient care and treatment. Image content may range from as large as a full body to as small as organelles. Organelles are multiple membrane sub-cellular components that as a whole make up the entirety of a eukaryote cell (a cell in

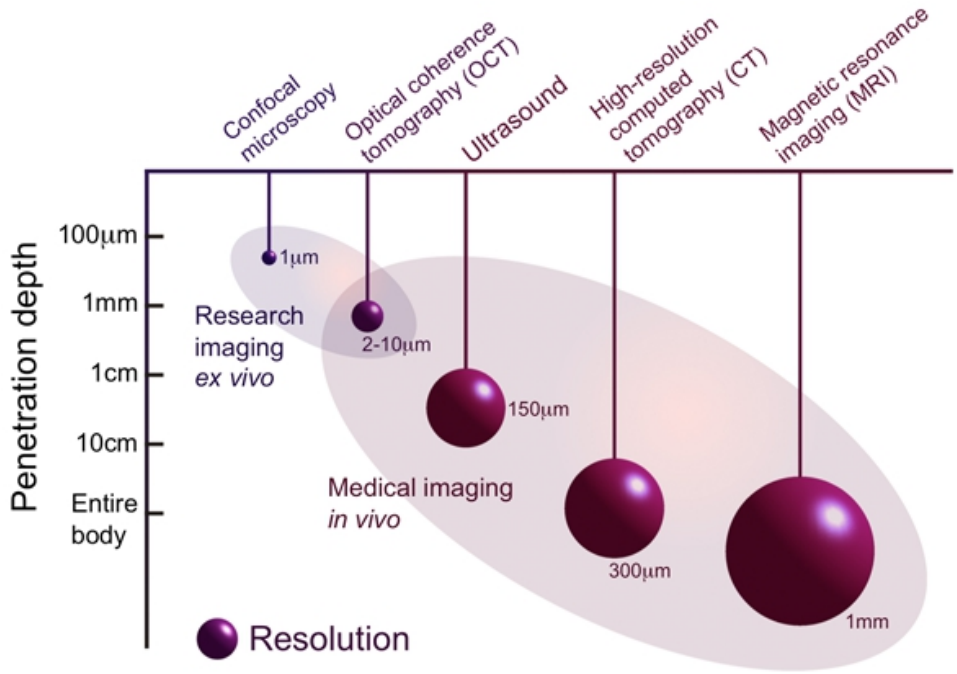

Figure 1.1: A cartoon figure showing the imaging spatial resolution versus the imaging depth for confocal microscopy, optical coherence tomography, ultrasound, computed tomography, and magnetic resonance imaging. Image taken from [46].

which the DNA is segregated from the rest of the cellular constituents) [40]. All animal and plant life are composed of eukaryote cells, which vary in size from about 10-100 μm. Various technologies exist which produce medical images and are based on different physical principles. Examples of such technologies and methods include, but are not limited to, magnetic resonance imaging (MRI), x-ray (XR), computerized (automated) tomography (CT or CAT), positron emission tomography (PET), single photon emission computerized tomography (SPECT), ultrasound (US), confocal (fluorescence) microscopy (CM or CFM), and optical coherence tomography (OCT). The primary imaging modality of interest for this thesis is OCT. A summary of a few imaging characteristics can be seen in fig. 1.1.

A general trend in medical imaging is a trade off between resolution and penetration depth, i.e. if one wishes to achieve deeper imaging, spatial resolution is decreased. Medical imaging instruments typically are designed and chosen to operate in a fixed region of resolution-depth parameter space, the restriction typically being due to the physical principles of instrument operation. Therefore medical imaging devices are usually very task specific and each technology is usually used for very specific purposes.

Optical coherence tomography is a specific method of obtaining full 3D tomographic images using optical electromagnetic radiation. OCT may be used as a medical imaging

technology that may be characterized by several features such as being able to obtain cellular spatial resolution, may be used in non-contact operation, relatively fast operation time, does not use harmful ionizing radiation, and is able to achieve several millimetres of imaging depth. OCT is often described as being the optical equivalent of ultrasound since the imaging characteristics are very similar, e.g. they both record reflectivity as a function of depth for a single iterative scan.

OCT is a relatively new medical imaging modality, with the first papers being published in the late 1980's and early 1990's [18]. OCT has had applications primarily in ophthalmology, dermatology, and haematology due to its ability to acquire cellular resolution images in nearly real-time and being able to operate in both *in vivo* and *ex vivo* [12, 17, 18, 22, 30, 48]. So far the largest application of OCT is retinal imaging since it is able to image all layers of the retina with cellular resolution over a large field of view in non-contact operation, however OCT has tremendous potential in other applications such as general histology tissue imaging [10, 18, 25, 26, 45].

1.2 Dispersed Interferometry

Dispersed optical interferometry has its origins in the field of astronomy [19, 20, 21, 58]. An instrument called the dispersed Fourier transform spectrograph (dFTS) was invented in the mid 1990's and was used to determine the radial velocity of stellar targets by measuring the stellar spectra [5, 31, 32, 33]. The dFTS instrument is essentially a standard Fourier transform spectrograph based on the conventional Michelson design, but with a standard dispersive-based spectrograph used to record the output. The dFTS was shown to improve the signal-to-noise ratio (SNR) of measured spectra over a regular FTS by a factor proportional to the square root of the resolving power of the back-end spectrograph, which can be several thousand easily.

The first optical coherence tomography systems were essentially Fourier transform spectrographs and are known as time-domain OCT systems (TD-OCT). At the same time the dFTS instrument was invented in the mid 1990's a new method of OCT was also invented based on an instrument design similar to the dFTS in which the output spectrum is measured by a dispersive-based spectrograph. These OCT instruments record a depth scan by taking the Fourier transform of the measured spectrum, and hence is called Fourier-domain OCT (FD-OCT); the specific implementation of FD-OCT by using a dispersive-based spectrograph is called spectral-domain OCT (SD-OCT). SD-OCT is extremely similar to the dFTS with the fundamental difference being the delay-induced mirror is replaced by a sample object. SD-OCT reports SNR improvements over TD-OCT with factors proportional to the number of detector elements in the back-end spectrograph [13, 14, 18, 39]. There are definite parallels between dispersed optical interferometry systems in astronomy and

SD-OCT, and it can be seen that SD-OCT is formally a dispersed optical interferometry system applied towards medical imaging.

1.3 Motivation

OCT fills a nice gap between confocal microscopy and ultrasound in terms of imaging performance, as depicted in fig. 1.1. Confocal (fluorescent) microscopy has historically been used as a microscope technology to image prepared tissue samples for pathological applications. These images are often considered a gold standard because of the high spatial resolution CM/CFM is able to provide. Despite the imaging advantages of CM/CFM the process of acquiring an image can be quite slow due to lengthy sample preparation (freezing, cutting, staining and/or fluorescent dying), and the imaging operation time is lengthy due to an iterative depth slice selection procedure.

OCT offers several advantages over confocal (fluorescence) microscopy such as being able to acquire full depth imaging for each point scanned across a sample, requires very little preparation time, and is still able to provide cellular resolution, thereby coming close to gold standard imaging. At the current time of the writing of this thesis there are very few commercial OCT based microscopes that are designed specifically for imaging tissue in a manner similar to CM/CFM.

Because of OCT's short sample preparation time and fast imaging operation time, such a microscope could be very useful in a clinical surgery type environment where biopsies are being taken. Ordinarily many tissue samples are taken in a surgical biopsy procedure which may cause irreparable damage to a patient. These tissue samples are then prepared and imaged using CM/CFM and a medical professional then examines these images and determines the diagnosis. This procedure may take up to 1-2 weeks at which time the patient may need to return for additional surgery if the diagnosis was dubbed inconclusive due to a quantitative lack of tissue samples. An instrument that is able to image each tissue sample at "silver standard" level quality as it is extracted from the patient could be extremely useful in the surgery room so that a high quality pre-diagnosis can be made during the surgical procedure. The impact would be less healthy tissue would be removed from the patient and the possibility of returning for additional surgery may be minimized.

One of the stated goals for this research is to construct an OCT based microscope that is suitable for biopsy imaging for pathology in a surgical environment, that of which there is a limited commercial market. The topic of the thesis is to incorporate a unique technology into the OCT microscope system to boost the performance beyond that of conventional OCT, thereby closing the gap between CM/CFM and OCT and raising the imaging quality close to that of the gold standard.

1.4 Scope and Thesis Structure

This thesis aims to solve a very specific problem: increasing the sensitivity of an SD-OCT instrument while maintaining maximal light throughput in order to increase the image quality and depth penetration of the OCT image. The topics and material presented in this thesis provide enough background theory relevant to understand the problem and solution, namely sensitivity in SD-OCT, dispersive spectroscopy and interferometry, and optical imaging. A full description of the entire theory and physics of optical coherence tomography, dispersive spectroscopy, and interferometry are beyond the scope of this thesis and further information on the subjects are provided in the references. Selected theory and physics from optics and OCT are presented in the framework of the research presented in this thesis.

The rest of the chapters in this thesis, and the content within, is structured as follows: Chapter 2 provides background theory used to understand and explain OCT on a fundamental level, the OPS, and the results of implementing the OPS in the SD-OCT system. If the reader is already very familiar with geometrical optics and ray tracing, and more advanced topics such as interference, diffraction, and optical coherence, then chapter 2 may be quickly glossed over for brevity. Chapter 3 introduces the theory and mode of operation of SD-OCT and also presents the design and results from the SD-OCT system microscope constructed and used in this research. Chapter 4 begins with a discussion on dispersive spectroscopy relevant to the SD-OCT system and develops into discussions on optical slicers. The design of the optical pupil slicer is presented and performance results and characteristics are shown. Chapter 5 is the heart of the thesis where expected improvements in the SD-OCT system due to the OPS are presented, followed by how the OPS was implemented and the performance results of the SD-OCT system with the OPS. The results show that the performance of the OPS are not good enough to make an improvement, and so the remainder of chapter 5 discuss the shortcomings of the OPS and necessary improvements to the SD-OCT system and the OPS. The thesis finishes with a conclusion of the results in chapter 6.

Chapter 2

Background

In this chapter the fundamental theory relevant to the remainder of this thesis is presented. The topics presented in this chapter are broken into two classifications: geometrical optics, and wave optics. Geometrical optics is a simplification of the more advanced topics of optical physics and serves as a useful descriptor of how optical systems behave without requiring knowledge of the intricate details of the full physical description of light. The subjects of ray tracing, aberrations, and radiometry will be presented under the framework of geometrical optics with several fundamental definitions such as focal length, the optical invariant, and numerical aperture. Wave optics is a more complete theory of optical physics and is able to properly explain advanced phenomena. The topic of wave optics is important to understand in this thesis because the subjects of interference, diffraction, and coherence are unable to be explained by geometrical optics.

If the reader is already familiar with the fundamentals of optical theory and especially the topics of interference, diffraction, and coherence, then this chapter can be skipped for brevity and the reader may proceed directly to chapter 3. This chapter serves as a basis for further developments of the theory more applicable to the research in this thesis and later topics will be referred to different portions of this chapter.

2.1 Geometrical Optics

Geometrical optics, or ray optics, is a simplification of the general wave treatment of optics in order to describe wave propagation in terms of rays which are perpendicular to the phase front, or the normal vector. Most optical phenomena may be described as such, and to first order the light path through an optical system can be described with great detail using the model of rays. Geometrical optics provides a powerful engineering model of optics because of its simplicity but overall completeness and ease of implementation into software, e.g.

ray tracing programs such as ZEMAX®. Geometrical optics does not include, or rather is incapable, of describing diffraction and interference properly, however elements such as a diffraction grating can be modelled using ray optics. In this section the general ray optics model will be presented, the paraxial region will be defined and the paraxial ray tracing equations will be presented. Moving beyond the paraxial region induces higher order effects that cause rays to deviate from the perfect paraxial case; these are known as optical aberrations and some basic aberration theory will be presented. The measurement of electromagnetic radiation in optics is known as radiometry, which is large enough a field to be in its own section, however since it is highly geometric in nature and only a few basic results will be presented, it is appropriate to classify it under an extension of ray optics.

2.1.1 Snells Law

Deriving from the boundary conditions from Maxwell's equations describing a propagating plane wave, the angular description of the propagation of the plane wave upon transmitting through an optical medium is given by Snell's law,

$$k_i \sin(\theta_i) = k_t \sin(\theta_t), \tag{2.1}$$

where k_i and k_t are the incident and transmitted wavenumbers, and θ_i and θ_t are the incident and transmitted angles as measured from the surface normal of the optical medium the light is interacting with [8]. The wavenumber may be given by,

$$k = \frac{2\pi\sqrt{\epsilon_r(\omega)\mu_r(\omega)}}{\lambda_c}, \tag{2.2}$$

where λ_c is the wavelength of light in a vacuum and the material is described by the dielectric and magnetic variables, $\epsilon_r(\omega)$ and $\mu_r(\omega)$ respectively, that depend on the optical angular frequency, ω. The speed of light in a material, v, may be given as,

$$v = \frac{c}{\sqrt{\epsilon_r(\omega)\mu_r(\omega)}}, \tag{2.3}$$

where the speed of light in a vacuum is given as, $c \simeq 3 \times 10^8$ m/s. The term in the denominator of eqn. 2.3 is called the index of refraction and is commonly denoted by $n(\omega)$. The index dependence on the optical angular frequency means that light will travel at different speeds in a material, this phenomena is known in optics as dispersion. Since the

speed of any travelling wave is given by the frequency multiplied by the wavelength, and since the speed of light in a medium is always less than the speed of light in a vacuum ($v < c$), and the optical frequency is constant (energy must be conserved), this implies the wavelength must decrease by a factor given by the index, and hence the presence of the material parameters in the numerator of eqn. 2.2. Substituting the definition for wavenumber into Snell's law, an alternative version is presented,

$$n_i(\omega)\sin(\theta_i) = n_t(\omega)\sin(\theta_t), \tag{2.4}$$

where $n_i(\omega)$ and $n_t(\omega)$ are the indicies of refraction of the incident material and the transmitted material respectively. This representation of Snell's law is the fundamental equation in which all of geometrical optics may be derived from, and is also known as the law of refraction. A mirror may be modelled by eqn. 2.4 by substituting in $n_t(\omega) = -n_i(\omega)$ whereby the result $\theta_t = \theta_i$ arises which is the law of reflection: reflected angle equals incident angle.

2.1.2 Paraxial Region

The law of refraction in eqn. 2.4 is sufficient to describe the transmission and reflection of rays through an optical system, however the computation is somewhat complex due to the sin functions. When the angles, θ_i and θ_t are small, a small angle approximation may be substituted into eqn. 2.4 to define the paraxial law of refraction,

$$n_i(\omega)u_i = n_t(\omega)u_t, \tag{2.5}$$

where u_i and u_t are the paraxial small angles defined by $u = \theta \simeq \sin(\theta)$. In the small angle approximation the tangent angle can also be used to approximate the sin of the angle, in which case the paraxial angle, u, may be defined as

$$u = \theta \simeq \sin(\theta) \simeq \tan(\theta). \tag{2.6}$$

Often the approximation of $\sin(\theta) \simeq \tan(\theta)$ is used in paraxial optics because the tangent angle for right triangles is defined as the height divided by the base. In optical ray tracing the height is often the height location of the ray at any point in an optical system and the base is the distance from the height location to where the ray crosses the optical axis. To visualize the error associated with the paraxial approximation the relative error may be plotted as a function of actual angle, θ; this is seen in fig. 2.1. It can be seen that for errors less than 1.5% the paraxial appoximation should only be used for angles less than 10°. An error of 1.5% is quite significant when rays propagate long distances.

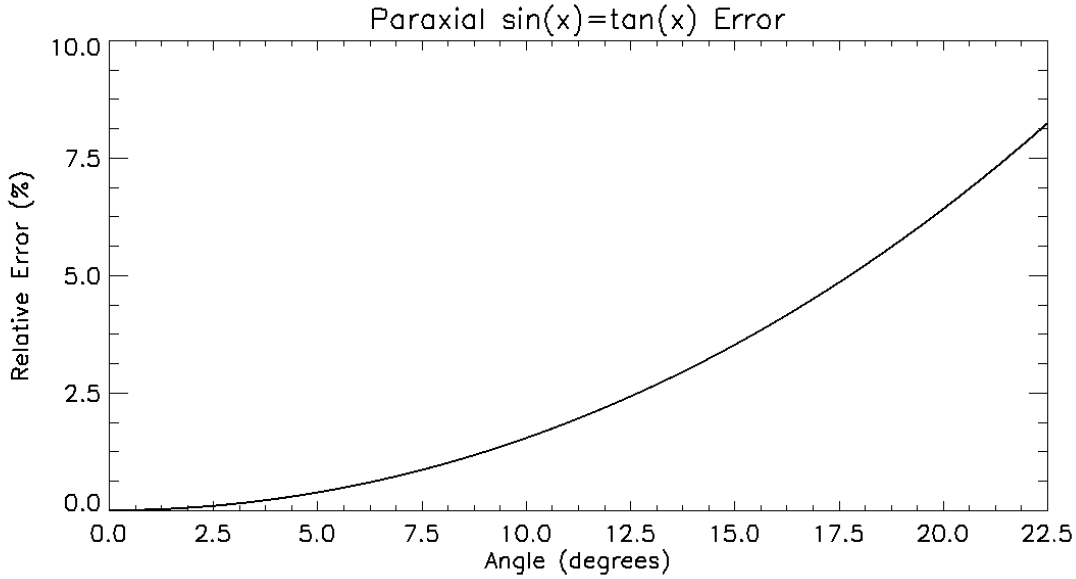

Figure 2.1: A plot of the relative error of assuming $\tan(\theta) = \sin(\theta)$ as a function of θ.

2.1.3 Ray Tracing Equations

A spherical lens is an optical element usually made of a certain type of glass, e.g. N-BK7, that has at least one circularly curved surface. Given the index of refraction of the glass, $n_g(\omega)$, and the medium immediately before the lens, $n_i(\omega)$, and the radius of curvature of the surface, R_s, the power of the optical surface, φ, may be defined as [29]

$$\varphi(\omega) = \frac{n_g(\omega) - n_i(\omega)}{R_s}. \tag{2.7}$$

It is seen that the power of an optical surface is dependent on the optical frequency because the index of refraction is dependent on the optical frequency. A lens has some real thickness, d_L, and has two optical surfaces. The total power of the lens is a combination of the powers of the two surfaces, φ_1 and φ_2, and the lens thickness and is defined as [29]

$$\varphi_L(\omega) = \varphi_1(\omega) + \varphi_2(\omega) - \varphi_1(\omega)\varphi_2(\omega)\frac{d_L}{n_g(\omega)}. \tag{2.8}$$

The focal length of the lens is given as the inverse optical power,

$$f_L(\omega) = \frac{1}{\varphi_L(\omega)}. \tag{2.9}$$

The fact that the focal length depends on the optical frequency means that light of different wavelengths will come to a focus as different points. This is known as chromatic aberration and will be discussed more in section 2.1.4. Perhaps the most important aspect of geometrical optics is its ability to trace a ray through an optical system. There are two fundamental ray tracing equations: the refraction equation, and the transfer equation. The refraction equation is derived from eqns. 2.5 and 2.7, while the transfer equation is derived from simple trigonometry [29]. The ray tracing equations are stated as,

$$n_2(\omega)u_2 = n_1(\omega)u_1 - h_1\varphi_{1,2}(\omega), \tag{2.10}$$

and

$$h_2 = h_1 + u_2 d, \tag{2.11}$$

where u_2 is the paraxial angle upon transmitting through a surface with power $\varphi_{1,2}$, the height of the ray from the centre of the optical axis is given as h_1, u_1 is the paraxial angle of the ray incident on the optical surface, and n_1 and n_2 are the indicies of refraction of the material before and after refraction. The second equation determines the height of the ray after travelling some distance, d, with paraxial angle u_2 with initial height h_1. If the optical surface has some focal length, f_s, and the initial ray is parallel to the optical axis ($u_1 = 0$) with an initial height h_1, then the ray will be refracted and have zero height ($h_2 = 0$) after travelling a distance equal to the focal length multiplied by the index of refraction ($d = n_2(\omega)f_s$), also known as the optical distance. This is the classic condition of collimated light entering a lens and coming to a focus at the focal point. Although the above example is very simple, any ray with appropriate starting conditions may be traced through an optical system with a high degree of complexity. The process of tracing a ray through a complex optical system is very repetitive and only relies on eqns. 2.10 and 2.11 with the power of the surface being defined by eqn. 2.7, and hence is a very good job for a computer to do. Ray tracing software packages, such as ZEMAX®, are used to design and model optical systems [64].

The Optical Invariant

Optical systems are of finite size and therefore they are limited in the rays which are allowed to pass through them. An aperture is an opening in which rays may pass through unblocked. The limiting aperture in an optical system is called the stop. The entrance pupil (EP) is the image of the stop in object space (in front of the optical system) and

the exit pupil (XP) is the image of the stop in image space (after the optical system). The location and size of the EP and XP may be found by using the standard ray tracing equations (eqns. 2.10 and 2.11).

Two types of rays may be traced through the system in order to describe the image at any location. These two rays are called the marginal ray and the chief ray [29]. The marginal ray begins on the optical axis at the object location and travels to the edge of the entrance pupil and also goes through the edge of the system stop and exit pupil. The image locations are defined as whenever the marginal ray crosses the optical axis. The marginal ray also defines the maximum angle at which rays may enter the optical system starting along the optical axis. The marginal ray angle and height are given by $\underline{u}$ and $\underline{y}$. The chief ray begins at the height of the object and goes through the centre of the entrance pupil and also goes through the centre of the system stop and exit pupil. The image heights are defined as the height of the chief ray whenever the marginal ray crosses the optical axis. The chief ray angle and height are given by $\bar{u}$ and $\bar{y}$.

The field of view (FOV) of an optical system is defined as the full angular range that is seen by the entrance pupil, which is $2\bar{u}$. Often the reverse problem is assigned in which the detection area is the limiting factor. In this case a reverse chief ray is traced starting at the detector height and passing through the centre of the exit pupil. The FOV is then found to be twice the emerging chief ray angle out of the front of the optical system, $2\bar{u}'$.

The rays passing though an optical system are constrained given the parameters of the optical system (focal lengths, lens separations, lens sizes, apertures, etc). Given two rays in an optical system an invariant, or constant, of the system is found to be

$$O_{1,2}(\omega) = n(\omega)\left(u_1 h_2 - u_2 h_1\right), \tag{2.12}$$

where u_1 and h_1 are the paraxial angel and height of the first ray, and u_2 and h_2 are the paraxial angle and height of the second ray at any location in an optical system with an index of refraction $n(\omega)$ [29]. If the two rays in eqn. 2.12 are the marginal and chief rays then the optical invariant is known as the Lagrange invariant given as,

$$O_L(\omega) = n(\omega)\left(\bar{u}\underline{y} - \underline{u}\bar{y}\right). \tag{2.13}$$

The optical or Lagrange invariant is constant at any axial location throughout the optical system. The Lagrange invariant will be seen again in section 2.1.5 in a different form. As stated the invariant is constant, however in practise it can degrade due to losses in the optical system, such as focal ratio degradation. An example of this would be passing

light through an optical fibre if the input FOV was smaller than the acceptance and exit angle.

Numerical Aperture and F/#

Perhaps the most widely used term in optics is the f-number (f/#), or numerical aperture (NA) describing the rays in the system. These terms are also very commonly used to describe a lens, e.g. an f/2 lens, or a lens with NA=0.5. The f-number is defined formally as the ratio of the focal length of an optical system to the diameter of the entrance pupil when the object is at infinity,

$$f/\#(\omega) = \frac{f_L(\omega)}{D_{EP}}. \tag{2.14}$$

For a single lens the lens itself serves as the system stop and therefore the entrance and exit pupil are located at the lens and the diameters are equal to the lens diameter. In this case the f-number is simply the focal length divided by the diameter of the lens. A more practical way to describe the rays is to use the numerical aperture (NA), which by definition is the index of refraction of the optical space in which the rays are being described, $n(\omega)$, multiplied by the sin of the marginal ray angle, θ_m,

$$\mathrm{NA}(\omega) = n(\omega)|\sin(\theta_m)| \simeq n(\omega)|\underline{u}|, \tag{2.15}$$

where the small angle paraxial approximation may be used. If a lens is assumed to have zero thickness and placed in air then the numerical aperture and f-number are related by

$$f/\#(\omega) = \frac{1}{2\,\mathrm{NA}(\omega)}. \tag{2.16}$$

2.1.4 Optical Aberrations

The paraxial region and the paraxial ray tracing equations describe an ideal optical system, such as a lens whereby all the rays come to a focus at a single point. The paraxial region makes use of the small angle approximation in Snell's law, but an approximation always has some error associated with it, as was shown in fig. 2.1. The proper way to trace a ray through a real lens is to use the full form of Snell's law without any approximations. The location of the traced real ray will be different than the location of the traced paraxial ray. This difference is called an optical aberration because it is a deviation of an ideal result.

Fundamental Aberrations		
Name	**Term Description**	**Order**
Defocus	W_{020}	1
Tilt	W_{111}	1
Spherical	W_{040}	3
Coma	W_{131}	3
Asigmatism	W_{222}	3
Distortion	W_{311}	3
Field Curvature	W_{220}	3

Table 2.1: Description of the Fundamental Aberrations

Optical aberrations show up as characteristic patterns in the focal plane that depend on the physical cause for the aberration itself. For example, chromatic aberration shows up as a different focal point for each frequency of light due to the dispersive nature of glass. Aberration theory describes the aberrations in terms of errors in the wavefront (difference between the actual wavefront and the paraxial wavefront) that manifest themselves as positional errors in the focal plane. Even though a wave description is used to describe and define the aberrations, a geometrical ray model is sufficient to trace an aberrated optical system. It is convenient to describe the wavefront error in rotationally invariant coordinates, H^2, ρ^2, and $H\rho\cos(\vartheta)$. The coordinate H is equal to the normalized radius of the image point($H^2 = x_i^2 + y_i^2$), ρ is equal to the normalized radius of the object point in the exit pupil ($\rho^2 = x_p^2 + y_p^2$), and ϑ is equal to the polar angle of the object point position in the exit pupil. Aberration theory defines several fundamental optical aberrations that typically contribute the most in optical systems, these are summarized in table 2.1 [4, 8, 27].

The terms $W_{H,\rho,\cos\vartheta}$ are constant coefficients called the aberration coefficients and the subscripts describe which independent variable terms are used by expressing the power to which they are raised. For example, coma, given as W_{131} would have a wavefront error expressed as $W_{131}H\rho^3\cos(\vartheta)$. The value of the aberration coefficient describes how strong the aberration is in the optical system and depends on the physical parameters of the optical system (focal length, diameter, incident angle, etc.). The positional ray error, or ray aberration, in the focal plane of a lens is given as the partial derivative of the wavefront error with respect to a coordinate axis in the image plane, e.g. x_i or y_i, multiplied by the negative ratio of the radius of curvature of the paraxial wavefront, R_p, to the radius of the exit pupil, $D_{XP}/2$. For example, the ray positional error for coma aberration would be given by,

$$\varepsilon_{x_i}(H,\rho,\cos(\vartheta)) = \frac{-2R_p}{D_{XP}}\frac{\partial}{\partial x_i}\left(W_{131}H\rho^3\cos(\vartheta)\right) = \frac{-2R_p}{D_{XP}}W_{131}H\rho^2\sin(2\vartheta), \tag{2.17}$$

and

$$\varepsilon_{y_i}(H,\rho,\cos(\vartheta)) = \frac{-2R_p}{D_{XP}}\frac{\partial}{\partial y_i}\left(W_{131}H\rho^3\cos(\vartheta)\right) = \frac{-2R_p}{D_{XP}}W_{131}H\rho^2(2+\cos(2\vartheta)). \tag{2.18}$$

It can be observed that the positional error depends on the square of the distance in the exit pupil and linearly on the distance in the image plane, therefore this aberration is classified as a 3$^{\text{rd}}$ order aberration. If a lens is traced with a numerous amount of rays, N, then a spot diagram will be produced as the image of all the rays. Spot diagrams are very useful for determining what effects the various aberrations of an optical system have on an image. From the spot diagram an average spot position ($\bar{\varepsilon}_H$,$\bar{\varepsilon}_{\vartheta_i}$) and root-mean-square (RMS) spot size may be defined using radial coordinates of the image,

$$\bar{\varepsilon}_H = \frac{1}{N}\sum_{j=1}^{N}\varepsilon_{H_j}, \tag{2.19}$$

$$\bar{\varepsilon}_{\vartheta_i} = \frac{1}{N}\sum_{j=1}^{N}\varepsilon_{\vartheta_{i_j}}, \tag{2.20}$$

and

$$\text{RMS} = \sqrt{\frac{1}{\pi}\int_0^{2\pi}\int_0^1(\varepsilon_H-\bar{\varepsilon}_H)^2\rho d\rho d\vartheta}. \tag{2.21}$$

Description of the Optical Aberrations

Defocus is caused either by choosing the wrong location for the focal plane, or by axially moving the lens by a distance δz. It can be seen that the defocus error depends linearly on the radius of the exit pupil, so that by stopping down the lens, and hence decreasing the radius of the exit pupil, the positional error due to a defocus will decrease. This is the fundamental reason why stopping down a lens will give better depth of focus.

Tilt is caused by an angular tilt offset either in the lens or the focal plane, or more generally because the focal plane and the lens plane are not parallel. The positional error for tilt depends linearly on the lens focal length and the error tilt angle. There is no way

to reduce this positional error other than by fixing the system so no tilt is in place, or by reducing the focal length of the system.

The effect of spherical aberration is that rays further out towards the edge of the exit pupil come to a focus closer to the exit pupil, i.e. before the paraxial focus, for a positive focal length lens, and opposite for a negative focal length lens. Hence it can be seen that by stopping down the lens the spherical aberration effect is reduced, as is the case in defocus. Having a parabolic curved surface can also eliminate this aberration.

Distortion is seen as an image magnification that depends on the position in the focal plane, hence the H^3 dependence on the position error. Distortion is caused by the location of the system stop relative to the position of the lens. If the stop is placed before a positive lens, and hence is the entrance pupil, the sign of W_{311} is negative and the ray error moves towards the optical axis; this is known as barrel distortion. If the stop is placed after a positive lens, and hence is also the exit pupil, the sign of W_{311} is positive and the ray error moves away from the optical axis; this is known as pincushion distortion. If the stop is coincident with the lens, and hence the lens itself is the system stop, then $W_{311} = 0$ and there is no distortion aberration.

Field curvature is due to the focal plane being planar and not curved. In the paraxial case off-axis object points in a plane are imaged onto a plane. In reality an off-axis object point in a plane will come to a focus at a point either before or after the paraxial focal plane depending if the power of the lens system is positive or negative. The deviation of the position of this focal point increases as the image point is further away from the optical axis. The surface that all points come to a focus on is called the Petzval surface.

Astigmatism is similar to field curvature in that the effect is seen to be that an off-axis object point will come to a different focal point than an on-axis object point. In fact, the y-axis positional error, ϵ_y, for astigmatism has the same functional form as field curvature, however the wavefront error is different and the x-axis positional error, ϵ_x, does not exist, or is zero. This implies that astigmatism is basically an additional effect similar to field curvature, however it only results in a positional error in one axis. Astigmatism is not due to the focal plane being planar and hence can be present even if field curvature is absent.

Coma is caused by an image magnification that is dependent upon the exit pupil location. Depending on the sign of the aberration coefficient, W_{131}, this magnification is either positive or negative. An object point can generally trace out a circle in the pupil with expanding radii until the pupil is completely filled. A spot diagram analysis indicates, and can be seen in the functional form of coma, that the image will also be a circle and displaced from the paraxial focal point in a direction depending on the sign of W_{131}. A summation of these circles, and hence the full spot diagram, will look like a snow-cone with the cone subtending 60°.

2.1.5 Radiometry

Radiometry is the science of measurement of electromagnetic radiation and it can be used to generally describe the light propagation throughout an optical system. Radiometry is highly geometric in nature and quantifies electromagnetic radiation in terms of joules, Watts, area, and solid angles. The solid angle, typically denoted by Ω, is a two dimensional angle in 3D space with dimensionless units of steradians. A steradian is the solid angle subtended by the surface area that is equal to the radius of a sphere squared. Since a sphere has a surface area of πD_{sp}^2 there are 4π steradians in a sphere. The solid angle for an object that is a section of a sphere as measured at the centre of the radius of curvature (centre of the sphere) can be calculated as,

$$\Omega = \int_{\phi_{\Omega_{min}}}^{\phi_{\Omega_{max}}} \int_{\theta_{\Omega_{min}}}^{\theta_{\Omega_{max}}} \sin(\theta_\Omega) d\theta_\Omega d\phi_\Omega, \tag{2.22}$$

where θ_Ω is the polar or zenith angle and ϕ_Ω is the azimuthal or rotational angle [4, 8]. This equation is not always useful because not all objects have a spherical curvature to them, although for spherical wavefronts and spherical lenses eqn. 2.22 is very relevant. Often eqn. 2.22 may be difficult to compute for complicated geometries and so an approximation for solid angle may be used given the area of a 2D object, A_{2D}, and the distance to the observation point, d_o,

$$\Omega \simeq \frac{A_{2D}}{d_o^2}. \tag{2.23}$$

The error of this approximation compared to the 3D spherical object with area, A_{3D}, is similar to the small angle approximation error shown in fig. 2.1 and so this approximation should only be performed when the observation distance is much larger than the height of the object area ($d_o \gg \sqrt{A_{3D}}$). A plot of the error as a function of zenith angle, θ_Ω, is shown in fig. 2.2.

In an optical system that is emitting radiation from a finite source area, A_s, located at some distance, d_{EP}, from an entrance pupil with area, A_{EP}, the total amount of geometrical light collected by the optical system may be calculated as,

$$\Xi = \int_{\phi_\Omega} \int_{\theta_\Omega} \int_{A_{EP}} \sin(\theta_\Omega) dA_{EP} d\theta_\Omega d\phi_\Omega, \tag{2.24}$$

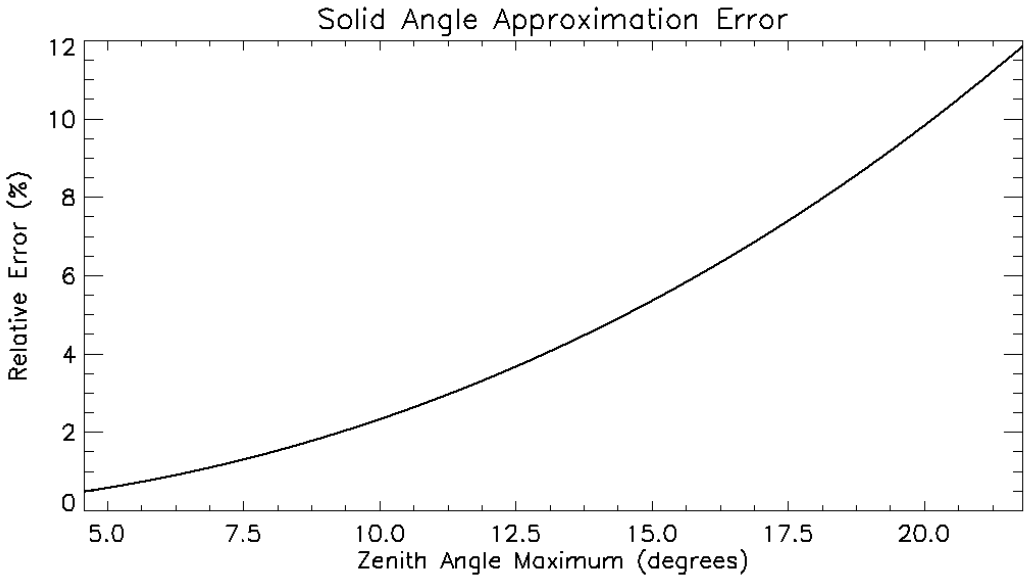

Figure 2.2: The relative error between the actual solid angle and the paraxial approximation plotted as a function of the zenith angle, θ_Ω. As the object distance d_o increases the zenith angle decreases and the error in the approximation decreases.

where the limits on the integration are taken over the source area angular description and the area of the entrance pupil. This is simply calculating the solid angle of the source as observed from every point within the area of the entrance pupil and taking the integrated value. This resulting value is known as the étendue and describes the light collection efficiency of an optical system. In the small angle approximation the solid angle can simply be expressed according to eqn. 2.23 and the étendue becomes,

$$\Xi = A_{EP}\Omega_s \simeq \frac{A_{EP}A_s}{d_{EP}^2} = A_s\Omega_{EP}, \tag{2.25}$$

where is can be seen that the étendue can be represented as the area of the EP multiplied by the solid angle of the source, Ω_s, or the area of the source multiplied by the solid angle of the EP. The most useful aspect of the étendue is that it is a constant in an optical system, and is therefore analogous to the Lagrange invariant defined in eqn. 2.13. The étendue is the solid angle equivalent to the Lagrange invariant when the chief and marginal ray solid angles are used; the two are related by [29],

$$O_L^2(\omega) = \frac{n^2(\omega)}{\pi^2}\Xi. \tag{2.26}$$

2.2 Wave Optics

Physical optics, or wave optics, is the treatment of light as an electromagnetic wave, rather than a ray. The wave optics model is necessary to describe optical phenomena such as interference and diffraction.

2.2.1 The Wave Equation and the Plane Wave Solution

Electric and magnetic fields in a medium with no charge or current may be described by the complex vectorial representation of Maxwell's equations given as:

$$\vec{\nabla} \cdot \vec{D} = 0, \tag{2.27}$$
$$\vec{\nabla} \cdot \vec{B} = 0, \tag{2.28}$$
$$\vec{\nabla} \times \vec{E} = -i\omega\vec{B}, \tag{2.29}$$
$$\vec{\nabla} \times \vec{H} = i\omega\vec{D}, \tag{2.30}$$

where $\vec{\nabla}\cdot$, $\vec{\nabla}\times$, and $\vec{\nabla}$ denote the divergence, curl, and gradient operator respectively, and $i = \sqrt{-1}$ [8, 34]. The complex electric and magnetic fields are given as $\vec{E}$ and $\vec{H}$ respectively and have units of volts per metre, and amperes per metre. The complex fields $\vec{D} = \epsilon\vec{E}$ and $\vec{B} = \mu\vec{H}$ are the electric and magnetic displacement fields and depend on the material parameters where ϵ is the dielectric material parameter, and μ is the magnetic material parameter. From now on only the electric field component will be discussed because optical instruments typically only measure the electric field and the mathematical treatment of the electric and magnetic field are essentially equivalent. The complex representation of a harmonic electric field is given as,

$$\vec{E}(\vec{r}, t) = \vec{E}(\vec{r}) \exp(i\omega t), \tag{2.31}$$

where t is time, ω is the angular optical frequency, and $\vec{r}$ is the positional vector. In a dispersive medium the dielectric and magnetic material parameters will depend on the optical angular frequency, i.e. $\epsilon(\omega)$ and $\mu(\omega)$. If the curl of eqn. 2.29 is taken with substitution of eqn. 2.30, the resulting relation is

$$\vec{\nabla} \times \vec{\nabla} \times \vec{E} = (\epsilon(\omega)\mu(\omega))\,\omega^2\vec{E}. \tag{2.32}$$

If a mathematical identity of $\nabla^2\vec{V} = \vec{\nabla}(\vec{\nabla}\cdot\vec{V}) - \vec{\nabla}\times\vec{\nabla}\times\vec{V}$ ([34]) is used with substituting in eqn. 2.27 then the result becomes,

$$\nabla^2\vec{E} - k^2(\omega)\vec{E} = 0, \tag{2.33}$$

where we make use of the definition of the material wavenumber, k, given in eqn. 2.2 and the definition of relative material variables, $\epsilon_r = \epsilon/\epsilon_0$ and $\mu_r = \mu/\mu_0$, where ϵ_0 and μ_0 are the permittivity and permeability constants of free space (vacuum). This result is known as the wave equation and all electromagnetic fields in a source free medium must obey eqn. 2.33. A plane wave is a solution to eqn. 2.33 and is described mathematically as

$$\vec{E}(\vec{r},t) = \vec{E}_0 \exp\Big(i(\omega t \pm \vec{k}\cdot\vec{r})\Big), \tag{2.34}$$

where $\vec{E}_0$ is the complex amplitude of the electric field and $\vec{k}$ is the vectorial material wavenumber. The vectorial nature of the material wave number is evident upon solving eqn. 2.33 for each scalar coordinate of the field. Plane waves are often the most useful and common types of electromagnetic waves encountered in optics. Plane waves describe collimated light and the normal to the plane defies the light ray used in geometrical optics.

2.2.2 Interference of Light

Interference is the result of two or more electromagnetic waves interacting with each other and may result in a measurable effect of which the type of interaction may be deduced. Often optical systems are designed with interference in mind in order to perform measurements not achievable through direct imaging. For example, the position of an object relative to a known distance may be determined with precision several orders of magnitude below the wavelength of the electromagnetic field. In this section we will assume the electromagnetic wave is planar and monochromatic, i.e. of a single frequency or wavelength. A more general treatment on interference with quasi-monochromatic or polychromatic radiation will be seen in section 2.2.4 where the concept of coherence is introduced. Using general complex notation the interference of two plane waves may be represented as,

$$\vec{E}_i(\vec{r},t) = \vec{E}_{0_1} \exp\Big(i(\omega t - \vec{k}_1\cdot\vec{r})\Big) + \vec{E}_{0_2} \exp\Big(i(\omega t - \vec{k}_2\cdot\vec{r})\Big), \tag{2.35}$$

where $\vec{E}_i$ is the interfered electric field comprising of the two electric fields denoted by subscripts 1 and 2. Optical detectors measure the square of the real part of the electric

field, $\vec{\mathcal{E}}^2$, but since the optical frequency is much larger than the temporal response of the detector, the time average of the squared real electric field is measured and defined to be the optical intensity given as,

$$I = \langle \vec{\mathcal{E}}^2 \rangle_t, \tag{2.36}$$

where $\langle \cdot \rangle_t$ denotes the time average (see list of symbols and definitions). The real component may be represented using complex notation as $2\vec{\mathcal{E}} = \vec{E} + \vec{E}^*$, where $*$ denotes the complex conjugate. Using this relationship the measured optical intensity of the two interacting plane waves may be expressed as,

$$I_i = \frac{1}{2}(|\vec{E}_1|^2 + |\vec{E}_2|^2) + \frac{1}{2}(\vec{E}_1 \cdot \vec{E}_2^* + \vec{E}_1^* \cdot \vec{E}_2). \tag{2.37}$$

It is noticed that the first term in eqn. 2.37 is simply the sum of the optical intensities from the two plane waves. The second term in eqn. 2.37 is the interference term between the two plane waves and it can be seen to explicitly depend on the vectorial product between the two fields. The vectorial nature of the electric fields is a statement of the polarization of the light. The amount of observed interference depends on the degree of polarization between the two interacting electric fields [8].

In eqn. 2.35 it was assumed the two plane waves had travelled for a time t before interacting and being measured, however, this assumption is not always correct. It is possible for two plane waves to have travelled different times before reaching a location, $\vec{r}$. We will denote the time of flight for the first wave as t_1 and the time of flight for the second wave as t_2. The time difference is given as $\tau = t_1 - t_2$. This time difference will manifest itself as an additional phase in one of the plane waves as $\Delta\phi = \omega\tau$, that can also be expressed as a distance phase $\Delta\phi = k\Delta d$, where Δd is the optical path length difference between the two waves. This last point is valid because light has the highest probability of taking the shortest optical path [8, 24, 41]. Adding this additional phase to one of the waves in eqn. 2.35, and assuming maximal polarization, the general interference wave can be expressed as,

$$I_i = I_1 + I_2 + 2\sqrt{I_1 I_2}\cos(\Delta\phi). \tag{2.38}$$

The interference intensity varies sinusoidally as a function of the phase, $\Delta\phi$, which depends on the time of flight difference, and equivalently the optical path difference between the two waves. When the interferometric term is greater than 0 it is referred to as constructive interference and when it is less than 0 it is referred to as destructive interference.

The sinusoidal oscillations of intensity are traditionally called fringes. The visibility of the fringes, V, may be defined in order to quantify the degree of interference, it is defined as

$$V = \frac{I_{max} - I_{min}}{I_{max} + I_{min}}. \tag{2.39}$$

2.2.3 Diffraction of Light

Diffraction is entirely due to the wave nature of the electromagnetic field itself and is typically observed when a field interacts with an object and does not require interaction with another wave, as is the case in interference. Diffraction ultimately limits the resolution of any optical system and is able to describe the response function of an optical system based on known measurable parameters (diameter of lenses, focal lengths, etc.). The most general treatment of diffraction begins with the complex vector formalism of Maxwell's equations and analyzes the electromagnetic field in various geometries. Without simplification and approximation very few diffraction problems may be solved completely [8], and therefore the most general treatment is often not practical. In order to understand the results of basic diffraction in common practise it is sufficient to describe the subject using scalar theory with valid approximations. Such will be the treatment of diffraction in this section.

Diffraction Gratings

A very important type of optical element, called a diffraction grating, is similar in effect to a prism in that the direction of the transmitted (or reflected) field depends on the optical frequency, ω. The diffraction grating operates under the principles of diffraction while a prism operates under the principles of refraction and dispersion. In the most basic sense a diffraction grating obeys the grating equation given as

$$\frac{m\lambda}{d_g} = \sin(\theta_i) + \sin(\theta_t), \tag{2.40}$$

where m indicates the order number and is an integer, d_g is the line spacing of the grating usually quoted in inverse lines per millimetre, and the two angles θ_i and θ_t are the incident and transmitted angles [8, 47]. The order number, m, refers to the number of wavelength differences in the constructive interference pattern.

Diffraction gratings are either reflective or transmissive and each have advantages and disadvantages [3, 7]. Gratings are characterized in terms of their line spacing, d_g, and

their blaze wavelength or angle. The blaze wavelength, λ_B, is the wavelength at which the grating has maximum efficiency, while the blaze angle, θ_B, is the angle of incidence at which the grating has maximum efficiency. A diffraction grating typically has highest efficiency when the incident angle and reflected/transmitted angle are equal, such a configuration is called the Littrow configuration [47]. Ideally the blaze angle and the Littrow angle are made to be equal and given by

$$\theta_B = \theta_L = \arcsin\left(\frac{m\lambda_B}{2d_g}\right). \tag{2.41}$$

Transmissive gratings operate slightly differently than reflective gratings. A transmissive grating is holographic in nature, and is typically formed by illuminating a photoresistive material by two monochromatic plane waves separated by an angle 2Θ. This will result in an interference pattern across the material where the period of the constructive interference is given as C [28]. If the photoresistive material is tilted at an angle Φ during exposure then the grating period at normal incidence appears to be $C_p = C/\cos(\Phi)$ and the grating equation becomes

$$m\lambda = C_p(\sin(\theta_i) + \sin(\theta_t)). \tag{2.42}$$

In an analogous manner, the maximum efficiency for a transmissive grating occurs in the Littrow configuration, which can be stated generally as $\theta_i - \Phi = \theta_t + \Phi$. This physically means the incident electromagnetic field is reflecting off of the plane of fringes, which occur at angle Φ. In this case the blaze condition for a transmissive grating may be stated as

$$m\lambda_B = 2C\sin(\theta_i - \Phi), \tag{2.43}$$

where the angle inside the sin argument is known as the blaze angle for a transmissive grating. Some vendors claim Φ as the blaze angle, so some caution must be taken when examining grating specification. In the latter case the blaze condition may be approximated by

$$\lambda_B = (n-1)d_g\sin(\Phi), \tag{2.44}$$

where n is the index of refraction of the grating material.

Diffraction Limit

It can be shown that the complex electric field at the focal point of a lens is the Fourier transform of the field before the lens multiplied by the aperture function of the lens [28],

$$E(x_i, y_i, k) = \frac{\exp\left(i\frac{k}{2f_L}(x_i^2 + y_i^2)\right)}{i\lambda f_L} \iint_{-\infty}^{\infty} E_0(x_p, y_p)\Pi(x_p, y_p) \exp\left(-i\frac{2\pi}{\lambda f_L}(x_p x_i + y_p y_i)\right) dx_p dy_p, \tag{2.45}$$

where f_L is the focal length of the lens, k is the wavenumber, x_i and y_i are the coordinates in the focal plane of the lens, x_p and y_p are the coordinates in the exit pupil of the lens, and $\Pi(x_p, y_p)$ is the aperture function of the lens. Equation 2.45 leads to the celebrated diffraction limit of a lens or imaging system. If a plane wave of unit amplitude is incident on a lens with a circular aperture with a diameter, D_a, and image coordinate $H = \sqrt{x_i^2 + y_i^2}$, the complex field distribution is seen to be,

$$E(H, k) = \exp\left(i\frac{kH^2}{2f_L}\right)\frac{\pi D_a^2}{4i\lambda f_L}\left(\frac{2J_1\left(kD_aH/2f_L\right)}{kD_aH/2f_L}\right), \tag{2.46}$$

where J_1 is a Bessel function of the first kind, first order. The measured signal is the optical intensity ($|E(H)|^2$) which is shown to be,

$$I(H, k) = \left(\frac{\pi D_a^2}{4\lambda f_L}\right)^2\left(\frac{2J_1\left(kD_aH/2f_L\right)}{kD_aH/2f_L}\right)^2. \tag{2.47}$$

This celebrated intensity distribution is known as the Airy pattern, a plot of the cross section of the pattern can be seen in fig. 2.3. The width of the central lobe is defined as when the function first reaches zero, the width, w, of this lobe is given as

$$w = \frac{1.22\lambda}{\mathrm{NA}}. \tag{2.48}$$

It can be shown that in general any infinitesimal point in the image is convolved by the Airy pattern [28], and therefore it is typically claimed that the spot size in an image is limited by diameter of the central lobe in the Airy pattern given by eqn. 2.48. This claim is known as the diffraction limit. The Rayleigh spatial resolution condition states that two diffraction limited spots may be resolved if the peak of one Airy pattern lies on top on the first zero point of the other Airy pattern.

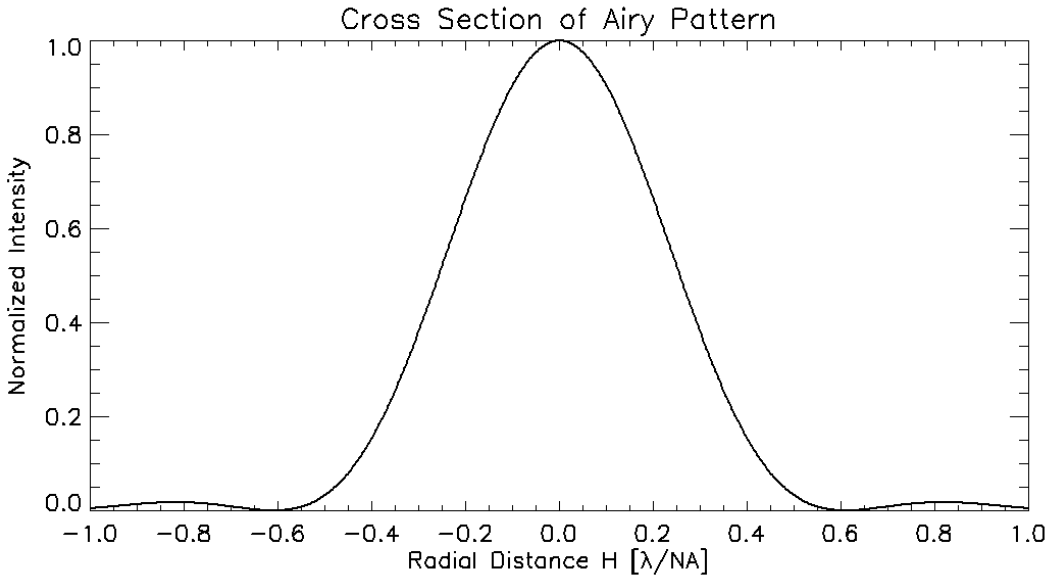

Figure 2.3: A cross section of the 2D Airy pattern for a uniformly illuminated circular pupil. The functional form is given in eqn. 2.47 and the domain is plotted in units of $\lambda/\,\mathrm{NA}$.

2.2.4 Optical Coherence

The development of interference in section 2.2.2 was overly simplistic in that it assumed completely monochromatic light that was perfectly spatially coherent. Coherence in the context of optics means the electromagnetic radiation is of the same origin. In optics there are two basic kinds of coherence, temporal coherence means that the radiation has emitted at the same time, and spatial coherence means the radiation has emitted from the same location. In order for interference to occur with good visibility the wave must be both spatially and temporally coherent [41, 61].

Temporal Coherence

Given two complex electric fields originating from different locations, $\vec{r}_1$ and $\vec{r}_2$, and interacting at a location, $\vec{r}$, by travelling for times, t_1 and t_2, via path lengths, d_1 and d_2, the interaction may be given by

$$E(\vec{r},t) = E_1(\vec{r}_1, t - t_1) + E_2(\vec{r}_2, t - t_2). \tag{2.49}$$

The time average optical intensity is given as

$$I(\vec{r}) = I(\vec{r}_1) + I(\vec{r}_2) + 2\Re\left[\Gamma(\vec{r}_1, \vec{r}_2, \tau)\right], \tag{2.50}$$

where $\Re[\cdot]$ denotes the real part. The function $\Gamma(\vec{r}_1, \vec{r}_2, \tau)$ where $\tau = t_1 - t_2$ is known as the mutual coherence function and is given formally as the time average cross-correlation between the two electric fields [41, 61],

$$\Gamma(\vec{r}_1, \vec{r}_2, \tau) = \langle E_1^*(\vec{r}_1, t) E_2(\vec{r}_2, t + \tau) \rangle_t. \tag{2.51}$$

In general the mutual coherence function is complex. It may be normalized to form the complex degree of coherence, γ given by,

$$\gamma(\vec{r}_1, \vec{r}_2, \tau) = \frac{\Gamma(\vec{r}_1, \vec{r}_2, \tau)}{\sqrt{I(\vec{r}_1) I(\vec{r}_2)}}, \tag{2.52}$$

which is also complex and may be represented as a magnitude and phase,

$$\gamma(\vec{r}_1, \vec{r}_2, \tau) = |\gamma(\vec{r}_1, \vec{r}_2, \tau)| \exp\left(i\bar{\omega}\tau\right), \tag{2.53}$$

where $\bar{\omega}$ is given as the mean optical angular frequency of light for the source bandwidth. An additional phase term has been neglected from eqn. 2.53 since it is only leads to higher order effects and are beyond the scope of this thesis. For a complete treatment of coherence theory refer to [41]. From eqns. 2.53 and 2.50, the interaction at location $\vec{r}$ may expressed as

$$I(\vec{r}) = I(\vec{r}_1) + I(\vec{r}_2) + 2\sqrt{I(\vec{r}_1) I(\vec{r}_2)}\, |\gamma(\vec{r}_1, \vec{r}_2, \tau)| \cos\left(\bar{\omega}\tau\right). \tag{2.54}$$

It can be seen that the total optical intensity of the interaction of the two electric fields will vary sinusoidally with a dependence on the optical path difference $|d_1 - d_2| = \tau c$. The third term in eqn. 2.54 is known as the interference term. The fringes are defined as the sinusoidal deviations from the mean optical intensity level, given as the sum of the first two terms. The amplitude of the fringe deviations depends on the magnitude of the complex degree of coherence, which varies from 0 to 1. The fringe visibility is defined according to eqn. 2.39 but with eqn. 2.54 expressing the optical intensity.

Spectral Coherence

The complex electric field may be represented as a Fourier transform as follows [41, 61],

$$E(\vec{r},t) = \int_0^\infty \widetilde{E}(\vec{r},\omega)\exp\left(-i\omega t\right)d\omega, \tag{2.55}$$

where it is understood that $\widetilde{E}(\vec{r},\omega) = 0$ for $\omega < 0$. Since $E(\vec{r},t)$ is a complex representation of the real measurable field $\mathcal{E}(\vec{r},t)$, it follows that $\widetilde{E}(\vec{r},-\omega) = \widetilde{E}^*(\vec{r},\omega)$ and therefore negative frequencies carry no additional information than positive frequencies. From eqn. 2.55 a cross-spectral density function may be defined analogous to the mutual coherence function,

$$\Psi(\vec{r}_1,\vec{r}_2,\omega) = \langle\widetilde{E}^*(\vec{r}_1,\omega)\widetilde{E}(\vec{r}_2,\omega')\rangle_e, \tag{2.56}$$

where $\langle\cdot\rangle_e$ represents the ensemble average (see list of symbols and definitions), and ω' is any optical frequency different from ω. From the Wiener-Khintchine Theorem, the mutual coherence function is shown to be the Fourier transform of the cross-spectral density function [41, 61]. The Wiener-Khintchine Theorem is stated that that the cross-spectral density function is the Fourier transform of the cross-correlation function[1]. Since the cross-spectral density function, Ψ, is the cross-correlation of the inverse Fourier transform of an electric field, we may express Γ and Ψ as,

$$\Gamma(\vec{r}_1,\vec{r}_2,\tau) = \int_0^\infty \Psi(\vec{r}_1,\vec{r}_2,\omega)\exp\left(-i\omega\tau\right)d\omega, \tag{2.57}$$

and

$$\Psi(\vec{r}_1,\vec{r}_2,\omega) = \frac{1}{2\pi}\int_{-\infty}^\infty \Gamma(\vec{r}_1,\vec{r}_2,\tau)\exp\left(i\omega\tau\right)d\tau. \tag{2.58}$$

If the two points $\vec{r}_1$ and $\vec{r}_2$ are both the same the cross-spectral density function is reduced to the optical power spectrum of the source,

$$S(\vec{r},\omega) = \Psi(\vec{r},\omega), \tag{2.59}$$

[1]For a proof of the Wiener-Khintchine Theorem see appendix B

where $S(\vec{r},\omega)$ is the optical power spectrum measured at some point in space given by $\vec{r}$. In lieu of eqns. 2.58 and 2.59 it is shown that the optical power spectrum of light may be given as the inverse Fourier transform of the autocorrelation function (see appendix B). Similar to the complex degree of coherence, a normalized cross-spectral density function, called the spectral degree of coherence, ψ, may be defined as,

$$\psi(\vec{r}_1,\vec{r}_2,\omega) = \frac{\Psi(\vec{r}_1,\vec{r}_2,\omega)}{\sqrt{S(\vec{r}_1,\omega)S(\vec{r}_2,\omega)}}. \tag{2.60}$$

This may also be represented in magnitude and phase similar to eqn. 2.53,

$$\psi(\vec{r}_1,\vec{r}_2,\omega) = |\psi(\vec{r}_1,\vec{r}_2,\omega)| \exp(i\omega\tau). \tag{2.61}$$

Using eqn. 2.61 the spectral equivalent of eqn. 2.54 is found to be

$$S(\vec{r},\omega) = S(\vec{r}_1,\omega) + S(\vec{r}_2,\omega) + 2\sqrt{S(\vec{r}_1,\omega)S(\vec{r}_2,\omega)}\,|\psi(\vec{r}_1,\vec{r}_2,\omega)| \cos(\omega\tau). \tag{2.62}$$

This equation is known as the spectral interference law. It can be see that the spectral density, $S(\vec{r},\omega)$, at a position, $\vec{r}$, is given as the sum of the spectral densities from the two points $\vec{r}_1$ and $\vec{r}_2$ plus a general interference term, that depends sinusoidally on the optical path difference $|d_1 - d_2| = \tau c$, and whose amplitude depends on the degree of spectral coherence at some frequency ω. Because of the Wiener-Khintchine theorem, the spectral degree of coherence, ψ, is related in a Fourier-like manner[2] to the complex degree of coherence, γ.

2.3 Statistical Optics

Statistical optics is a subject that deals with the statistical nature of optical detection. Fundamentally on a quantum level optics is probabilistic in nature, however, this level of detail is outside the scope of this thesis. A semi-classical treatment may be provided in which the fields are described classically, but the detection may be treated discretely with a probabilistic nature.

[2]The two are not strictly Fourier transform pairs, however we will treat them as so. The higher order effects and rigorous mathematical treatment are beyond the scope of this thesis. Refer to [41] for a complete treatment.

Optical Properties of Tissue		
Name	**Symbol**	**Typical Value**
Absorption	μ_a	0.005 mm^{-1}
Scattering	μ_s	0.5 mm^{-1}
Anisotropy	g	0.8
Index of refraction	n	1.4

Table 2.2: Description of tissue parameters with common values in the visible region of the electromagnetic spectrum

2.3.1 Light Propagation In Tissue

Tissue is a very complex material from the point of view of modelling it in terms of the material parameters ϵ and μ, which are typically used to describe most materials encountered in optics. The interaction of electromagnetic radiation in a material where ϵ and μ are well defined is well understood, and analytic solutions may be found in most cases. Tissue in general cannot practically be modelled as a composition of regions with different material parameters because the problem becomes too complex and near impossible to solve. A simpler model for optical tissue interaction takes a more probabilistic and statistical approach and is able to produce results that agree well with experiment.

The common model of optical tissue interaction embraces the concept of photons and describes probabilistically the different events that a photon may take as it propagates and interacts with the tissue. Tissue may be modelled simply as homogeneous material with scattering and absorption coefficients (μ_s and μ_a), an index of refraction, n, and an anisotropy factor, g, that describes the scattering direction. Besides the index of refraction, the other coefficients may be thought of as a probability that a photon may be absorbed or scattered, and if it is scattered the anisotropy factor determines the scattering angle. A list giving typical values for these parameters for tissue in the visible-NIR region of the electromagnetic spectrum are given in table 2.2

The absorption and scattering coefficients are given in units of inverse distance because they are used in a Beer's law formulation to describe the attenuation of optical intensity after travelling some distance, d. Beer's law is stated as [57],

$$I = I_0 \exp\left(-\mu_t d\right). \tag{2.63}$$

Beer's law describes the number photons that have not had any event, either scattered or absorbed, as a function of distance. From the values in table 2.2 it is seen that after a distance of 2 mm the number of photons unaffected by scattering in the tissue has decreased

by a factor of e^{-1}. Similarly at a distance of 200 mm the number of photons unaffected by absorption has decreased by a factor of e^{-1}. It is seen that a photon has a much higher probability of being scattered than absorbed in tissue. Since a photon may be absorbed or scattered simultaneously a total attenuation coefficient must be used in eqn. 2.63 given as,

$$\mu_t = \mu_a + \mu_s. \tag{2.64}$$

In general the absorption and scattering coefficients are a function of wavelength. In typical tissue in the visible to near-infrared region of the electromagnetic spectrum the scattering coefficient decreases and the absorption coefficient increases with increasing wavelength, therefore longer wavelength light is able to pass through more tissue without being affected (scattered or absorbed).

When a photon is scattered the direction is random in both polar angle and azimuthal angle (θ_s and ϕ_s) but the polar angle depends on the anisotropy factor, g, such that there is a preferred direction of scattering. The azimuthal angle is assumed to be uniform over 2π. The scattering angles may be given by [57]

$$\cos(\theta_s) = \frac{1}{2g}\left(1 + g^2 - \left(\frac{1-g^2}{1-g+2gU}\right)^2\right), \tag{2.65}$$

and

$$\phi_s = 2\pi U, \tag{2.66}$$

where U is a uniform random variable with values from 0 to 1. Sometimes it is more useful to view the the probability density function for the polar angle, which is given as

$$Pr(\cos(\theta_s)) = \frac{1-g^2}{2(1+g^2-2g\cos(\theta_s))^{\frac{3}{2}}}. \tag{2.67}$$

Most optical tissue interaction models are fundamentally based on these equations. Common methods to model a tissue imaging system is to perform a Monte Carlo simulation based on the absorption and scattering coefficients [49]. Analytic models use a diffusion approximation derived from the radiative transfer equation [57]. The analytic models are more accurate than the Monte Carlo simulations, but typically are more complex.

2.3.2 Photon Statistics

Of great interest in optics is the statistics of radiation detection. For the sake of this discussion the concept of photons will be used, which are the particulate description of electromagnetic radiation. An optical detector is exposed to electromagnetic radiation for some amount of time. For each incident photon there is some probability that it will be converted to an electron, this probability is known as the quantum efficiency of the detector, η. Each electron adds an electron volt of charge across the detector. After a certain amount of time given as the exposure time the voltage is measured. The voltage divided by the integration time is proportional to the average optical power incident on the detector during the exposure time. Essentially the optical detection process is a photon counting procedure. The photon emission from a radiating source is uncorrelated, i.e. independent, and therefore the counting procedure can be modelled as a Poisson process. The probability distribution of photon arrival can be given as the Poisson distribution,

$$Pr(j) = \frac{P^j \exp(-P)}{j!}, \tag{2.68}$$

where j is the number of photons counted and P is the mean number of detected photons, also known as the Poisson rate [4]. The mean and variance are both equal to the Poisson rate, P. In the context of optics the mean optical power is given by P/t_e, where t_e is the exposure time. The signal-to-noise ratio (SNR) may be defined as the mean signal, $\bar{j}$ divided by the standard deviation, σ_j, of the signal. For optics obeying the Poisson probability distribution the SNR may be given as

$$\text{SNR} = \frac{\bar{j}}{\sigma_j} = \frac{P}{\sqrt{P}} = \sqrt{P}. \tag{2.69}$$

It is seen that the photon noise goes as the square root of the expected number of detected photons during an exposure time event. To understand the spectral, or frequency, characteristics of an optical signal consider a constant optical power is incident on a detector with a fixed exposure time, hence P is a constant. If the optical signal is plotted as a function of time, each time point will have a different value of j given by eqn. 2.68. Since photon arrival is uncorrelated the values for j will be uncorrelated as well even though their means are all the same. This means that if j is much larger than P for a particular time point nothing can be said about the value of j for an adjacent time point. If the Fourier transform of the optical signal with its mean subtracted is taken ($\text{FT}[j(t) - P]$) the resulting spectrum will have equal power over an infinite extent and therefore the photon noise is said to be white noise.

Chapter 3

Optical Coherence Tomography

Optical coherence tomography (OCT) is an imaging modality that operates on the principles of interferometry in order to measure the reflectivity of a sample as a function of depth. OCT is typically used as a medical imaging instrument because it is able to produce 3D volume images of tissue with several millimetres of penetration depth at sub-cellular resolution ($\lesssim$ 10 μm). OCT does not necessarily need to be in contact with the tissue it is imaging so this advantage allows OCT to be used as a non-invasive medical imaging system, which has a large impact in the field of ophthalmology. OCT is also a good candidate for a tissue sample microscope since high-resolution images can be obtained with very little preparation time and the 3D depth sectioning is already inherent to the OCT signal, while for confocal microscopes only single thin layers ($\sim$6 μm) may be imaged at a time and typically require long preparation times. An OCT system was constructed that was designed to operate as a tissue sample microscope and also serve as a research test-bed system for easily trying out various ideas for hardware implementation. One example of this is the implementation of the optical pupil slicer (OPS) into the OCT instrument to evaluate its performance improvement. This chapter is divided into two sections, the first goes over the history and basic theory of OCT, and goes into specific theory on a certain implementation of OCT called spectral domain optical coherence tomography (SD-OCT). The next section describes the custom built OCT system used in this research and provides some system characterization results and an example image. The operation of the spectrograph and the inclusion of the OPS is briefly mentioned but is left to a more lengthy discussion in chapter 4.

3.1 Theory and Background of Optical Coherence Tomography

Optical coherence tomography is a relatively new field, with the first OCT papers being published in the late 1980's and early 1990's [18]. The foundations of OCT are based on low coherence interferometry and diffuse microscopy; essentially a hybrid between interferometry and optical imaging of tissue. The core of most OCT systems is a Michelson interferometer, for which its inventor, Albert Michelson, won the Nobel Prize in Physics in 1907. Today the Michelson interferometer is considered fundamental, and the properties and applications are well understood.

A Michelson interferometer may be used as a spectrograph due to the Weiner-Khintchine Theorem (see appendix B). By translating the mirror in one of the interferometer arms an interferogram is produced, which is the autocorrelation function of the input light source, and its Fourier transform may be taken to produce the spectrum. This configuration of the Michelson interferometer is commonly known as a Fourier Transform Spectrograph (FTS). The interferogram has a maximum value when the optical path difference (OPD) between the two arms is zero and is an even function. If the input spectrum is broadband, i.e. has low temporal coherence, then the interferogram will be narrow and only have strong signal very close to the zero OPD location.

The very first OCT systems were essentially FTS systems with the stationary mirror being replaced by a focusing lens and a tissue sample. A tissue sample typically has multiple reflection locations, and therefore has multiple locations of zero OPD when the scanning mirror is translated. The fundamental OCT signal is a depth scan, called an a-scan, that shows the reflectivity profile as a function of depth. At each reflection location the interferogram is seen with an amplitude corresponding to the reflectivity at that location. A narrow interferogram, i.e. broadband light source, is required to distinguish between different reflection positions located close to one another.

A significant improvement to OCT technology was adopted in the late 1990's, when it was discovered that a-scans could be produced without having to scan a mirror in the interferometer [18, 22, 35]. Instead, the spectrum of the output of the interferometer could be recorded and the reflectivity profile could be obtained by taking the Fourier transform. This method of OCT is called Fourier Domain OCT (FD-OCT), as opposed to Time Domain OCT (TD-OCT), which requires scanning a mirror. It was quickly discovered that FD-OCT offers a significant sensitivity improvement over TD-OCT [13, 14, 39]; signal-to-noise ratio improvements on the order of 20 dB are seen in the latest literature [13, 38]. Not only does FD-OCT offer significant signal improvement over TD-OCT, it is also much faster since an entire a-scan is collected at once.

There are two basic methods of achieving FD-OCT: one is by recording the output of

the interferometer with a spectrograph and using a broadband light source, and the second is by recording the spectrum of the light source by using a single element detector and a frequency sweeping light source. The former method is called Spectral Domain OCT (SD-OCT) and the latter method is called Swept Source OCT (SS-OCT). Both SD and SS OCT produce similar results and the systems typically only differ in the types of components that cause the limiting factors. In this research an SD-OCT system was constructed so this implementation of FD-OCT will be considered for the remainder of this thesis.

3.1.1 The SD-OCT Signal

The goal of OCT is to produce a depth image of the reflectivity of a sample. In the biomedical field the sample is typically tissue and the reflectivity depth image is used to examine the tissue structure. In SD-OCT a broadband light source is used in the interferometer to probe the tissue and a dispersive spectrograph is used to record the light to produce the image. A more complete treatment of dispersive spectrographs and their properties will be given in chapter 4, but for now their properties and how they affect SD-OCT will be explained.

The light exiting the sample will be reflecting from many different depths and therefore have different optical path lengths (OPL) over which it has travelled. On the other hand, the light from the reference arm has a constant OPL. Subtracting the OPL of the reference arm from the OPLs from the sample arm will result in many different optical path differences (OPD). The goal of OCT in general is to distinguish and measure the reflection locations in the sample by measuring the OPDs. In SD-OCT this is achieved by recording the spectrum of the interfered light by using a dispersive spectrograph. To appreciate how the OPD information is manifested in the spectrum first consider the general interference equation for measuring light as a function of wavenumber for a fixed delay position,

$$I(k) = I_r(k) + I_s(k) + 2\sqrt{I_r(k)I_s(k)}\cos\left(k\Delta d\right), \tag{3.1}$$

where $\Delta d = |d_r - d_s|$ and d_r and d_s are twice the distances from the beam splitting device to the reflection locations in the reference and sample arms respectively (twice the distance because the light has to travel from the beam splitting device to the reflection location, and then back to the beam splitting device), k is the wavenumber of light being measured (see eqn. 2.2), and $I_r(k)$ and $I_s(k)$ are the optical power spectra of the reference arm and the sample arm respectively. It is seen that for a fixed optical delay (OPD $= |d_r - d_s|$) the intensity of the interference spectrum will vary sinusoidally as a function of wavenumber. Since the frequency of the sinusoidal oscillation depends on the OPD, signal processing to measure the frequency will also measure the OPD. The simplest way to measure the

sinusoidal frequency of a signal is to perform the Fourier transform. With optimal signal processing available by subtracting the effects of the reference and sample spectra from the interference spectrum, an a-scan, $A(d)$, can be produced,

$$A(d) = \frac{B}{2}\left(\delta(d - \Delta d) + \delta(d + \Delta d)\right), \tag{3.2}$$

where $\delta(d)$ is the Dirac delta function as a function of optical delay, d, and B is the average integrated spectral reflectivity at the reflection location. The theory presented in eqns. 3.1 and 3.2 represents the most ideal case and only serves as a proof of concept of the signal extraction. In reality there are many other factors that must be taken into account, but the general SD-OCT signal philosophy is embedded in the above theory. In SD-OCT the spectrum is recorded with a dispersive spectrograph with a limited number of pixels with finite width, therefore it is impossible to record the spectrum as a function of infinitesimal wavenumber. Instead, the spectrum is recorded as a function of wavelength, λ, with each spectral sample being separated by a wavelength range, $\Delta\lambda$. Since each pixel has finite width, it will have a full-width half maximum bandwidth, $\delta\lambda$, which serves as the spectral resolution of the spectrograph.

Because of the spectral measurement conditions the idealized interference equation may not be used to describe the recorded spectrum. A more general treatment using optical coherence theory must be constructed. From the description of optical coherence in section 2.2.4 we may construct a description of the optical intensity in a single pixel, j, due to a single reflection location,

$$\begin{aligned} I_j(d_s) &= \int_{\delta\lambda_j} \left(I_r(\lambda) + I_s(d_s, \lambda)\right) d\lambda \\ &+ \left|\psi_j\left(\Delta d, \delta\lambda_j\right)\right| \cos\left(2\pi\frac{\Delta d}{\lambda_j}\right) \cdot \int_{\delta\lambda_j} 2\sqrt{I_r(\lambda) I_s(d_s, \lambda)} d\lambda, \end{aligned} \tag{3.3}$$

where $\delta\lambda_j$ is the spectral bandpass with central wavelength λ_j for the j^{th} pixel, and ψ_j is the spectral coherence function for the j^{th} pixel, which depends on the OPD and the pixel bandpass. Comparing the advanced description of the interference intensity (eqn. 3.3) with the idealized description (eqn. 3.1) we see that the two are very similar with the greatest difference being the spectral coherence function term, ψ_j. It is the coherence function that is of critical importance to describing signal characteristics of the SD-OCT system. The interfered spectrum will be recorded with a given number of pixels, J, each with a different

central wavelength, λ_j, and bandpass function $\delta\lambda_j$. As a reasonable approximation[1], the wavelength separation between any two adjacent pixels is the same for all pixels in the spectrograph; this value is defined as $\Delta\lambda$. With complete knowledge of the sample arm and reference arm spectra, their modulation effect may be taken out of eqn. 3.3 by subtracting the spectra and dividing by the geometrical (square root) mean. The a-scan OCT signal is given as the discrete Fourier transform of the processed spectrum,

$$A(d) = \sum_{j=0}^{J-1} B\,|\psi_j\,(\Delta d, \delta\lambda_j)| \cos\left(2\pi\frac{\Delta d}{\lambda_j}\right) \exp\left(-2\pi i\frac{jd}{J}\right). \tag{3.4}$$

We see that the general form of the a-scan given in eqn. 3.4 is the Fourier transform of the sinusoidal function amplitude multiplied by the spectral coherence function amplitude in each pixel. From the convolution theorem this can be expressed as the Fourier transform of the sinusoidal function convolved with the Fourier transform of the spectral coherence function for a given OPD across the pixels [28]. The Fourier transform of the sinusoidal function is simply a pair of Dirac delta functions, as was seen in eqn. 3.2, located at $d = \pm|d_r - d_s|$. The Fourier transform of the spectral coherence function with respect to the pixel number is something that requires a little more thought.

We define the spectral coherence envelope as the envelope along the delay axis of the spectral coherence function—for a single pixel this is given as the Fourier transform of the spectral bandpass function in the pixel, or equivalently the envelope of the complex degree of coherence function, γ (see section 2.2.4). The independent variable in the Fourier transform $(1/\Delta\Lambda)$ may be converted to OPD by multiplying it by λ_j^2 (refer to appendix A for a proof). The attenuation of interference intensity as a function of OPD is described by this relationship. Given a delay position, the value of the spectral coherence envelope is unique for each pixel since the bandpass function for each pixel is different. Assuming a different coherence envelope for each pixel will tend to complicate the end result beyond the scope of this thesis and is only useful for examining higher order effects. It may be assumed that the entire SD-OCT system may be characterized by the average spectral coherence function, which assumes that each pixel behaves the same. Since each pixel will have the same attenuation value for a given delay, the Fourier transform of the spectral coherence function with respect to the pixel numbers will be a Dirac delta function convolved with a sinc function with a width inversely proportional to the spectral imaging window—and of course the amplitude is given as the attenuation value at the specific delay position

The spectral coherence envelope is given as the Fourier transform of the spectral bandpass function in a pixel, or equivalently the envelope of the complex degree of coherence function through the Wiener-Khintchine Theorem (see section 2.2.4). The pixel has a

[1]See chapter 4 for a description of why this approximation is valid.

spectral width given by $\Delta\lambda$ and an actual bandwidth $\delta\lambda$ centred about a mean system wavelength λ_0. Since the pixel spatial response function is typically a RECT function, and the bandpass is typically described by a Gaussian function, the spectral coherence envelope is generally accepted in the literature to be,

$$\psi(z) = \text{sinc}^2\left(\frac{2\pi\Delta\lambda}{\lambda_0^2}z\right)\exp\left(-\left(\frac{2\pi}{\lambda_0^2}z\right)^2\frac{\delta\lambda^2}{2\ln(2)}\right), \tag{3.5}$$

where z is given as the physical delay, equal to half the OPD. The signal that is pertinent to SD-OCT is the sinusoidal variation of the spectrum [16, 18, 63]. Since the sinusoid is being sampled with a limited number of pixels with a sample separation of $\Delta\lambda$, the maximum frequency that can be measured without signal aliasing will be limited by Nyquist. The maximum number of sinusoidal oscillations that can be be measured with J pixels is $J/2$. Since each pixel is separated by $\Delta\lambda$ and the conversion in the coherence envelope domain from wavenumber to physical delay is given by multiplying the independent variable by $\lambda_0^2/2$, the maximum unaliased imaging depth in SD-OCT may be given by,

$$z_{max} = \frac{1}{4n}\frac{\lambda_0^2}{\Delta\lambda}, \tag{3.6}$$

where n is the index of refraction of the sample; this relationship is proved in appendix A. This maximum unaliased imaging depth is implicitly embedded in the functional form for the spectral coherence envelope in eqn. 3.5. We see from the spectral coherence envelope that the depth imaging characteristics in SD-OCT may be almost completely described by the wavelength separation between pixels, $\Delta\lambda$, and the bandwidth per pixel, $\delta\lambda$. As will be seen in chapter 4, these two values are completely determined by the spectrograph hardware, and therefore the depth imaging performance in SD-OCT is determined by the quality of the spectrograph. The depth imaging resolution, however, is only dependent on the total measured bandwidth of the system light source, $\Delta\Lambda$. An illustrative example of the process of converting a recorded spectrum in an SD-OCT system to an a-scan is shown in fig. 3.1 and the SD-OCT system parameters are summarized in table 3.1.

The interference spectra in fig. 3.1(a) were generated by assuming the reflecting object was a perfect mirror, i.e. the sample and reference arm spectra were identical. The coherence envelope was defined according to eqn. 3.5 with $\Delta\lambda$ =0.0489 nm and $\delta\lambda$ =0.08 nm, and used in eqn. 3.3 to generate the interference spectra. It can be seen that as the physical delay is increased, the resulting frequency of the interference sinusoid also increases while the modulation amplitude decreases. By convention in interferometry each sinusoidal oscillation is called a fringe and the relative amplitude of the fringes compared with the mean signal is defined as the visibility (see eqn. 2.39). Using this terminology we say that

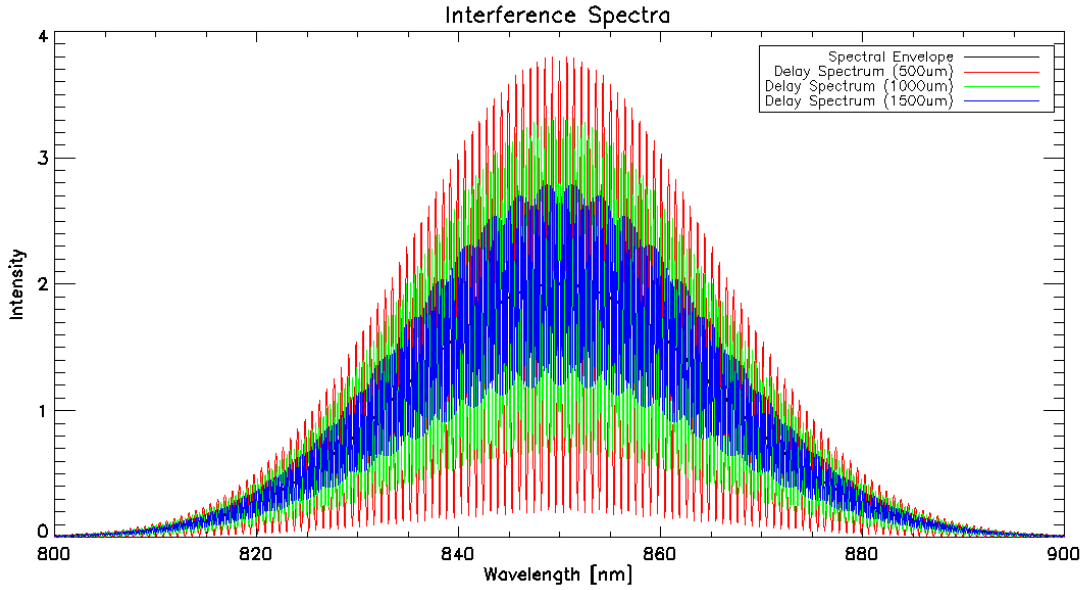

(a) Spectrum

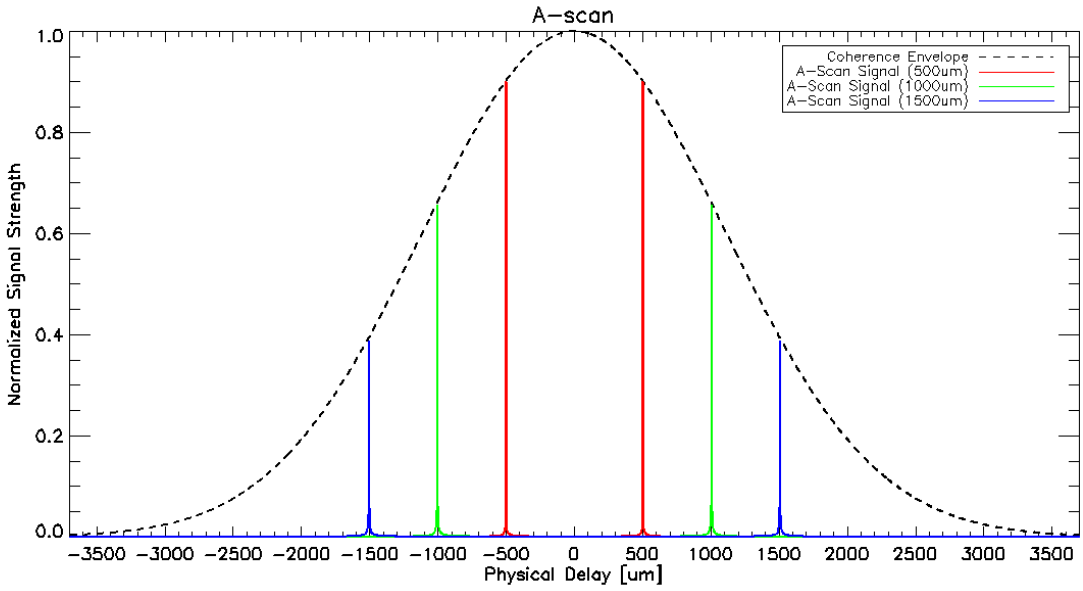

(b) A-Scan

Figure 3.1: The interference spectra for a delay positions of 500 μm, 1000 μm, and 1500 μm and the corresponding a-scan signal produced with optimal signal processing.

Simulation Input Parameters	
Parameter	**Value**
λ_0	850 nm
FWHM Source	35 nm
# Pixels	2048
Pixel Width	10 μm
$\Delta\lambda$	0.0489 nm
$\delta\lambda$	0.0800 nm

Table 3.1: The relevant parameters to determine the SD-OCT signal depth imaging signal for an example system.

the visibility of the fringes decreases with increasing delay, or imaging depth, according to the spectral coherence envelope. The converted a-scan in fig. 3.1(b) shows positional locations corresponding with the physical delay but shows that the reflection locations occur at $\pm$ the actual delay position, i.e. the a-scan is an even function. This is because the spectra collected are real with no phase information so the Fourier transform cannot discern between positive frequencies and negative frequencies. If we wish we can examine only one side of the a-scan, but we lose half our pixel resolution to do so. The peaks of the a-scan are equal to the total reflected power at that location modulated by the spectral coherence envelope. We can see with this SD-OCT system the fringe contrast at 1.5 mm of physical delay is only 0.4, or -3.98 dB, even though 100% of the light is being reflected.

The signal in SD-OCT may be defined as the total optical power, say the mean number of photons detected, P, multiplied by the visibility, V,

$$S_{\mathrm{OCT}} = PV, \tag{3.7}$$

where the visibility is given by eqn. 2.39 which is determined by the coherence envelope, ψ. This is a useful definition for signal because it scales the total amount of light collected at a reflection depth with the sensitivity corresponding to that depth. Using this definition it becomes clear that collecting 10^5 photons at a depth with a sensitivity of -10 dB is a better situation than collecting 10^6 photons with a sensitivity of -30 dB. In the latter case an order of magnitude more photons were collected but the OCT signal in the former case is 10 dB higher, therefore collecting more light does not necessarily mean better signal. The spectral coherence envelope in SD-OCT defines the sensitivity of the system as a function of depth.

Even though eqn. 3.6 defines the maximum theoretical unaliased imaging depth in SD-OCT, the practical and actual imaging depth is often less than this value [2, 18, 54]. Systems may be designed to have aliasing depths on the order of 7 mm even though

practical imaging depths are rarely larger than 3 mm. The reason for this is because the imaging depth in highly scattering media, such as tissue, is limited by the signal-to-noise ratio (SNR). According to light propagation in tissue (section 2.3.1), the amount of light that penetrates tissue without becoming absorbed or scattered decreases exponentially with an extinction coefficient proportional to the absorption and scattering coefficients. The type of light that SD-OCT is sensitive to is the light that is single back-reflected from a certain depth. Very often the ratio of optical power of single back-reflected light to multiply scattered light at a given depth will be much less than 1; when this ratio becomes too small then the noise contributing from the multiple scattered light (and reference arm light) will dominate the signal from the single back-reflected light (using the definition for SD-OCT signal above), and this defines the maximum imaging depth in SD-OCT as limited by SNR. A practical way to think of this in terms of the interference spectrum is that the light intensity variation has a larger variance than the visibility of the interference fringe.

A higher sensitivity SD-OCT instrument may increase the imaging depth because the point at which multiple scattered light dominates single back-reflected light will occur at larger imaging depths. This may physically be achieved by having a broader spectral coherence envelope, which can furthermore be achieved by having a higher quality spectrograph (see chapter 4). Not only will the imaging depth increase with a higher performing spectrograph, but the quality of the depth images will also increase by having a more sensitive SD-OCT instrument with a broader spectral coherence envelope and therefore producing images with higher SNR.

3.1.2 Other Limiting Parameters of SD-OCT

A powerful advantage of OCT over conventional imaging is that the axial and lateral resolution are independent of one another, albeit the central wavelength, λ_0. In other words, to increase one resolution, the other resolution does not need to change. The lateral resolution in OCT is defined by the classic Rayleigh criteria,

$$\Delta x = \frac{0.61\lambda_0}{\mathrm{NA}}, \tag{3.8}$$

where Δx is the closest two independent points may be separated and still be independently resolved. This value depends directly on the centre wavelength λ_0 and inversely on the numerical aperture, NA, of the focused beam. The focused spot size width is twice the Rayleigh value ($w = 2\Delta x$) and is also defined as the diffraction limit (see eqn. 2.48). The axial resolution in OCT is given famously as [18, 22]

$$\Delta z = \frac{2\ln 2}{n\pi}\frac{\lambda_0^2}{\Delta\Lambda}. \tag{3.9}$$

This value assumes the light spectrum is Gaussian about centre wavelength λ_0 with a full width half maximum bandpass of $\Delta\Lambda$. From eqns. (3.8) and (3.9) it can be seen that the two resolutions are independent of one another except for the choice of wavelength; a smaller wavelength results in better resolution keeping all other parameters equal.

Upon examining eqn. 3.8 it can be seen that in order to obtain the smallest lateral resolution the numerical aperture must be maximized. The trade off for large NA is a small depth of focus (DOF). The DOF is classically defined as the region in which the spot size is less than $\sqrt{2}$ times the minimum spot size, which is often called the Rayleigh range [8, 28]. Thus, a high NA beam will give good lateral resolution, but only over a small depth range. The depth of focus is defined as,

$$\mathrm{DOF} = \frac{(0.61)^2 n 2\pi\lambda_0}{\mathrm{NA}^2}, \tag{3.10}$$

and the spot width at any axial location, z, may be given as,

$$w(z) = 2\sqrt{\left(\frac{0.61\lambda_0}{\mathrm{NA}}\right)^2 + \left(\frac{\mathrm{NA}}{0.61n\pi}z\right)^2}. \tag{3.11}$$

In order to obtain the smallest axial resolution it can be seen from eqn. 3.9 that a broad spectrum is desired. However, since the axial point spread function (PSF) is given as the Fourier transform of the light spectrum, the shape of the spectrum is also important. It is desirable to have as close to a Gaussian spectrum as possible in order to obtain a good axial PSF without anomalous features such as side lobes which will induce imaging artifacts. A disadvantage of a very broad light source is the light will suffer from more dispersion, which may severely broaden out the axial PSF and degrade imaging performance. However, numerical dispersion correction techniques may be applied in SD-OCT in order to minimize these effects [23, 60]. The practical trade off for a broadband spatial coherent light source is cost; broad bandwidth light sources such as a Titanium-Sapphire laser are very expensive.

3.2 The Custom OCT System Designed and Used in this Research

A custom SD-OCT system was built with the purpose of serving as a tissue imaging microscope. The system is designed to be able to take large volumes of about 3 mm cubes and produce a 3D tomographic high-resolution image on time scales of several minutes. The OCT instrument also serves as a test-bed prototype system for experimenting with various hardware configurations and advancements, such as the optical pupil slicer.

The SD-OCT system consists of three primary subsystems: the interferometer, the spectrograph, and the sample imaging system which is called "the trapeze." The OCT system is designed to operate in the visible-NIR region (0.8 μm - 1.1 μm) of the electromagnetic spectrum as opposed to the NIR-IR region (1.1 μm - 2 μm) for several reasons. First because higher optical frequencies (shorter wavelengths) provide better lateral and axial resolution (see eqns. 3.8 and 3.9), and second because standard silicon detectors may be used which are cheaper, more available, and provide better spatial resolution than IR detectors, which are typically made of InGaAs. A disadvantage of vis-NIR light is that the scattering coefficient is larger than for light in the 1.3 μm to 1.5 μm region, however, the absorption coefficient is lower and penetration depths of up to several millimetres are still seen with vis-NIR light [49, 54, 57].

3.2.1 Optical Design of the SD-OCT System

An annotated cartoon drawing of the SD-OCT system can be seen in fig. 3.2 and the sample handling subsystem, "the trapeze," is seen in fig. 3.3. Everything to the right of the pinhole (PH) is the spectrograph part of the SD-OCT instrument, and everything to the left of the pinhole (PH) is the interferometer section of the instrument, including the sample handing system, "the trapeze." A list summarizing the hardware components used in the SD-OCT system can be seen in tables 3.2 and 3.3.

Interferometer

For the following section refer to fig. 3.2. The light source used in the SD-OCT system is a broadband super-luminescent diode (SLD) system with a centre wavelength of 845 nm, a FWHM of 100 nm, and total output power of 16 mW (Superlum, Broadlighter D-855-HP2). The SLD source for the SD-OCT system is coupled into a single mode fibre and fastened to the fibre launcher mount (FL) as the input to the system. The fibre launcher mount (New Focus, 8051) is kinematic and has translation control in the XY plane by two mini pico motors that have 30 nm precision and the mount allows for a $\pm$3 mm movement.

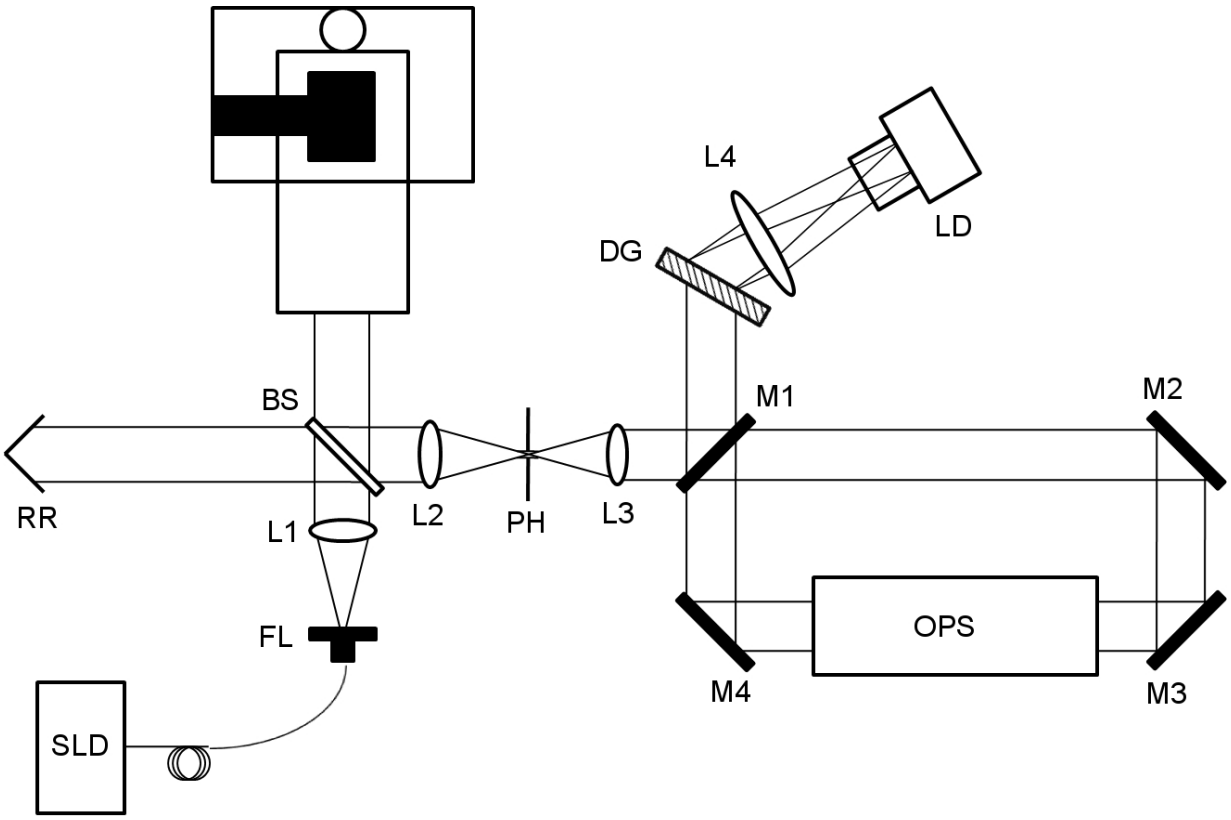

Figure 3.2: A cartoon layout of the SD-OCT system including the location of the optical pupil slicer.

SD-OCT System Hardware	
Parameter	**Value**
λ_0	845 nm
$\Delta\Lambda$	100 nm
L1 Focal Length	75 mm, f/3
L2 Focal Length	75 mm, f/3
L3 Focal Length	75 mm, f/3
L4 Focal Length	150 mm, f/3
DG power	1200 l/mm
Pixel Width	10 μm
Pixel Height	20 μm
# Pixels	2048

Table 3.2: The hardware parameters for the SD-OCT system components in the interferometer and spectrograph sections.

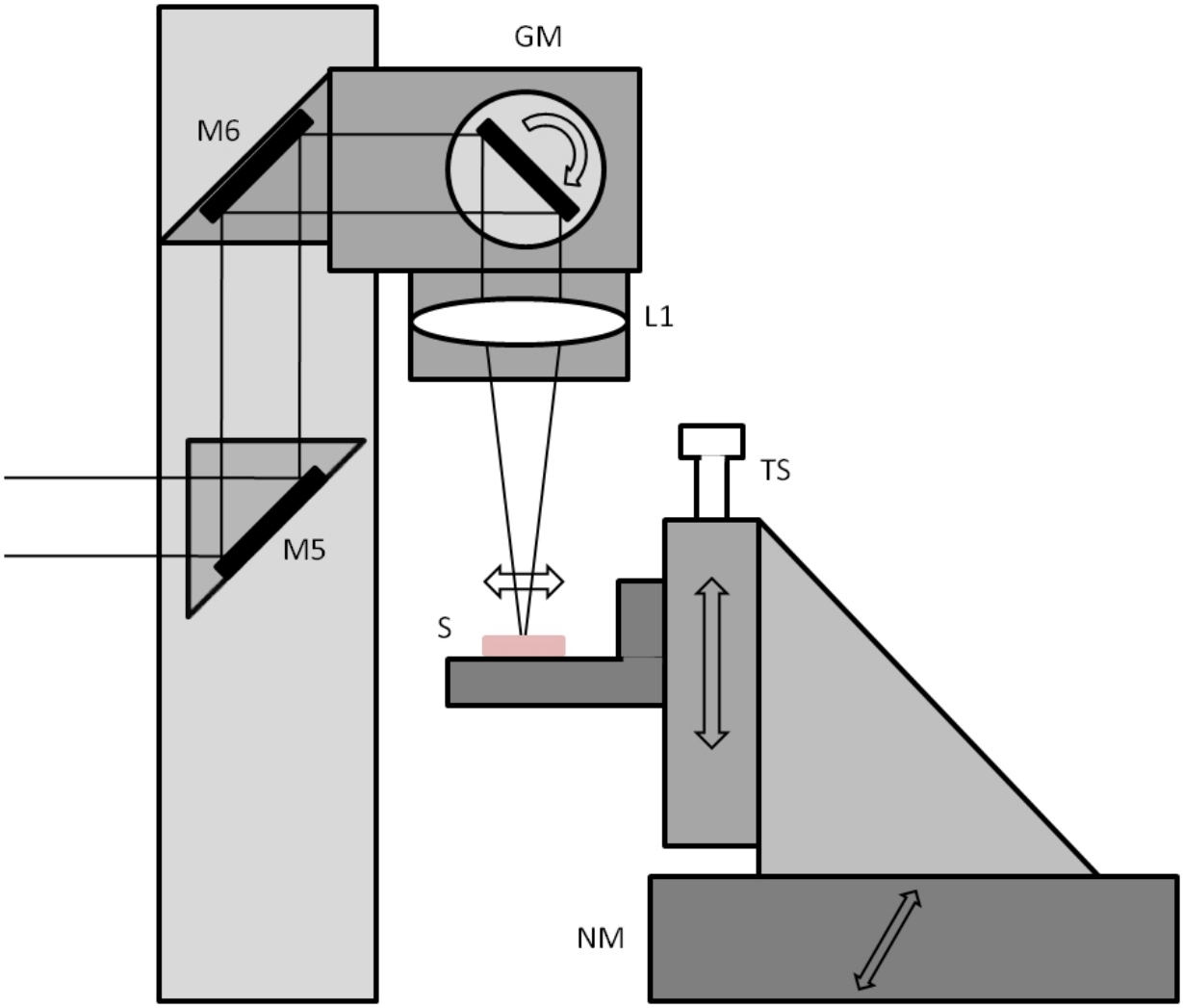

Figure 3.3: A cartoon layout of the sample scanning system, "the trapeze," in the SD-OCT system.

Trapeze System Hardware	
Parameter	**Value**
L1 Focal Length	100 mm, f/2
GM scan range	0.349 rad
GM scan precision	5.3 μrad
TS scan range	28 mm
TS scan precision	50.5 μm/rad
NM scan range	50 mm
NM scan precision	10 nm
NM scan accuracy	50 nm

Table 3.3: The hardware parameters for the sample handling subsystem in the SD-OCT instrument, "the trapeze."

The NA of the emerging beam is 0.14 and is collimated to be a 20 mm beam using a 1" diameter achromatic doublet (L1) with a focal length of 75 mm and design wavelengths of 706.5 nm, 855 nm, and 1015 nm (Thor Labs, AC254-075-B). The beam is split equally by a 2" diameter 50:50 non-polarizing beam splitting plate (BS) (Thor Labs, BSW17) where half the light is sent towards the reference arm of the interferometer and the other half of the light is sent towards the trapeze. The reference beam is directed towards a 1" hollow retro reflector (RR) (CVI Melles Griot, CCH-25.4-1-LEBG) that is mounted on two orthogonal translation stages (New Focus, 9067-COM) with two pico motors attached (New Focus, 8302) in order to provide up to $\pm$0.5" XY translation control with 30 nm precision. The translation control on the fibre launcher and retro reflector provide all the alignment control necessary in the interferometer [11]. The return beams from the reference and trapeze arms recombine at the beam splitting plate, BS, and are sent towards a spatial filter relay. The spatial filter consists of an identical focusing and re-collimating 1" diameter achromatic lens (L2 and L3) with a focal length of 75 mm and design wavelengths of 706.5 nm, 855 nm, and 1015 nm (Thor Labs, AC254-075-B), and a 10 μm pinhole (PH) (Newport, 910-PH10) at the focal point mounted in a kinematic lens position mount with translation control in XYZ (New Focus, 9841). The pinhole, PH, and collimating lens, L3, are the entry point to the spectrograph.

Trapeze

For the following section refer to fig. 3.3. The light entering the trapeze is directed towards a single galvanometer scanning mirror system (GM) (Nutfield, QuantumScan-30) by two 2" silvered mirrors (M5 and M6) (Thor Labs, PF20-03-P01). Upon reflecting off of the scan mirror, GM, the beam is directed downwards towards the sample (S); the scanning mirror

system is fastened in a custom mount. The light is brought to a focus by a 2" diameter achromatic doublet lens (L1) with a focal length of 100 mm and design wavelengths of 706.5 nm, 855 nm, and 1015 nm (Thor Labs, AC508-100-B) fixed in a custom mount. The sample is placed on a translation stage (TS) (New Focus, 9064-X) apparatus that is able to provide ±14 mm axial translation for depth positioning by a micrometer screw with 80 threads per inch. This translation stage is furthermore fastened to a high precision automated translation stage (NM) (Nanomotion, FB050) that is able to provide ±25 mm movement with 10 nm precision and 50 nm accuracy and repeatability. The Nanomotion stage movement direction is perpendicular to the scan mirror direction so that as the scan mirror sweeps back and forth in the X direction the translation stage is able to provide scanning in the Y direction; the OCT instrument provides the depth axial scanning. This way a full lateral 3D scan across the sample is obtained, thus producing a tomographic image. A publication describing the design, operation, and performance results in more detail can be found in [36].

Spectrograph

For the following section refer to fig. 3.2. The spectrograph in the SD-OCT system is a standard diffraction grating based dispersive spectrograph. The details on spectrograph operation are left to chapter 4. The entry point to the spectrograph is a 10 μm pinhole, PH (Newport, 910-PH10), collimated by a 1" diameter achromatic doublet lens (L3) with a focal length of 75 mm and design wavelengths of 706.5 nm, 855 nm, and 1015 nm (Thor Labs, AC254-075-B). The collimated light is then reflected off of a 2" silver mirror, M1 (Thor Labs, PF20-03-P01), mounted in a kinematic mirror mount that allows for rotation in the X and Y axis (Thor Labs, KM200). The light is dispersed by a 1200 l/mm volume phase holographic diffraction grating (DG) with a blaze wavelength of 850 nm and a peak efficiency of 95% (Kaiser Optical). All the dispersed light in the first diffraction order is collected by a 2" diameter achromatic doublet lens (L4) with a focal length of 150 mm and design wavelengths of 706.5 nm, 855 nm, and 1015 nm (Thor Labs, AC508-150-B). The dispersed light is brought to a focus onto a linear array detector (LD) (Basler, spL2048-70k) where the spectrum is collected and sent to the CPU. The detector has two rows of 2048 square pixels of size 10 μm on a side. The camera also allows vertical binning so the effective pixel size is 10 μm wide by 20 μm tall. The focal length ratios of the collimating lens (L3) and the focusing lens (L4) dictate a 2x imaging magnification (see eqn. 4.8) so the 20 μm pinhole image will just fit on the 20 μm tall pixel size.

Optical Pupil Slicer

The purpose of this thesis is to implement an optical pupil slicer (OPS) into the SD-OCT system and measure its effects. A lengthy discussion on how optical slicers work is left

to chapter 4 and the specific implementation in the SD-OCT system is left to chapter 5. At this point it is simply mentioned that the OPS is placed in the system spectrograph after the collimating lens, L3, and before the diffraction grating, DG. In order to aid in the process of measuring the SD-OCT system performance both with and without the OPS a setup shown in fig. 3.2 is implemented. The spectrograph mirror M1 is made to be removable so that when it is in place the collimated light is directed towards the diffraction grating, DG, and is focused onto the linear detector, LD, by a camera lens, L4. If this mirror, M1, is removed then the collimated light continues toward two 2" silver folding mirrors (M2 and M3) (Thor Labs, PF20-03-P01) that changes the light direction by 180° and directs it to the entrance of the OPS. The light exiting the OPS is reflected off of another 2" silver folding mirror (M4) (Thor Labs, PF20-03-P01) and sent towards the diffraction grating, DG, and follows the same optical path as the light would with M1 in place. By including or excluding mirror M1 the spectrograph can quickly and easily be changed from a non-sliced spectrograph to a sliced spectrograph.

3.2.2 Results from the SD-OCT System

The SD-OCT system is able to image samples and produce images with high-resolution in a timely fashion. The imaging parameters and characteristics can be determined from the hardware parameters in tables 3.2 and 3.3 and from the general OCT theory presented in section 3.1. A summary of the SD-OCT system imaging parameters and characteristics can be found in table 3.4.

The sensitivity of the instrument was measured by placing a silver mirror in the sample arm (Thor Labs, PF10-03-P01) and recording 1024 interference spectra with a reference arm physical delay of 0.25 mm. The resulting averaged a-scan can be seen in fig. 3.4. The SNR is measured as the difference between the peak signal (-5.63 dB) and the average noise floor (-41.35 dB) and results in a SNR value of 35.72 dB. A neutral density filter (ND) with an optical density (OD) of 4.0 (Thor Labs, NE240B) was placed after the collimating lens (L1) in the SD-OCT system (see fig. 3.2). The optical power measured after the pinhole, PH, for the reference arm was 1.40 μW and for the sample arm it was 1.78 μW, resulting in a fringe contrast of -0.0305 dB; this factor must be subtracted from the measured SNR to correct for non-ideal optical power fringe contrast. The resulting SNR is therefore 35.75 dB. The maximum power that can make it through the pinhole from the sample arm (with no ND) is 1.3 mW. An integration time of 6.5 μs was used to collect the a-scan and completely fill the dynamic range of the camera. The maximum integration time of the camera is 1 ms so a factor of 0.65% less light could be collected, resulting in an optical power of 11.57 nW. The ratio of the maximum to minimum sample power is 50.51 dB. The sensitivity in SD-OCT is defined as the SNR (35.75 dB) plus the ratio of the maximum optical power to the minimum optical power from the sample (50.51 dB), therefore the sensitivity of the

SD-OCT Imaging Parameters	
Parameter	**Value**
Axial Resolution (n=1.0)	3.7 μm
Axial Resolution (n=1.4)	2.6 μm
Lateral Resolution (n=1.0)	5.2 μm
Lateral Resolution (n=1.4)	3.7 μm
Depth of Field (n=1.0)	197.6 μm
Depth of Field (n=1.4)	141.1 μm
Max. Lateral Spot Width (n=1.0)	394.6 μm
Max. Lateral Spot Width (n=1.4)	281.9 μm
Max. Scan Depth (n=1.0)	3.78 mm
Max. Scan Depth (n=1.4)	2.70 mm
GM scan precision	1.1 μm
Typical Scan Step	3.4 μm
Typical Lateral Scan Range	3.5 mm by 3.5 mm
Typical Lateral Scan Samples	1024 by 1024
Typical Exposure Time	200 μs
Typical B-Mode Scan Time	300 ms
Sensitivity	86 dB

Table 3.4: The imaging parameters and characteristics for the SD-OCT system and a typical scan setup.

SD-OCT instrument, as measured at 0.25 mm delay, is 86.26 dB. Likely the sensitivity for the instrument is higher than this value due to sub-optimal signal processing to generate the a-scan.

Although a single sensitivity number of 86.26 dB was reported, the sensitivity of the SD-OCT instrument is dependent on the physical delay in accordance to the spectral coherence envelope (see section 3.1). A full in-depth analysis of the spectral coherence envelope of the SD-OCT system is left to chapter 5 whereby it is compared to the results obtained with the optical pupil slicer. Nevertheless an a-scan produced from a mirror in the sample arm with various different delay positions can be seen in fig. 3.5(a) along with corresponding interference spectra in fig. 3.5(b). It can be seen that as the delay increases the SNR decreases, which in effect decreases the sensitivity of the SD-OCT instrument as a function of delay.

Since the sensitivity decreases exponentially as a function of delay and the signal returning from a highly scattering sample decreases exponentially as a function of depth (see section 3.1), one way to increase the SNR at large imaging depths is to make the delay equal to zero at a large imaging depth. This may be realized by increasing the physical

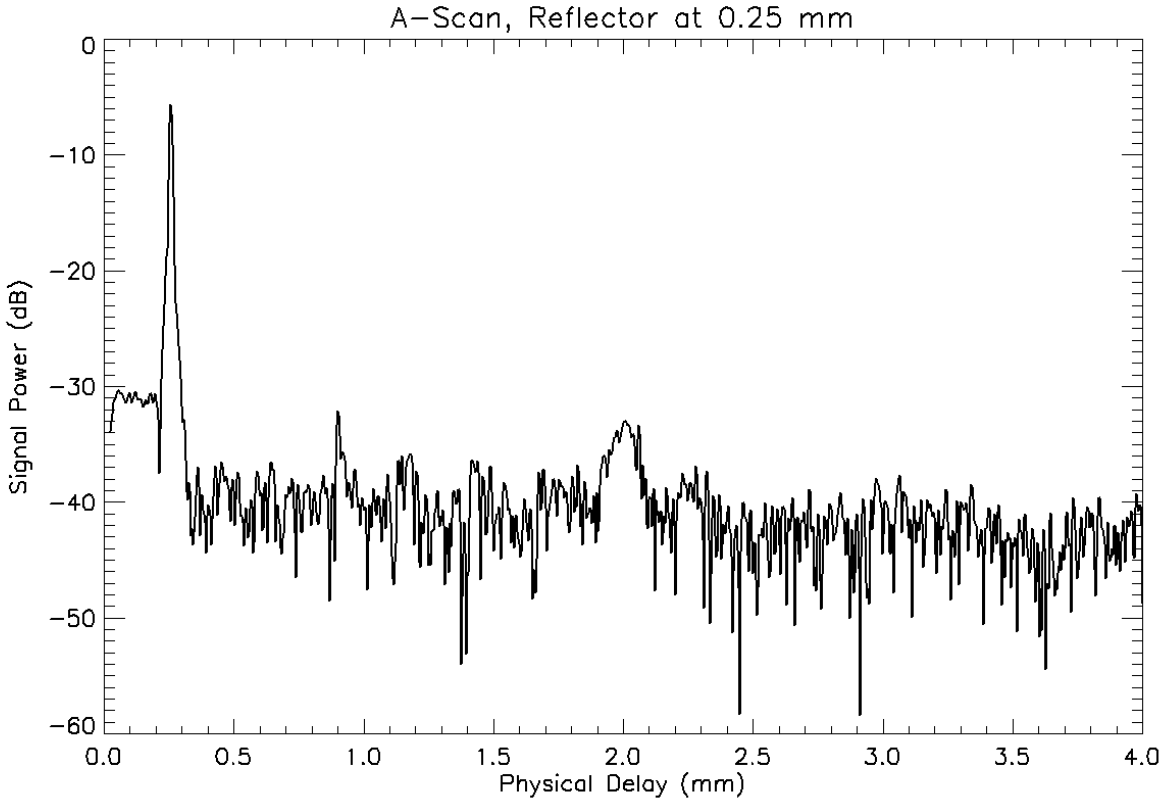

Figure 3.4: An A-scan produced with a silver mirror in the sample arm with a neutral density filter (OD=4.0) and a reference delay of 0.25 mm.

path length of the reference arm so the zero OPD position lies somewhere inside the sample, as opposed to above the sample, as is typically done in SD-OCT [18]. This provides a way to probe depths larger than the commonly accepted maximum imaging depth given by eqn. 3.6, and even beyond commonly accepted maximum imaging depths based on SNR [2, 54]. An example image using this technique was produced with the SD-OCT system. The target was a USAF 1951 resolution target (Edmund Optics, NT38-257), section #0-2 with line widths of 466 μm, imaged through 3.3 mm of chicken breast tissue, corresponding to an index of refraction of about $n = 1.4$. The classically stated maximum imaging depth for this system is about 2.70 mm (see table 3.4) and traditional light transport theory would state the practical imaging depth is even less [49], however the resulting image in fig. 3.6 clearly shows that the lines from the target can be imaged through 3.3 mm of tissue. The target was tilted at about 8° from the nanomotion translation stage axis of motion. The quality of the resulting image is not too great but it demonstrates that reversing the sensitivity of the SD-OCT instrument can have great impact.

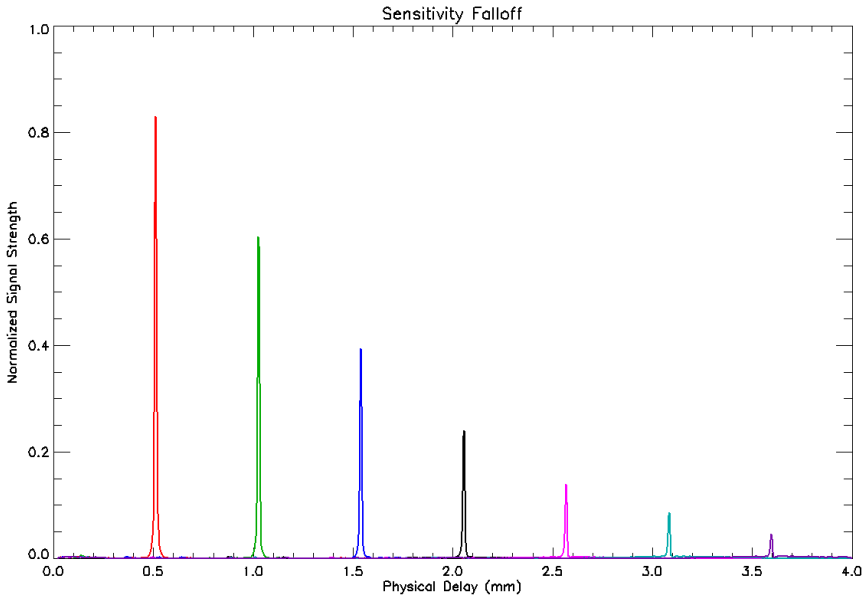

(a) A-scan

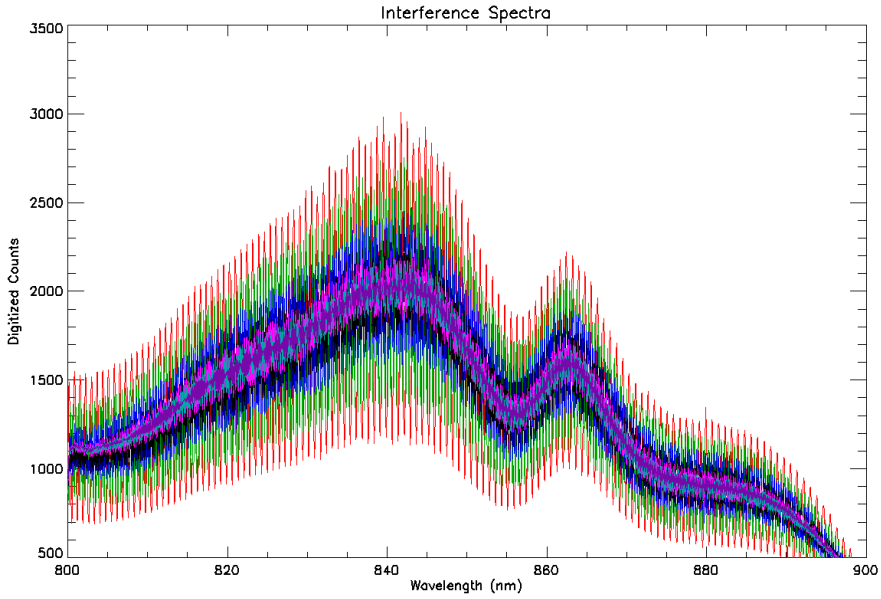

(b) Interference Spectra

Figure 3.5: An a-scan produced with a silver mirror in the sample arm and various delay positions induced by the reference arm.

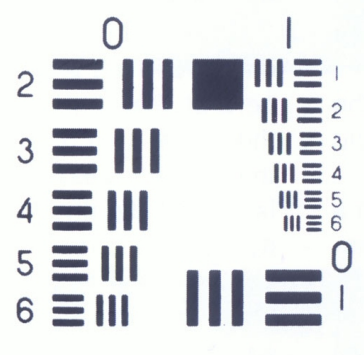

(a) USAF 1951 Target

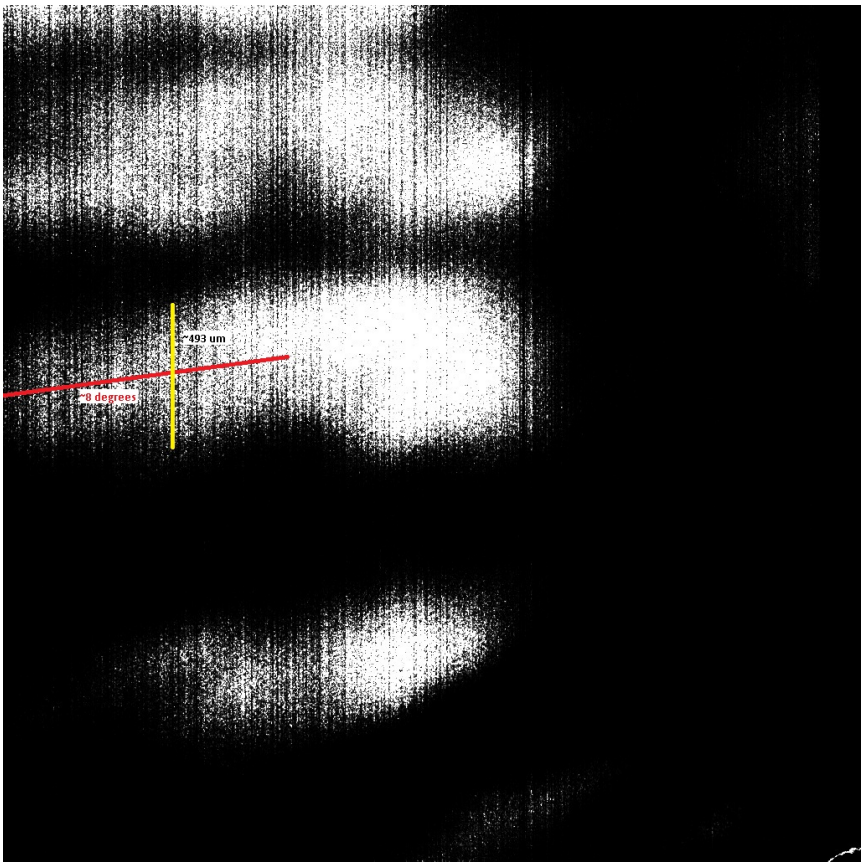

(b) SD-OCT En-Face Image

Figure 3.6: Section #0-2 of the 1951 USAF resolution target imaged through 3.3 mm of chicken breast. The target was tilted at 8°.

Chapter 4

Optical Slicers

The fundamental operating description of an SD-OCT system was discussed in chapter 3. In there we saw that the depth-imaging characteristics are heavily dependent on the performance of the spectrograph used to record the interfered light. The maximum unaliased imaging depth was seen to depend on the wavelength separation between spectral measurements, $\Delta\lambda$, and the attenuation falloff envelope function, called the spectral coherence envelope, depended on the spectral bandpass in a spectral measurement, $\delta\lambda$. In OCT the amount of light returning from a sample depth decreases exponentially with depth according to photon transport theory (see section 2.3.1), therefore in most tissue imaging the imaging depth is limited by SNR, or sensitivity of the instrument [54].

The sensitivity of an SD-OCT system is characterized by the spectral coherence envelope, and therefore by the performance of the spectrograph. A general treatment of dispersive spectrographs will be given in section 4.1 with practical considerations towards the types of dispersive spectrographs found in SD-OCT. The metrics used to define the performance of spectrographs, namely the resolving power, R, and the throughput efficiency, T, will be given. These two standard metrics can be used to define the quality factor, Q, of the spectrograph. Two standard techniques to improve the resolving power will be discussed and will be shown to be lossy methods that decrease the throughput efficiency. The sensitivity in SD-OCT depends on the resolving power, R, and the speed-efficiency in SD-OCT depends on the throughput efficiency, T. Therefore for high-speed high-performance SD-OCT applications the quality factor of the spectrograph is an appropriate metric for quantifying the SD-OCT system. A device known as an optical slicer is able to fundamentally improve the quality factor for a given spectrograph design and therefore fundamentally improve the performance of the SD-OCT system. The basic theory and operation of optical slicers will be given in section 4.3. An actual implementation of a specific kind of optical slicer, called an optical pupil slicer, was constructed and the performance evaluation was performed; these results will be presented in section 4.4.

4.1 Dispersive Spectroscopy and Spectrographs

Spectroscopy in optics is the study of the different frequency, or wavelength, components of a given light source, and using this information to deduce additional information about a given problem. A classic example of optical spectroscopy in the biomedical field is pulsed oximetry, where the optical spectrum of blood is used to measure the oxygenation of hemoglobin [51]. In puled oximetry only two wavelengths are needed, but more advanced problems require knowledge of many more different wavelengths. Typically in spectroscopy the measurement of the optical power spectrum of the given light source is performed, and the device that performs the spectral measurement is called a spectrograph. The goal of any spectrograph is to be able to distinguish at least two different wavelengths from one another. The accuracy and quality of the measured spectrum depends on the nature of the application and there are predefined metrics to quantify measured spectra. The two most important metrics are resolving power, R, and the signal-to-noise ratio (SNR). The resolving power is a relative quantification of smallest wavelength difference between any two given wavelengths and still be distinguished from one another, it is defined mathematically as

$$R = \frac{\lambda_0}{\delta\lambda}, \tag{4.1}$$

where $\delta\lambda$ is the smallest wavelength difference that can be resolved, also known as the spectral resolution, and λ_0 is the mean wavelength about which the two wavelengths are being distinguished from one another. As an example, a spectrum that is able to tell the difference between the wavelengths 849.5 nm and 850.5 nm would have a spectral resolution $\delta\lambda$=1 nm and a mean wavelength λ_0=850 nm, therefore according to eqn. 4.1 will have a resolving power R=850. There are many different methods of measuring an optical power spectrum, and there are many different types of spectrographs. The method most relevant to SD-OCT and our application is measuring the spectrum by spatially dispersing the light and measuring the optical power as a function of position; this is known as dispersive spectroscopy and the instruments are dispersive spectrographs.

The goal of a dispersive spectrograph is to distinguish two different wavelengths from one another by spatially resolving them, i.e. by recording an image of the light distribution and using prior knowledge that each spatial position corresponds to a different wavelength. The clearest example of dispersive spectroscopy in everyday life is by looking at a rainbow; the colours, or wavelengths of light, are located in different positions in the sky and therefore are located in different positions on our retina thereby forming an image. In the case of the human eye we are able to distinguish the colours from one another independent of location because our image sensors (cones) are narrowband and produce a different signal for different colours, or wavelengths, and our brain is highly calibrated and is able to inter-

pret these signals as being different known colours [6]. In the case of conventional imaging technology, the detectors used typically have broadband responsivity and are not good at distinguishing different wavelengths. The closest we can come to mimicking a human cone is by placing a known narrowband colour filter over the detector so the recorded signal will be the total optical power of the source light in the wavelengths associated with the colour filter. This is typically how colour images are produced in digital photography, by using a Bayer colour filter over millions of pixels (single element detectors) [6]. This method works well for colour photography, where only three colours are measured (red, green, and blue) so only three different filters are needed; however, for hyper-spectral applications it becomes terribly inconvenient, or impossible in high-precision applications, to have numerous different colour filters placed over each detection element. Instead of a colour filter approach, in dispersive spectroscopy the light in each spatial position is recorded with an identical detector characterized by a general responsivity, however the spatial calibration of the different wavelengths becomes critical in wavelength differentiation.

In an optical system the light is spatially altered in deterministic ways by elements such as mirrors, lenses, prisms, and diffraction grating. The way in which light is affected by these elements is determined completely by measurable properties such as radii of curvature, index of refraction, relative orientation geometry, and groove spacing. A simple dispersive spectrograph comprises of a dispersive element such as a prism or diffraction grating, a focusing lens, and a detector. The detector may be comprised of a single element that moves spatially along the dispersive direction of light, many smaller single element detectors (pixels) orientated along the dispersive direction in an array, or a single element fixed in place while the dispersive element is moved to change the central mean wavelength incident on the detector. All these configurations achieve the same end result of recording an optical power spectrum and have numerous advantages and disadvantages associated with each depending on the application, however the one implementation we will focus on is the detector comprised of many smaller single element detectors in an array, i.e. a camera. This configuration is the one typically seen in SD-OCT instruments and has the advantage of recording the entire optical power spectrum with a single exposure.

We saw in section 3.1.1 that the signal quality for SD-OCT instruments is dependent on the spectral resolution, $\delta\lambda$, as well as the wavelength separation between each pixel, $\Delta\lambda$. In a dispersive spectrograph using a transmission diffraction grating, the light is angularly dispersed upon exiting the grating and is described according to the grating equation,

$$m\lambda = d_g \left(\sin\left(\theta_i\right) + \sin\left(\theta_t\right)\right), \tag{4.2}$$

where m is the diffraction order, d_g is the groove spacing typically quoted in inverse units of lines per millimetre (l/mm), θ_i is the angle incident onto the diffraction grating as measured from the surface normal, and θ_t is the dispersed angle transmitted as measured from the

surface normal. For a complete description of these terms and the grating equation refer to section 2.2.3. For the configuration relevant to SD-OCT the position of the diffraction grating is fixed and the angularly dispersed light is focused onto the camera using a lens system with an effective focal length, f_L. Assuming the small angle approximation ($\theta \leq 10^\circ$) we may describe the position of the light on the focal plane using the paraxial ray trace equations (see eqns. 2.10 and 2.11) and arrive at the result,

$$\lambda(x_i) = \frac{d_g}{m}\left[\sin\left(\arctan\left(\frac{x_i}{f_L}\right) + \theta_B\right) + \sin(\theta_i)\right], \tag{4.3}$$

where x_i is the position on the focal plane relative to the blaze position, x_B, associated with the blaze wavelength, λ_B, and θ_B is the dispersion angle associated with the blaze wavelength. Again, refer to section 2.2.3 for a definition and description of these terms. Suffice it to say that the above eqn. 4.3 is sufficient to describe the spatial position, x_i, of the wavelengths, λ, exactly for a transmission diffraction grating and a focusing lens with the aforementioned known parameters and measurable orientation geometries, f_L, d_g, θ_i, θ_B, and observing diffraction order number, m; it is implicit that the blaze angle, θ_B, is a function of the order number, m. Since the size and position of two adjacent pixels are known eqn. 4.3 can be used to determine the wavelength separation, $\Delta\lambda$ between the two adjacent pixels. In an ideal case the bandwidth in a pixel would be equal to $\Delta\lambda$ and therefore the spectral resolution would equal to the wavelength separation within the pixel, i.e. $\delta\lambda = \Delta\lambda$. This situation is physically impossible because it requires the focused spots have zero width. Practically the spots have some width and therefore the spectral resolution is always greater than the wavelength separation in the pixel; spectral resolution is analogous to spatial resolution in a dispersive-based spectrograph.

Spatial resolution was discussed in section 2.2.3 and diffraction limited resolution was defined using eqn. 3.8, known as the Rayleigh criterion. It was seen that the spatial resolution is related to the metric of the spot size, in this case the diameter of the central lobe in the Airy pattern. If two focused spots are separated by a given distance such that the zero intensity location of one spot coincides with the peak intensity of the other spot then the two spots are said to be resolved. The spatial resolution was defined to be half the width of the central Airy lobe, which upon centring about the middle of the lobe corresponds to about 36.75% of the normalized peak intensity and results in about a 20% intensity dip between the two peaks. The full-width at half maximum (FWHM) value corresponds to 42.17% of the Airy diameter, therefore it may be concluded that a FWHM value may also be used to define the spatial resolution with a reasonable degree of accuracy; the intensity dip between the two peaks is about 4%, which is close to the accepted Dawes limit of 5% [1]. This FWHM definition is a more useful result when dealing with focused spots not equal to the Airy pattern since the Rayleigh limit does not correspond with non-

diffraction limited spots. In the case of Gaussian spot profiles the intensity dip in between the peaks separated at the FWHM is about 8%, a well resolvable criterion.

The spectral resolution, $\delta\lambda$ in a dispersive spectrograph is equal to the FWHM of the bandpass in a pixel in accordance with the previous FWHM definition for spatial resolution assuming the bandpass in a pixel is approximately Gaussian, which is a good first order approximation. The bandpass function for a pixel may be given as the convolution of the spatial pixel response function (typically a RECT function) with the spatial light distribution function of the focused spot, which is approximately Gaussian, but strictly the Airy pattern convolved with the image pattern. The resulting convolution is therefore approximately Gaussian if the FWHM of the spatial light distribution function is similar to the full support of the spatial pixel response function. The convolution function will take on the shape more dominated by the larger supported function, therefore this approximation breaks down when the pixel size is much larger than the FWHM, in which case the convolution resembles the pixel function more closely.

Consider each pixel to be the convolved Gaussian function centred about the pixel location, therefore if two pixels are separated by some distance, x, then two Gaussian functions will be separated by the same distance, x. In accordance with the FWHM definition of spatial resolution, the Gaussian function must be separated by the FWHM value, and therefore the pixels must be separated by the same distance. If there are any pixels with a separation distance smaller than this value then the intensities will be too similar to each other and the two spots will be unresolvable. The FWHM value, which determines pixel separation distance, can be converted to wavelength difference, $\delta\lambda$, by eqn. 4.3. The number of pixels, J, spanning the recorded spectrum multiplied by the ratio of wavelength separation divided by the spectral resolution gives the number of resolution elements, N_{res}, in a dispersive spectrograph,

$$N_{res} = J\frac{\Delta\lambda}{\delta\lambda}. \tag{4.4}$$

Not only does the resolving power matter in a dispersive spectrograph, the SNR is also important. If the noise introduced in the recorded spectrum is larger than the variation in the intensity dip between any two resolution elements then the spectrum looses resolving power and may be unresolved. For example, consider a broadband flat spectrum with a fully absorbing feature with a spectral width equal to the spectral resolution, $\delta\lambda$. The recorded spectrum with infinite SNR would show an intensity dip at the absorption wavelength with the dip equal to the definition of resolvability; using the FWHM definition from above this would be about 8%. If the SNR causes the intensity to vary at the 8% level then it is possible that the recorded intensity at the dip location will increase to be equal to the intensity of the rest of the spectrum, therefore the absorption feature is unresolved. The spectral SNR required is heavily application dependent, and typically problems are defined

by a minimum SNR at a given spectral resolution, or resolving power. In the simplest case where SNR is proportional to the total amount of light collected then there is a one-to-one correspondence with resolving quality and total signal. This situation occurs when the noise is dominated by photon noise and photon statistics are relevant (see section 2.3.2).

The total amount of light, or optical power, collected by a dispersive spectrograph is never equal to the total amount optical power emitted by the source in practise. Losses occur at every optical surface and the conversion efficiency from photons to electrons (quantum efficiency, η) is very often less than 100%. Additional losses occur due to the efficiency of the diffraction grating. Typically a spectrograph with a diffraction grating is designed to record only a single order number, e.g. $m = 1$; however, diffracted light will enter all orders. Some types of diffraction gratings, such as volume phase holograph transmission gratings, may be designed such that as much light as possible will enter a prescribed order number [3, 7]. The relative amount of optical power for a given wavelength in the designed order to the total amount of optical power at that wavelength in the source is defined as the efficiency of the grating at that particular wavelength; an efficiency as a function of wavelength may be defined and measured for any diffraction grating. Combining all the losses in a dispersive spectrograph, an overall throughput, T may be defined as the ratio of the total optical power recorded, I, to the total optical power input, I_0,

$$T = \frac{I}{I_0}. \tag{4.5}$$

By defining a desired SNR in the recorded spectrum, and using the throughput efficiency, T, the required exposure time with a total optical source power input to the spectrograph may be found.

How does one determine the quality of a dispersive spectrograph? We already mentioned that the resolving power, R, is a good metric for determining how well the spectrograph can resolve two different wavelengths from one another about their central wavelength. We also mentioned that the SNR may affect this measurement so the amount of light is also an important metric, and is coupled with the resolving power. The same amount of light dispersed over a larger (large R) area will have less optical power per pixel and lower SNR per channel than if the light were dispersed over a smaller area (small R). The absolute SNR in a spectrograph, or the recorded spectrum, is not a good quality indicator of the instrument, though the efficiency at which the spectrograph utilizes the input light is a good quality indicator; we have defined this as the throughput efficiency, T. A dispersive spectrograph quality metric may be defined as the resolving power, R, multiplied by the throughput efficiency, T,

$$Q = R \cdot T = \frac{\lambda_0}{\delta\lambda} \cdot \frac{I}{I_0}. \tag{4.6}$$

The hardware configuration determines the resolving power, and in the types of dispersive spectrographs with fixed detectors and diffraction gratings this metric is constant. For a given application with a single instrument the SNR may increase or decrease but the throughput efficiency will remain constant for every application since it is only hardware dependent. Given that both the resolving power and the throughput efficiency are completely determined by the hardware of a given dispersive spectrograph, the combination of these two factors in defining the quality factor of the instrument is a useful way to characterize the performance.

In many applications it is desirable to have as high a resolving power as possible since finer spectral features can be resolved. The resolving power in a dispersive spectrograph is often limited by the size of the focused spots, rather than the dispersing power of the diffraction grating or prism. The maximum obtainable resolving power based on diffraction theory for a diffraction grating based spectrograph is given as

$$R_{max} = \frac{mD_b}{d_g}, \tag{4.7}$$

where m is the order number, D_b is the diameter of the beam incident on the diffraction grating in units of millimetres, and d_g is the groove spacing of the grating (mm/line) [8, 47]. It is often the case that the pixel size and focused spot size decrease the resolving power from this value, although this is not always true, for example in a poorly designed spectrograph. We mentioned above that the spectral resolution, $\delta\lambda$, is always greater than the wavelength range in a pixel, $\Delta\lambda$, and this was because the focused spots had finite width. In order to increase the resolving power of the spectrograph the spot size must decrease in width to the about the same size of a pixel, at which point the approximation for Gaussian bandpasses breaks down and our resolvability definition must take on a new meaning. Once the spot size is small enough the spectral resolution and wavelength range are approximately equal ($\delta\lambda \simeq \Delta\lambda$) and the spectrograph resolving power is maximized for the given hardware configuration. The overall resolving power may be increased by decreasing the wavelength range and keeping the spot size the same size of the pixels. Decreasing the wavelength range may be performed by a couple of methods: first, by increasing the angular dispersion induced by the dispersive element, and second, by increasing the focal length of the camera lens.

In a diffraction grating based spectrograph both these points are evident from examining eqn. 4.3. The dispersive power is inversely proportional to the groove spacing so having a small d_g means more lines per millimetre and a larger angular spread for a given wavelength region. Increasing the focal length, f_L, of the camera lens is seen to inversely scale the independent variable, or in this case the position in the focal plane relative to the blaze wavelength location, x_i. In the first case of using a higher power grating the prac-

tical consequences are that the input-output angle[1] increases so the system may become unwieldy if these angles get larger than 90°, the large angular range will likely increase the complexity and/or size of the camera lens thereby driving up the cost of the spectrograph significantly, and the maximum diffracted wavelength is limited to $\lambda_{max} \leq 2d_g$ [8]. The general design philosophy is to use as high power a diffraction grating as possible without imposing on other practical engineering considerations, for example, an angular spread of larger than 10° will require highly complex lens systems. In the second case of increasing the focal length of the camera lens, the light will be spread over a larger area for a given dispersive angular region since the light has to travel a longer distance, but the spot size also increases by the same factor the focal length was increased. This is because an object-image size multiplied by the propagation angle is an invariant in an optical system (see eqn. 2.12); by increasing the focal length by a given factor, the propagation angle decreases by that same factor (in the small angle paraxial approximation), and therefore the image size must increase by the same factor. A visual example of this is clear to anyone that has performed some amateur photography: using a longer focal length lens makes the image bigger. The spot size must be decreased by some other means in order to keep it about the same size of the pixels when the camera focal length increases.

In a dispersive spectrograph the input light is typically emitted from a finite source size, such as a pinhole aperture or fibre optic cable. These finite source areas serve as the image on the focal plane on the detector with appropriate magnification scaling factors due to the optics. The source emits light and a cone is collected and collimated by a lensing device, typically a refractive lens, but may be a reflective lens. This collimated light interacts with the diffraction grating either reflecting or transmitting at different angles depending on the wavelength. Afterwards the light is focused onto the detector by another lensing device (refractive or reflective). The size of the focused spot is equal to the size of the source object multiplied by the ratio of the camera focusing lens focal length to the source collimating lens focal length,

$$h_i = h_o \frac{f_{cl}}{f_{sl}}, \tag{4.8}$$

where h_i is the image size, h_o is the object size, f_{cl} is the focal length of the camera focusing lens, and f_{sl} is the focal length of the source collimating lens. In accordance with our above discussion on the optical invariant, it can readily be seen in eqn. 4.8 that the image size is a multiple of the object size depending on the propagation angles, which are determined by the focal lengths. It may be seen that one way to decrease the focused spot size is to ensure the ratio of the focal lengths is small, either by having a large focal length for the source lens, or a short focal length for the camera lens. Since a long focal length for the camera

[1]This is for a transmission grating not a reflection grating.

lens is desired to reduce $\Delta\lambda$, to make small spots the focal length of the source lens should be even larger. In our analysis we have not considered the collimated beam diameters, D_b, which can play an important roll considering the maximum resolving power is partially determined by it (see eqn. 4.7); it is important to keep the diameter large enough that the resolving power is not limited by the diffractive effects of the grating. The amount of light collected and collimated by the source lens is determined by the ratio of the numerical aperture (NA) of the lens over the NA of the source up to a maximum of 1 (obviously we cannot collect more light than is emitted even if our acceptance NA is larger)[2],

$$T = \left(\frac{D_{sl}}{D_s}\right)^2, \tag{4.9}$$

where D_{sl} is the diameter of the source lens and D_s is the diameter of the collimated source beam. By increasing the focal length of the source lens the diameter of the source beam incident on the source lens increases. Once the diameter of the source beam is larger than the diameter of the lens, throughput loss occurs. This is the first instance where we see a trade-off between resolving power and throughput efficiency; by increasing the focal length of the source lens the spot image size decreases—increasing the resolving power—but the amount of light collected decreases and the throughput efficiency decreases. By using the definition of spectrograph quality factor in eqn. 4.6 a system configuration may be examined and an optical hardware configuration may be found that maximizes the quality factor. An example of this analysis is performed with a hardware configuration similar to the SD-OCT system spectrograph. The hardware parameters are summarized in table 4.1, and the resolving power, throughput efficiency, and quality factor graphs are seen in figs. 4.1-4.3. These results assume a circular source object that is uniformly illuminated.

From figs. 4.1-4.3 it can be seen that as the focal length of the collimating lens increases (increasing f/#) the throughput remains constant until about f/4.8, where the throughput starts to decrease. At f/4.8 the diameter of the source beam is equal to the diameter of the collimating lens so all light from the source is being collimated. It is also seen that as the focal length of the collimating lens increases the resolving power increases because the bandwidth in a pixel is decreasing. The resolving power starts to plateau because once the spots start getting smaller than a pixel then the bandwidth is limited by the pixel size. The quality factor plot (fig. 4.3) shows a peak in spectrograph quality when the collimating lens is f/4.8, or when the focal length is about 120 mm. We see that the quality factor, Q, is a very helpful tool in dispersive spectrograph design. The SD-OCT system spectrograph, however, employed a focal length of 75 mm, or f/3, for the collimating lens because the divergence angle from the pinhole is fixed and the slicer was designed to work with a beam

[2]For a discussion on numerical aperture refer to eqn. 2.15.

Simulation Input Parameters	
Parameter	**Value**
λ_0	850 nm
Source Aperture	10 μm
Camera lens focal length	150 mm
Source NA	0.103
Collimating lens diameter	25.4 mm
Grating power	1200 l/mm
Blaze wavelength	850 nm
Pixel width	10 μm
Collimating lens focal length	25 mm - 500 mm
Slit Width	1 μm - 10 μm

Table 4.1: Input hardware parameters to calculate the throughput efficiency, resolving power, and ultimately the quality factor for a spectrograph as a function of both slit width and focal length of the collimating lens.

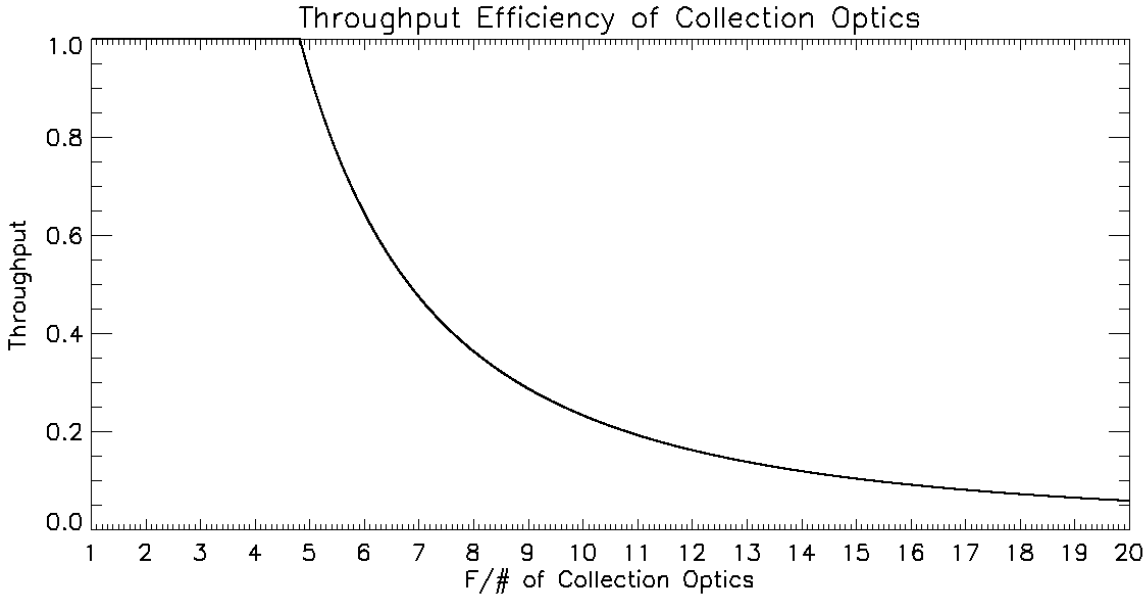

Figure 4.1: A plot showing the throughput efficiency of the spectrograph as a function of the collimating lens f/#.

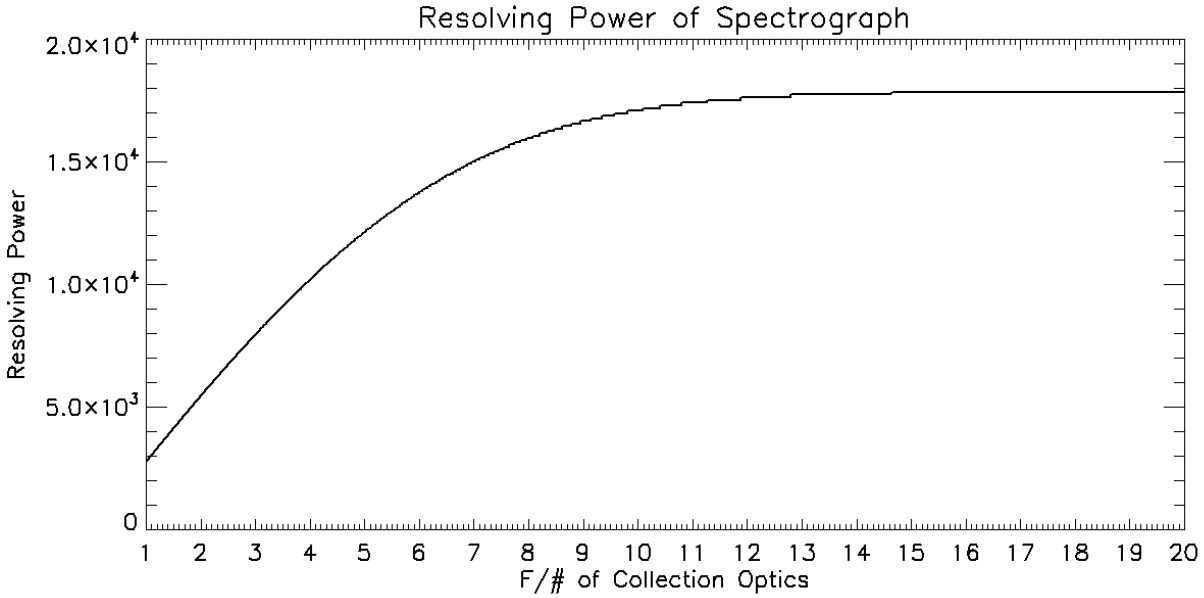

Figure 4.2: A plot showing the resolving power of the spectrograph as a function of the collimating lens f/#.

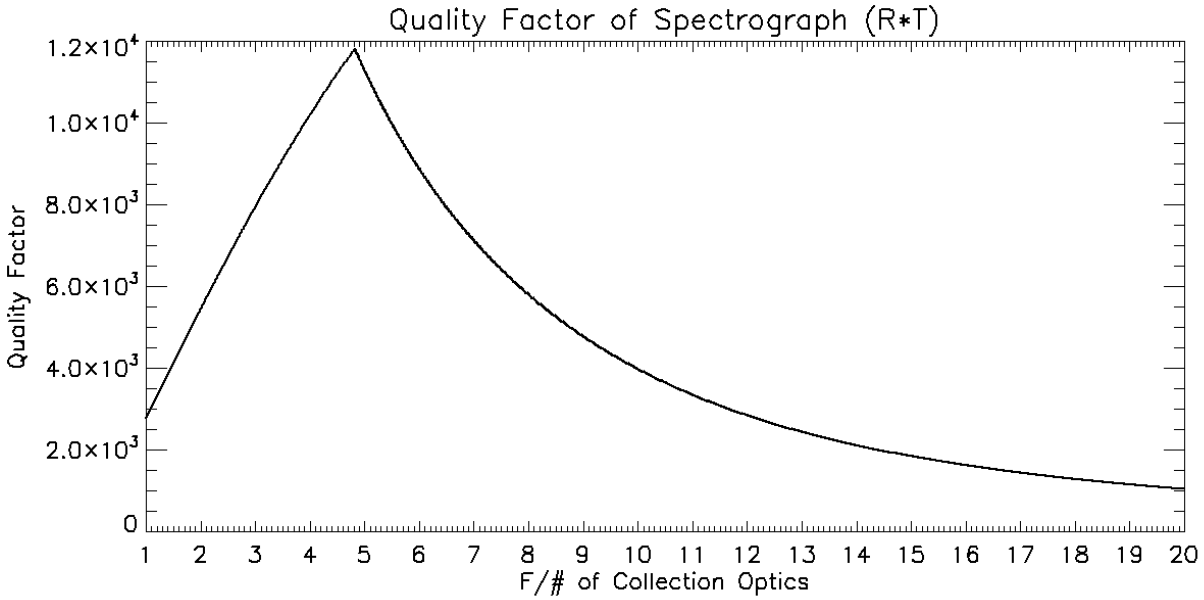

Figure 4.3: A plot showing the quality factor of the spectrograph as a function of the collimating lens f/#.

diameter no larger than 15 mm (22 mm clear aperture). This simple analysis is shown to not take into account all aspects of a spectrograph design.

Increasing the focal length of the collimating lens is not the only way to reduce the spot size on the focal plane—a slit may be used at a conjugate focal point in the spectrograph. Slits have a long history in optics, but the first documented evidence of using a slit to increase the resolving power of a spectrograph occurred in 1802 by William Hyde Wollaston [53, 62]. A slit is an aperture with a narrow width in the dispersive direction but a tall height in the cross-dispersive direction that is placed at a conjugate focal point so that the final focused spot is narrower than it would be if no slit were used. Since the resolving power is dependent on the spot width, a slit is seen to increase the resolving power. Slits are very easy to implement and make intuitive sense in a spectrograph so they are advantageous on several fronts, as can be testified by their use in virtually all dispersive spectrographs for the past 200 years! The only obvious disadvantage to a slit is that they are very lossy because they block most of the light from a source. Assuming a source object can be modelled as a uniform circular disc, the throughput efficiency of a rectangular slit with height larger than the source object can be expressed analytically as,

$$\begin{aligned} T_{slit} &= \frac{4}{\pi r_s^2} \int_0^{w_s} \sqrt{r_s^2 - x^2}\, dx \\ &= \frac{2\left(w_s \sqrt{r_s^2 - w_s^2} + r_s^2 \arcsin\left(\frac{w_s}{r_s}\right)\right)}{\pi r_s^2}, \end{aligned} \tag{4.10}$$

where r_s is the radius of the source object and w_s is the half-width of the slit. The slit throughput derivation assumed the slit was placed exactly on top of the source object, rather than at a different conjugate focal point. The difference between the two techniques is negligible when the source object is many times larger than the diffraction limit, but close to the diffraction limit a more advanced model is needed. By following a similar analysis for evaluating the spectrograph quality factor by use of the resolving power and the throughput efficiency due to a slit, we arrive at the results presented in figs. 4.4-4.6. The spectrograph hardware parameters are also summarized in table 4.1. For the slit spectrograph system the focal length of the collimating lens was chosen to be 75 mm.

In fig. 4.4 it can be seen that the throughput efficiency is almost linear with respect to the slit width except when the slit is almost the same size as the source object. The resolving power increase from using the slit (fig. 4.5) also shows a near-linear trend, although the slope is small, meaning the spectrograph does not see much improvement from using a slit. This is because the source size is already close to the diffraction limit and the width

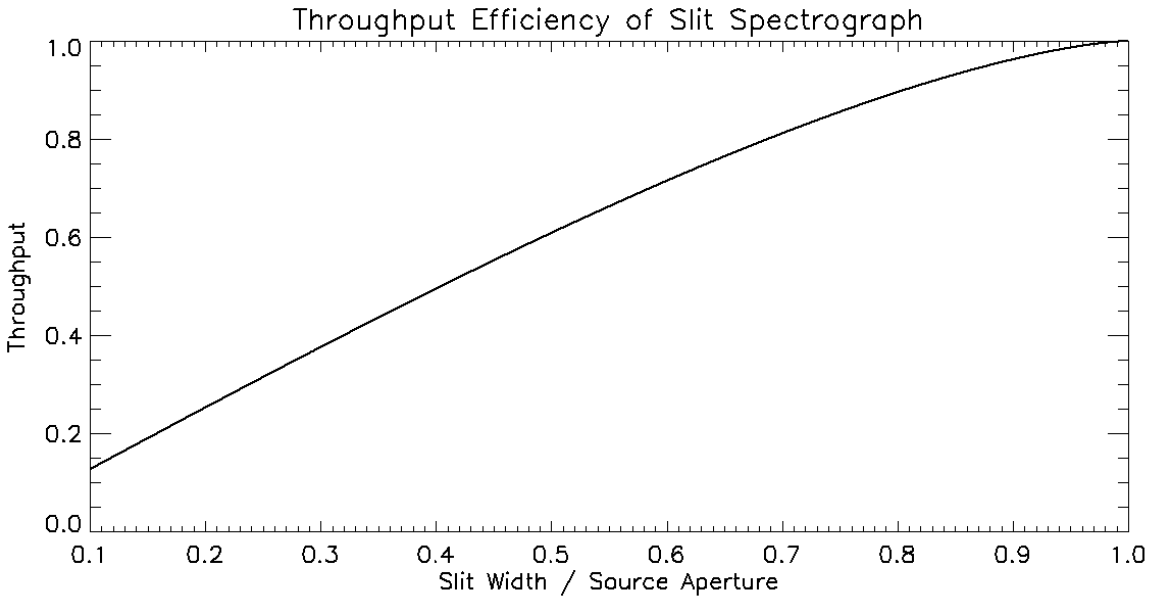

Figure 4.4: A plot showing the throughput efficiency of the spectrograph as a function of the slit width. This is the graphical representation of eqn. 4.10.

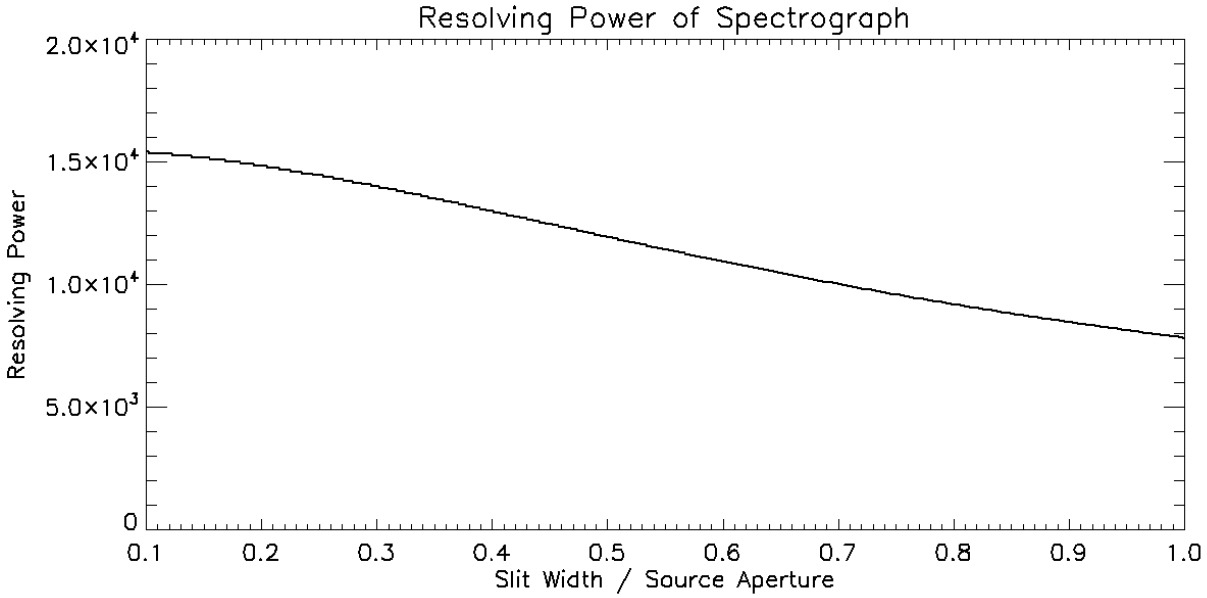

Figure 4.5: A plot showing the resolving power of the spectrograph as a function of the slit width.

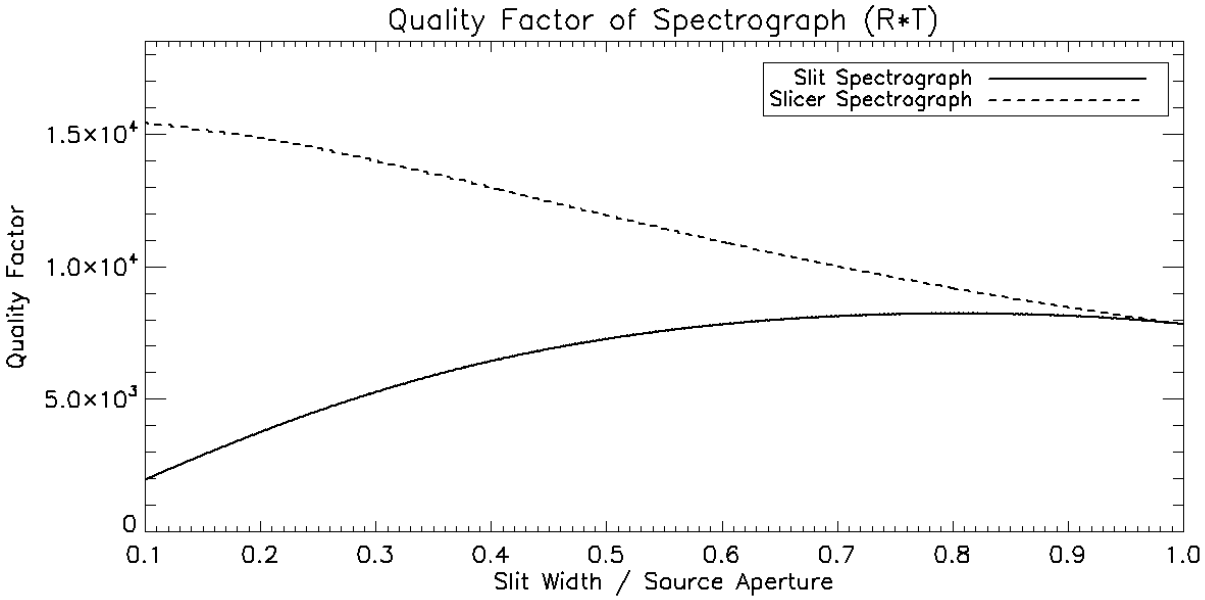

Figure 4.6: A plot showing the quality factor of the spectrograph as a function of the slit width.

of a pixel. Nevertheless the quality factor may be defined for this spectrograph system and it is seen that there is a peak when the slit width is about 8 μm.

For a given hardware configuration for a spectrograph with a slit there will be a maximum quality factor. A fundamental way to improve the quality of a dispersive spectrograph would be to be able to increase the resolving power by a factor larger than the throughput loss. A system that is able to do this perfectly, i.e. with no losses, is also shown in fig. 4.6. Such a device is called a slicer. The subject of slicers in dispersed spectrographs will be the topic of the remainder of this chapter.

4.2 History of Different Designs and Implementations of Optical Slicers

Historically the first optical slicer appeared as an astronomical instrument to reduce the light loss at the slit of a spectrograph [9]. This type of slicer was called the Bowen slicer named after its inventor in 1938. A modified form of the Bowen slicer was conceived in 1972 by Walraven and Walraven and was called the Bowen-Walraven (BW) slicer [56]. This slicer was a solid prism design so while it was robust, the performance was limited. The BW slicer had issues where the slices were not properly aligned, and had limited performance

due to high dispersion through the glass material. Several modifications have been done to the BW slicer and other optical slicer designs have been considered since 1972, such as fibre and waveguide based [15, 52].

Both fibre and waveguide based slicers are not very efficient devices in terms of preserving light throughput, which seems contradictory considering one of the main the purposes of a slicer is to maintain light throughput. In a fibre based slicer the light is typically focused onto a bundle of fibres arranged in a circular geometry and then the bundle of fibres at the output are arranged in a linear geometry. The light coupling efficiency may be approximately given as the core area of the fibre divided by the total area of the fibre (core plus cladding), which in a typical 0.22 NA, 50 μm core fibre optic cable may be on the order of 10% to 15%. Another disadvantage of fibre and waveguide based slicers is that each slice on the output image plane has some separation distance that may require the use of a large detector area.

Optical slicers may have numerous applications, but historically they have been used to increase the performance of a spectrograph without the use of a slit. There may be many designs and implementations of optical slicers but they all basically are based on spatially altering the light distribution in some form. Optical slicers can be broken down into two fundamental categories that depend on where the light manipulation occurs: spot slicers, and pupil slicers.

A spot slicer performs the optical slicing at or close to the focus of the light, therefore it is manipulating the spot profile. For example, the Bowen-Walraven slicer is a spot slicer. These types of slicers are more intuitively obvious because there is a direct comparison to how the slicing is being performed and what is seen at the conjugate focal plane in the spectrograph. Spot slicers are typically easier to conceive than pupil slicers, however they are somewhat harder to implement because of the high precision and alignment required, and also because the slicing hardware needs to be very small.

Pupil slicers, on the other hand, perform the optical slicing in collimated space, or in the pupil plane. Since collimated space is often synonymous with Fourier space in optics it is often less intuitive to think of manipulating the Fourier transform of a spot to change its spatial distribution profile. A pupil slicer offers several advantages over a spot slicer. First the slicing hardware does not necessarily need to be tiny, second the light may be manipulated over large path lengths, third the focused spot shape is independent of the pupil shape, and fourth in that multiple pupil slicers can be run in series to achieve a multiplicative effect. Pupil slicers are based on manipulating the étendue of the beam.

4.3 Design of the 2X Refractive Optical Pupil Slicer

The general design philosophy behind an optical slicer is that it achieves the same resolving power performance boost effect of a slit but with a minimal loss of throughput. This is readily achievable by causing the focused spot size to be reduced in width, or in the dispersive direction dimension. In order to preserve light the focused spot size must increase in length along the orthogonal direction. Since the spectral resolution is only dependent upon the width of the spots in the dispersive direction, an increase in length along the orthogonal direction is acceptable. Typically 2D arrays or pixels with high aspect ratios are used in dispersive spectrographs so having a high aspect ratio focused spot does not reduce throughput; however, care must be taken to ensure the focused spot fits entirely on the detector.

The radiance, L, of an optical system is conveniently defined such that it remains a constant at all locations of a perfect lossless optical system,

$$L = \frac{P/t_e}{A_{EP}\Omega_s \cos\theta}, \tag{4.11}$$

where P/t_e is the total optical source power in Watts given as the mean number of photons, P, per exposure time, t_e, A_{EP} is the area of the entrance pupil in m^2, Ω_s is the solid angle that the source subtends entering the optical system in steradians, and θ is the angle deviation between the source normal and the optical axis in radians [4]. Given a perfect lossless optical system the total amount of optical power, P/t_e, remains constant, and furthermore in the ideal case the source is aligned with the optical axis such that $\theta = 0$ and maximum radiance is obtained. The other two terms in equation 4.11 describe the source and optics geometry, and is known as the étendue, defined by

$$\Xi = A_{EP}\Omega_s \simeq A_s\Omega_{EP}, \tag{4.12}$$

where the approximation is given by eqn. 2.25 in the small angle regime. The étendue in a perfect optical system is constant at all locations and serves as the optical invariant of a system (see section 2.1.5). Because the étendue only depends on the area of the source and the 2D description of the pupil shape, the sub-geometrical description of the area and solid angle may be arbitrarily defined as long as the resulting product remains constant. By changing one variable in the étendue, such as the source area, A_s, the solid angle, Ω_{EP}, must change to keep the product a constant, and therefore to keep the radiance, L, a constant resulting in a lossless system.

A conventional slit in a spectrograph decreases the source area, A_s, but leaves the solid angle, Ω_{EP}, unchanged resulting in a decrease in étendue and therefore a decrease in

Refractive Slicer Element Parameters		
Element	**f_L (mm)**	**Diam. (mm)**
L1	200	25.4
L2	50	25.4
L3	50	25.4
L4	100	50.8

Table 4.2: The focal lengths and diameters the individual elements in the refractive 2X slicer design. Information protected under United States patent [44].

radiance, L: the definition of a lossy optical system. The operation of the slicer aims to keep the area of the source the same, but changes the sub-geometrical description of the spot shape such that the width in the dispersion axis is reduced. Because the source area is kept constant, the solid angle, Ω_s, is also kept constant, however, the sub-geometrical description is changed so that the angular profile corresponding to the dispersive axis results in a constant étendue and a lossless system.

In the case of the conventional slit the source area was manipulated directly by use of an aperture and the remaining optical elements were left unchanged. In the case of the slicer, the optical elements are used to manipulate the sub-geometrical description of the solid angle, Ω_{EP}, directly resulting in an automatic source geometry change such that the width along the dispersive axis is reduced; keeping the solid angle, Ω_{EP}, constant results in keeping the source area, A_s, constant and therefore resulting in a lossless optical system.

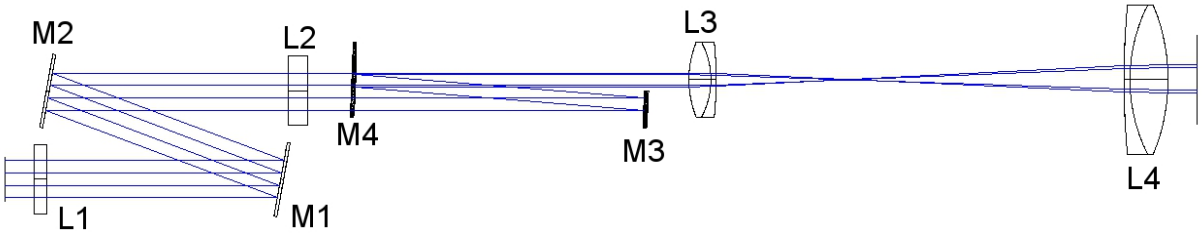

Figure 4.7: A diagram showing the optical design for the 2X refractive pupil slicer. L1 and L2 are cylindrical lenses used for beam compression, M1 and M2 are redirecting mirrors, M3 and M4 are mirrors used for pupil slicing, and L3 and L4 are spherical lenses used for beam expansion. Figure protected under United States patent [44].

An optical pupil slicer was chosen to have slicing power of 2X because it is the simplest implementation of all optical pupil slicers, and it is able to provide a large reduction factor that should be measurable in almost all scenarios. The slicer was chosen to be constructed using refractive optics because these types of components are generally available off the shelf, easy to implement, and provide an on-axis design.

Orientation of the Slicer Elements					
Element	**X (mm)**	**Y (mm)**	**Z (mm)**	**Tilt X**	**Tilt Y**
L1	0.0	0.0	0.0	0.0	0.0
L2	30.0	0.0	82.55	0.0	0.0
L3	33.75	1.875	217.55	0.0	0.0
L4	33.75	1.875	356.81	0.0	0.0
M1	0.0	0.0	80.0	0.0	-10.28°
M2	30.0	0.0	0.0	0.0	-10.28°
M3	30.0	0.0	197.55	1.1°	-2.28°
M4	33.75	1.875	97.55	1.1°	-2.28°

Table 4.3: The locations of the elements in the refractive slicer. Measurements are referenced to the centre of L1, which coincides with the centre of the input beam. All measurements are to the centre of the optical element except the re-arranging mirrors. The measurement locations for M3 and M4 are the centre of the vertical straight edge. Information protected under United States patent [44].

The optical design of the 2X refractive pupil slicer can be seen in fig. 4.7 and the optical parameters and locations are summarized in tables 4.2 and 4.3. The design of the slicer is protected under a United States provisional patent [44]. Lens L1 is a circularly symmetric cylindrical lens made from N-BK7 glass with a focal length of 200 mm (Thor Labs, LJ1653RM-B). Lens L2 is also a circularly symmetric cylindrical lens made from N-BK7 glass but with a focal length of 50 mm (Thor Labs, LJ1695RM-B). The two lenses are placed 246.3 mm apart so the light emerging from L2 is collimated but compressed vertically by a factor of 4. To save on space the light is reflected in a dogleg by using mirrors M1 and M2 (Thor Labs, BB1-E03).

All the spot area aspect ratio manipulation in the slicer is performed by the cylindrical lenses. However, if only cylindrical lenses are present the pupil beam profile aspect ratio will be the inverse of the spot area aspect ratio, i.e. not circular. There are several reasons why a circular pupil function is desired. First, the diffraction limited Airy pattern will be circularly symmetric. Second, if aberrations are present then they will be symmetric across the pupil. Third, it allows for the use of circularly symmetric optics. Fourth, a circular pupil is needed if multiple pupil slicers are to be used in series. Fifth, when used in a grating spectrograph the light is spread over a larger vertical area on the diffraction grating so the effects of any imperfection is minimized. Since the focused spot shape does not depend on the aperture spatial transmission function, albeit pupil aberrations and diffraction Airy patterns (according to eqn. 2.45), which can be ignored for a first order description, the pupil spatial light distribution may be oriented in any desired shape. Therefore the non-circular pupil emerging from the cylindrical lens relay may be “sliced” and reoriented to

form a circular pupil without changing the étendue. This is achievable by the use of the redirecting mirrors, M3 and M4, in a dogleg orientation. The mirrors used are a special kind of mirror called a D-mirror because they resemble the letter 'D,' in reality the mirrors are semicircles (Thor Labs, BBD1-E03). The mirrors in the slicer are placed 100 mm apart and they are tilted by 1.1° about the dispersive axis and -2.28° about the cross-dispersive axis.

After the cylindrical lenses and slicing mirrors the pupil is collimated and circular, but the diameter is a factor of 2 smaller than the input diameter. The focused spot will have an aspect ratio of 1:4 and the width will be equal to the width of the original spot because the étendue has not changed in that dimension. In order to dilute the pupil so the diameter is equal to that of the incoming beam a telescope relay may be used with circularly symmetric lenses. The lenses used are L3 and L4. Lens L3 is an achromatic doublet lens with design wavelengths of 706.5 nm, 855 nm, 1015 nm and a focal length of 50 mm (Thor Labs, AC254-050-B). The light exiting L3 is collimated again upon exiting lens L4, which is also an achromatic doublet lens with design wavelengths 706.5 nm, 855 nm, 1015 nm but with a focal length of 100 mm (Thor Labs, AC508-100-B). The two lenses are placed 139.26 mm apart from each other. This telescope relay increases the solid angle of the beam in both dimensions equally by a factor of 2 and therefore decreases the height and width of the focused spot by a factor of 2; the focused spot's width will be reduced by a factor of 2 compared to the original width, and the height will be increased by the same factor of 2.

4.4 Performance of the 2X Refractive Optical Pupil Slicer

In order to test the performance of the 2X refractive slicer it was placed in a custom-built in-house dispersive spectrograph; the following results and discussion were presented in [42]. The 2X refractive slicer was designed to be placed in a dispersive-type spectrograph with a beam diameter of 15 mm and a clear aperture diameter on the optics of 22 mm; therefore the input and output beam diameter of the slicer fit entirely within a 22 mm diameter clear aperture. The input to the spectrograph is a 50 μm core diameter fibre. The fibre light is collimated using a 50 mm focal length, 25.4 mm diameter achromatic doublet lens with design wavelengths of 706.5 nm, 855 nm, and 1015 nm (Thor Labs, AC254-050-B). The collimated light is angularly dispersed by a 300 l/mm holographic transmission grating with a blaze angle of 31.7° (Thor Labs, GTI50-03A) tilted at an incident angle of 7.5°. The dispersed light is then focused using a 100 mm focal length, 50.8 mm diameter achromatic doublet lens with design wavelengths of 706.5 nm, 855 nm, and 1015 nm (Thor Labs, AC508-100-B). The light is detected by a linear 1D array CCD camera with 3648 pixels of size 8 μm by 200 μm with a 16 bit readout (Mightex, TCE-1304-U).

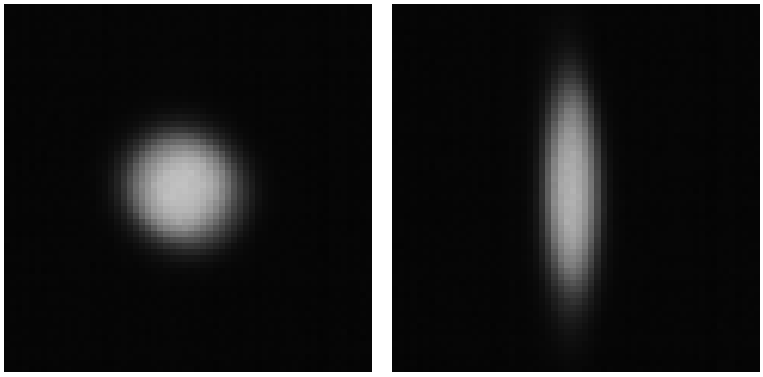

(a) Before Slicer (b) After Slicer

Figure 4.8: The images of the focused spot shape before and after passing through the slicer.

The slicer was designed to operate in the NIR band of light covering the wavelengths from 700 nm to 1000 nm. The throughput of the slicer was measured by placing narrow-band interference filters in the beam path and measuring the optical power using a power meter (Newport, 1918-C) with a calibrated silicon-based detector wand (Newport, 818-ST/DB). The filters used to measure the throughput have centre wavelengths of 700 nm, 750 nm, 800 nm, 850 nm, 900 nm, 950 nm, and 1000 nm with bandwidths of 10 nm (Thor Labs, FB700-10, FB750-10, FB800-10, FB850-10, FB900-10, FB950-10, FB1000-10). The light source used is a calibrated black-body tungsten-halogen source operating at 2,850°K (Avantes, AvaLight-HAL). A resulting plot of calculated throughput can be seen in fig. 4.9(a). The average measured throughput was found to be 85.58% over the spectral range 700 nm to 1000 nm.

The power of the slicer is defined by its reduction in spot width at a given étendue and wavelength band. The étendue for the source fibre and collimating lens is calculated to be approximately $\Xi = 298.556$ [μm^2 sr]. Images of the focused spot were captured using the same focusing lens in the spectrograph (Thor Labs, AC508-100-B) and a high-quality CMOS web-cam with 6 μm by 6 μm pixels (IDS, UI-1225LE-M-GL), these can be seen in fig. 4.8. The images were vertically binned to create the 1D focused spot profile plots, shown in fig. 4.9(b). A full-width at half-maximum (FWHM) value was measured from the resulting 1D plots in order to measure the slicer power. An average power of 2.00X in spot width reduction was measured going from a 81.6 μm to 40.8 μm over the wavelengths 700 nm to 1000 nm.

The goal of the slicer is to improve the quality factor, Q, of a dispersive-type spectrograph by increasing the resolving power, R, by reducing the spot width in the dispersive direction by a factor larger than the loss of throughput efficiency, T. The slicer is shown to

potentially improve the resolving power by a factor of 2.00 while maintaining an average throughput of 0.8556, thereby improving the quality factor of a dispersive-type spectrograph by a factor of 1.7112. The slicer was used in the spectrograph described above and spectra of calibrated atomic emission line sources were captured. These resulting spectra were compared against the spectrograph with no slicer (and no conventional slit). The light sources used were a calibrated mercury-argon emission source (Ocean Optics, HG1) and a calibrated neon emission source (Avantes, AvaLight-CAL-Neon). Both light sources have strong emission features over the spectral band 700 nm to 1000 nm. A select wavelength region for each light source and the resulting spectra both with and without the slicer are shown in figs. 4.10(a) and 4.10(b). Given the spectrograph hardware parameters and the measured spot width FWHM, the resolving power of the spectrograph without the slicer is about $R = 315$ and with the slicer it is increased to about $R = 630$.

The resulting spectra clearly show an increase in the resolving power by using the slicer. In fig. 4.10(a) a single emission line at 859.12 nm is enhanced by the slicer, and three closely separated emission lines at 863.46 nm, 865.43 nm, and 867.94 nm are unresolved without the slicer but easily resolved with the slicer, the wavelength separation values were taken from the NIST spectral database [50]. A similar observation is seen in the mercury-argon emission spectra where a single emission at 826.45 nm is enhanced by the slicer and two closely separated emission lines at 840.82 nm and 842.46 nm are unresolved without the slicer but easily resolved with the slicer. The resolving power required to resolve the mercury-argon doublet is at least $R = 513$, and since the spectrum shows a good resolution it is likely that the resolving power of the slicer spectrograph is larger ($R > 513$). The spectra from the using the slicer do not have an apparent loss in signal strength, thereby confirming the throughput advantage of using a slicer as opposed to a conventional slit—the measured average throughput for both spectra is 83.88%.

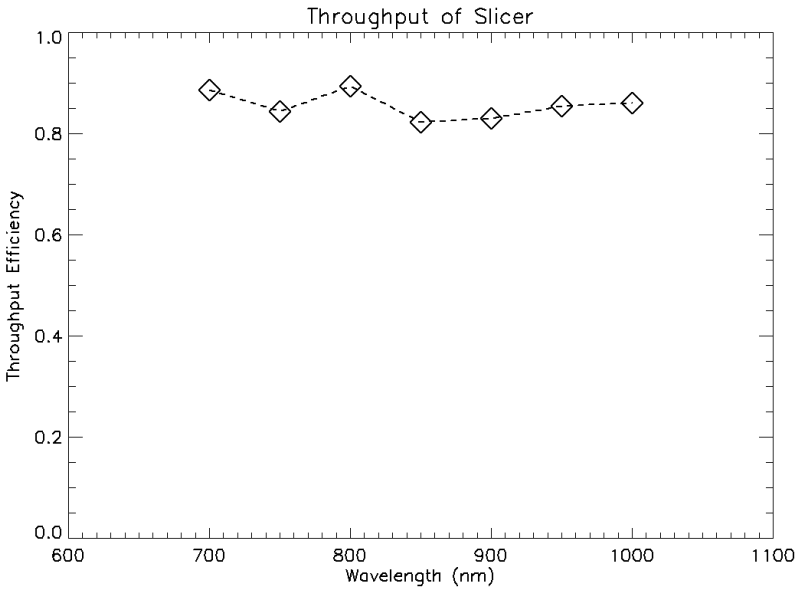

(a) Throughput Efficiency

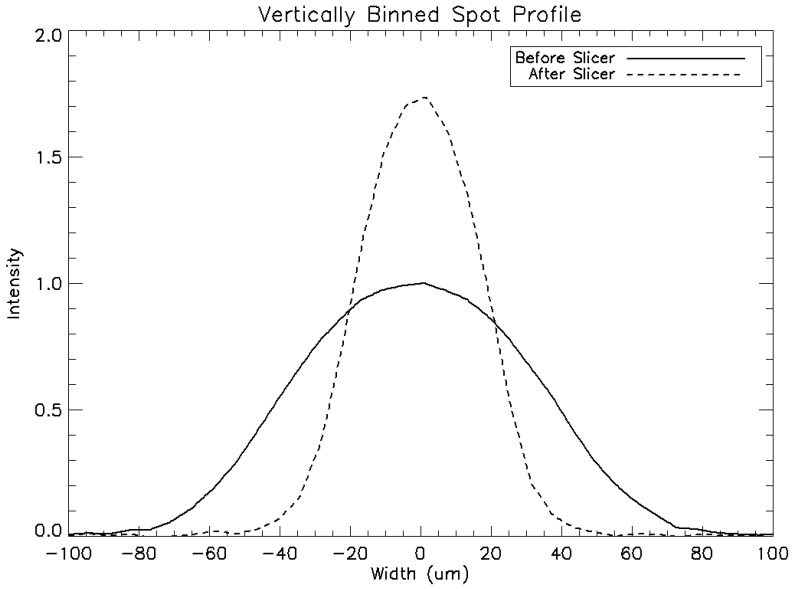

(b) Spot Profile

Figure 4.9: Plots showing the throughput efficiency of the slicer measured as a function of wavelength over the spectral band 700 nm to 1000 nm, and the focused spot before light passes through the slicer (solid) and after (dashed).

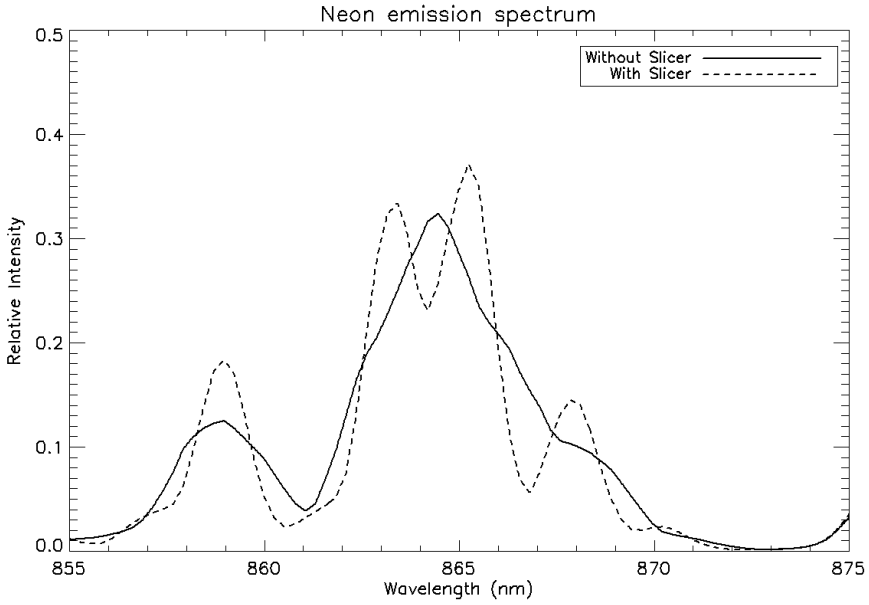

(a) Neon

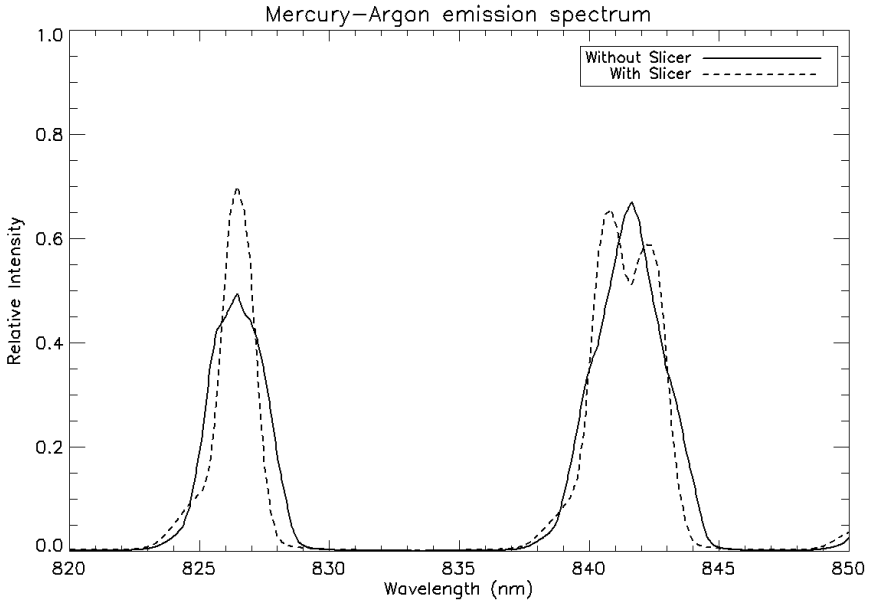

(b) Mercury-Argon

Figure 4.10: The spectra captured from the calibrated atomic line emission sources using the slicer (dashed) and without the slicer (solid).

Chapter 5

Implementing the Slicer in the SD-OCT System

In section 4.4 we saw that a refractive based optical pupil slicer designed to have a slicing factor of 2X was able to reduce the focused spot width by a factor of 2.00 from 81.6 μm to 40.8 μm from a fibre source of core diameter 50 μm and maintain 85.58% efficiency over a bandpass from 700 nm to 1000 nm. This effectively increased the resolving power, R, of the spectrograph by a factor of 2.00 and the spectrograph quality, Q, by a factor of 1.7112 (see eqn. 4.6). The quality of an SD-OCT system may be determined by the quality of the back-end spectrograph as was discussed in section 3.1.1; the resolving power plays a crucial role in the imaging depth characteristics and the throughput limits the speed-efficiency of the OCT system. Designing and implementing a custom spectrograph for the in-house SD-OCT system which includes the optical pupil slicer described in section 4.3 will be considered in this chapter. An SD-OCT system including an optical pupil slicer in its design is protected by an International patent [43]. First a justification, simulation, and analysis on optical pupil slicers in SD-OCT systems will be given. This is followed by the method of the actual implementation of the 2X refractive optical pupil slicer in the SD-OCT system and the results which follow. As will be seen, the refractive 2X slicer does not provide any improvement in the custom SD-OCT system. The analysis and evaluation on this failing result will be given and the necessary improvements to be made on both the SD-OCT system and the optical pupil slicer will be presented.

5.1 Justification for Implementing a Slicer in an SD-OCT System

The maximum obtainable unaliased imaging depth, z_{max}, in SD-OCT systems is given by eqn. 3.6, which is dependent on the pixel wavelength separation, $\Delta\lambda$, and hence the resolving power, R, of the back-end spectrograph. The signal obtained from a SD-OCT system, S_{OCT}, is given by eqn. 3.7, which is the fringe contrast (visibility) multiplied by the number of detected photons. A practical maximum imaging depth, z_{pmax}, may be defined as the point at which the signal-to-noise ratio (SNR) drops to below a chosen threshold. Ordinarily in highly scattering media this point occurs before the maximum unaliased imaging depth ($z_{pmax} < z_{max}$). Since the fringe contrast verses depth (see fig. 3.1) is dependent on the resolving power, it follows that the maximum practical imaging depth, z_{pmax}, is also dependent on the resolving power. It is a common practise in OCT, and especially in the design of SD-OCT systems, to attempt to increase the resolving power as much as possible. However, it is often not useful to increase the resolving power beyond a certain point where the improvement seen is minimal (see example fig. 4.2), nor is it practical to attempt to increase the resolving power beyond the maximum theoretical resolving power, R_{max}, given by eqn. 4.7.

As was discussed in section 4.3, a common technique for increasing the spectral resolution, and hence the resolving power, is to place a slit or pinhole at a conjugate focal point in the spectrograph; however, this technique throws away valuable light and decreases the throughput and efficiency of the spectrograph. This is not a desirable trade-off in OCT since little light is collected anyway, and this is especially true in speed-limited OCT applications like ophthalmology [12, 48]. Using a slicer-type spectrograph in an SD-OCT system makes sense because it is able to provide high spectral resolution, and therefore good imaging depth quality, without a large sacrifice in throughput, hence increasing the quality factor of the SD-OCT system.

If a perfectly efficient (100% throughput and quantum efficiency, η) spectrograph were used in an SD-OCT system that had maximized the light delivery intensity as dictated by safety regulations and collected every useful photon returning from the sample and reference arm, this represents the best possible scenario. Suppose that one then wishes to increase the resolving power by use of a slit, this now drives the throughput efficiency down by some factor and the OCT system is no longer "perfect." By using an optical pupil slicer instead of a slit the throughput may be maintained ideally at 100% but the spectral resolution will be increased and hence the SD-OCT quality factor will increase. This is a fundamental improvement to SD-OCT systems.

5.1.1 SD-OCT System and Slicer Simulation

The philosophical justification for pursuing the endeavour of implementing an optical pupil slicer in an SD-OCT system was given in section 5.1. Embedded within the argument it was claimed that slicers can make a fundamental improvement to SD-OCT because they are able to increase the resolving power of the back-end spectrograph while maintaining throughput. The resulting throughput maintenance performance of the 2X refractive slicer was shown in section 4.4; these results served as the proof that the optical pupil slicer can maintain throughput while increasing spectral resolution. In order to justify using hard numbers and quantitative, as well as qualitative, analysis a proper study of how an optical pupil slicer affects the SD-OCT signal must be carried out. Since the throughput argument has already been proved and justified, the effect of increasing the resolving power on the custom built in-house SD-OCT system described in section 3.2 remains to be evaluated. For the purposes of simulation an interpreting-type programming language called IDL (Interactive Data Language) version 7.0 was used [37].

Simulation Model and Theory

The purpose of the simulation is to generate a relative fringe contrast versus depth plot—like the one in fig. 3.1(b)—for the custom SD-OCT system both with and without a slicer. Several steps are taken to generate this plot and some assumptions are made to simplify the process. The general design philosophy of the simulation is to work backwards and then express the input in parameters controllable by the slicer and the spectrograph hardware. To understand the fringe contrast versus depth relationship first consider the signal obtained by a single pixel. The signal in the j^{th} pixel of the SD-OCT spectrograph as a function of sample reflection location, z_s, may be given by

$$\begin{aligned} I_j(z_s) &= \int_{\delta\lambda_j} \left(I_r(\lambda) + I_s(z_s,\lambda)\right) d\lambda \\ &+ \left|\psi_j\left(z_s, \delta\lambda_j\right)\right| \cos\left(4\pi\frac{z_s}{\lambda_j}\right) \cdot \int_{\delta\lambda_j} 2\sqrt{I_r(\lambda) I_s(z_s,\lambda)} d\lambda, \end{aligned} \tag{5.1}$$

which is seen to be very similar to eqn. 3.3, except in the term z_s as opposed to Δd (these differ by a factor of 2 due to physical delay as opposed to optical delay). The functions $I_r(\lambda)$ and $I_s(z_s,\lambda)$ represent the optical intensity of the reference and sample arms respectively as a function of sample reflection distance from the beam splitter device, z_s, and wavelength, λ. The function $\psi_j\left(z_s, \delta\lambda_j\right)$ is the spectral coherence function of the j^{th}

pixel. From section 3.1.1 the spectral coherence envelope for the j^{th} pixel may be expressed as the Fourier transform of the optical power spectrum in the j^{th} pixel. The optical power spectrum in a pixel may be given as the convolution of the pixel spatial response function with the image of the source object, and then further convolved with the diffraction Airy spot pattern for each wavelength in the source bandpass. Using the convolution theorem the spectral coherence envelope for the SD-OCT system can be represented as

$$\psi(z_s) = \text{FT}\left[\int \text{P}(x_i, y_i)dy_i\right] \cdot \text{FT}\left[\int I_{\text{Airy}}(x_i, y_i)dy_i\right] \cdot \text{FT}\left[\int I_{\text{Image}}(x_i, y_i)dy_i\right], \quad (5.2)$$

where the pixel spatial response function is given as $\text{P}(x_i, y_i)$, the diffraction Airy pattern produced by the camera lens is given as $I_{\text{Airy}}(x_i, y_i)$, and the image of the source object is given as $I_{\text{Image}}(x_i, y_i)$. The arguments have been given in terms of x_i and y_i, which are the 2D rectangular coordinates on the focal plane for the dispersive and cross-dispersive directions respectively. The dispersive positions on the focal plane, x_i, can be converted to wavelength, λ, by eqn. 4.3 that can furthermore be converted to sample depth as was discussed in section 3.1.1. Given the spatial pixel response function is typically a RECT function, and the two intensity profiles (I_{Airy} and I_{Image}) may be approximated by Gaussian functions, it can be seen that eqn. 5.2 is similar to the commonly accepted eqn. 3.5 for the spectral coherence envelope. It has been assumed that all pixels in the SD-OCT system spectrograph have the same bandpass functions and that the sample is a perfect grey-body reflector, therefore the entire SD-OCT system may be characterized using the spectral coherence envelope. Given some hardware input parameters such as wavelength bandpass ($\Delta\Lambda$), diffraction grating line spacing (d_g), sample material index (n), focal length of camera lens (f_{cl}), pixel width, and extended input source geometry, the fringe contrast versus depth relationship (ψ) may be completely determined.

Simulation Results

The spectrograph of the SD-OCT system described in section 3.2 may be simply modelled using the hardware parameters, as were summarized in table 3.2. The optical pupil slicer described in section 4.3 may be modelled as a black box with a given slicing factor that only affects the horizontal compression and vertical expansion of the original extended input source geometry, in this case being a perfect uniform circle. These parameters are the input to the simulation code and are summarized in table 5.1. Several plots are produced that attempt to explain the effect of including a slicer in the SD-OCT system and are shown in figs. 5.1-5.4.

Simulation Input Parameters	
Parameter	**Value**
λ_{min}	800 nm
λ_{max}	900 nm
λ_0	850 nm
Grating line spacing	1200 l/mm
Collimated beam diameter	15 mm
Camera focal length	150 mm
Collimating lens focal length	75 mm
Pixel width	10 μm
Number of pixels	2048
Pinhole diameter	10 μm
Slicing factor	2
Material index	1.0

Table 5.1: Input hardware parameters to model the spectrograph in the SD-OCT system for the simulation code to compare the fringe contrast versus depth relationship for both with and without a slicer.

Discussion

The results from the SD-OCT simulation characterize the spectrograph in terms of the imaging point spread function (PSF) and the spectral bandpass in each pixel, $\delta\lambda$, as well as how the performance of the spectrograph affects the depth imaging results of the SD-OCT system. We know from the OCT theory presented in section 3.1 that the depth signal is attenuated according to the spectral coherence envelope, which furthermore is affected by the spectral resolution, or the spectral bandwidth in each pixel. By narrowing the width of the imaging PSF the resolving power of the spectrograph is increased, and the coherence envelope falls off more slowly. Since the coherence envelope serves as the fringe contrast as a function of imaging depth, and furthermore since the OCT a-scan signal is proportional to the fringe contrast (see eqn. 3.7), better depth imaging will be observed for higher spectral resolving power.

The plots in fig. 5.1 show the normalized spatial-spectral distribution of light on the focal plane of the camera lens, which coincides with the location of the detection plane of the camera. The functions are plotted in the domain of wavelength space, which is equivalent to physical location space by eqn. 4.3. The finite extended image source in the spectrograph is the 10 μm pinhole in the spatial filter. Using eqn. 2.48 with the central wavelength, λ_0 and the focal length of the collimating lens, the diameter of the collimated beam may be found to be approximately 15 mm. Given this diameter of 15 mm and the

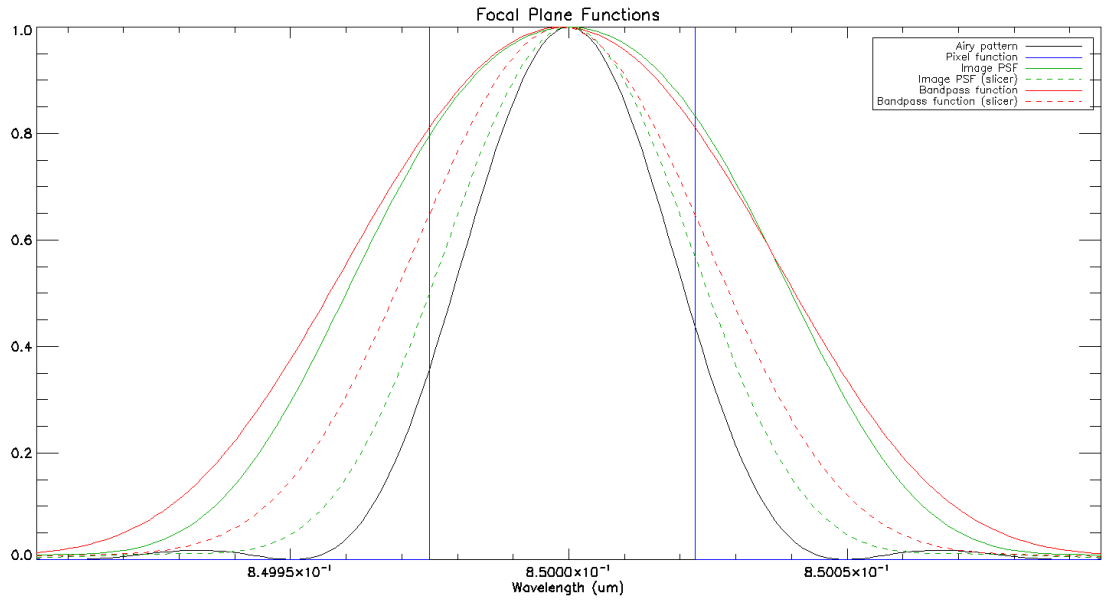

Figure 5.1: A plot showing the functions on the focal plane that are used to generate the fringe contrast versus depth relationship. The narrowest function is the vertically integrated Airy pattern (solid black) inherently produced by the camera lens. This is convolved with the vertically integrated perfect image (fig. 5.2) to produce the imaging PSF (green) for both without (solid) and with (dashed) the slicer. Furthermore the PSFs are convolved with the pixel spatial response function (blue) to produce the pixel bandpasses (red) both without (solid) and with (dashed) the slicer.

focal length of the camera lens, the Airy pattern may be computed according to eqn. 2.47. The theoretical central lobe width is equal to 20.74 μm while the pixel width is equal to 10 μm, telling us that the pixels are well below the diffraction limit.

The vertically integrated images of the pinhole are shown in fig. 5.2. The pinhole was modelled as a perfect uniform circle, but in physical reality there is some limb darkening present, this was excluded from the simulation at present for simplification. These image functions are plotted in the domain of physical extent. It is seen that the non-slicer image has an extent of 20 μm, which is exactly what we would expect from a 10 μm diameter pinhole imaged through a system with a magnification of 2. The slicer image has a physical extent of 10 μm, which is exactly what we would expect after passing through an optical pupil slicer with a slicing factor of 2X. The non-sliced image has an extent approximately the same as the diffraction limit while the sliced image has an extent approximately half the diffraction limit. These image functions are convolved with the Airy pattern to produce the imaging PSFs.

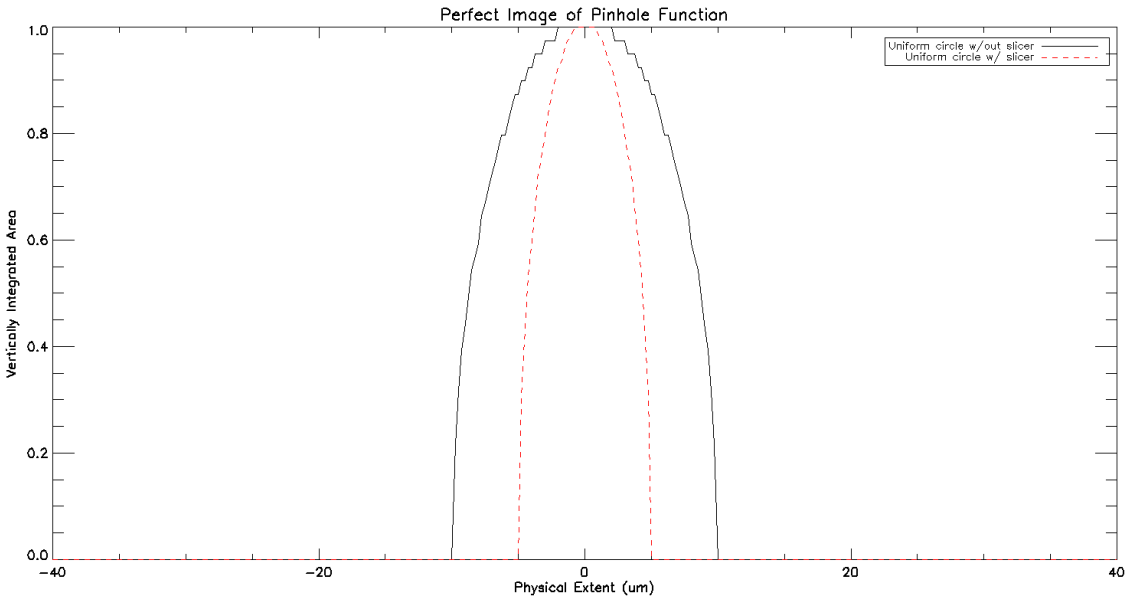

Figure 5.2: A plot showing the vertically integrated perfect image of the pinhole on the camera focal plane. The pinhole is modelled as a uniform circular function. The plot shows the results for both without (black solid) and with (red dashed) a slicer in the system. These functions are convolved with the Airy pattern depicted in fig. 5.1.

These imaging PSFs are furthermore convolved with the spatial pixel response function, in this case being a perfect RECT function. Since the pixel width is less than the width of the imaging PSFs an improvement in the pixel bandpass for slicer and non-slicer is seen. The plots in fig. 5.1 show that the bandpass functions appear Gaussian in nature, however this is not strictly true given that there are no Gaussian functions in the simulation, nevertheless the sliced bandpass has a smaller bandwidth than the non-sliced spectrum by about 73% (factor of 1.377X), reaffirming the finding that the slicer is not providing the full 50% reduction as would be ideal with a 2X slicer. In the simulation it was assumed that each pixel would have the same bandpass function so a convenient central wavelength of 850 nm was chosen. In reality each pixel will have its own bandpass function which provides a convenient way to characterize the spectrometer, however to illustrate the underlying general operation and characterization of the SD-OCT system the higher order effects of using different bandpasses for each pixel may be ignored.[1]

The Fourier transform of the bandpass for a single pixel will provide the coherence envelope and therefore determine the maximum obtainable fringe visibility as a function of optical delay, or scan depth. A high temporal coherence in a single pixel will provide a slow

[1]this was the assumption in section 3.1.1

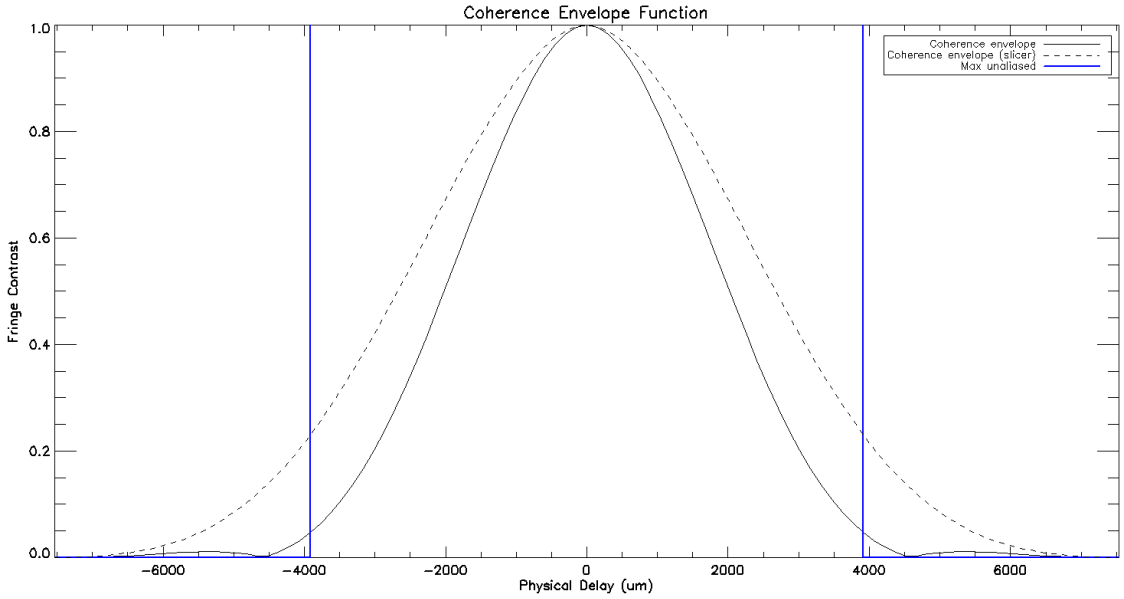

Figure 5.3: A plot showing the fringe contrast versus depth relationship for the SD-OCT system as indicated by the coherence envelope. The plot shows the results for both without (black solid) and with (black dashed) a slicer in the system. These were obtained by taking the Fourier transform of the bandpass functions depicted in fig. 5.1. Also shown is the location of the maximum unaliased imaging depth (solid bold blue).

envelope decay and therefore large signal strength over a scan depth range. High temporal coherence may be obtained by highly spatially dispersing a low temporal coherence light source.

The Fourier transforms of the bandpass functions in fig. 5.1 are taken and plotted in fig. 5.3 as a function of physical delay. The unit conversion from wavelength to physical delay was achieved through the use of appendix A. It is seen that the coherence envelope for the non-sliced system decays faster than the sliced system, as is expected, but the improvement for slicer is not profound. The ratio of the coherence envelopes is plotted in fig. 5.4. From this plot the effect of a slicer gives a 1.5X improvement in fringe contrast at around 2.1 mm, a 2X improvement at around 2.7 mm, and at most a 5X improvement at the theoretical maximum unaliased imaging depth of 3.7 mm. Keep in mind is this all for physical delay in vacuum, in a typical tissue with an index of 1.4 these distances become 1.5 mm, 1.9 mm, and 2.7 mm.

From the results presented in this section and the above discussion of said results, an argument can me made to justify the inclusion of a 2X slicer in the SD-OCT system spectrograph. First of all the fringe contrast improvement is quite significant at the largest

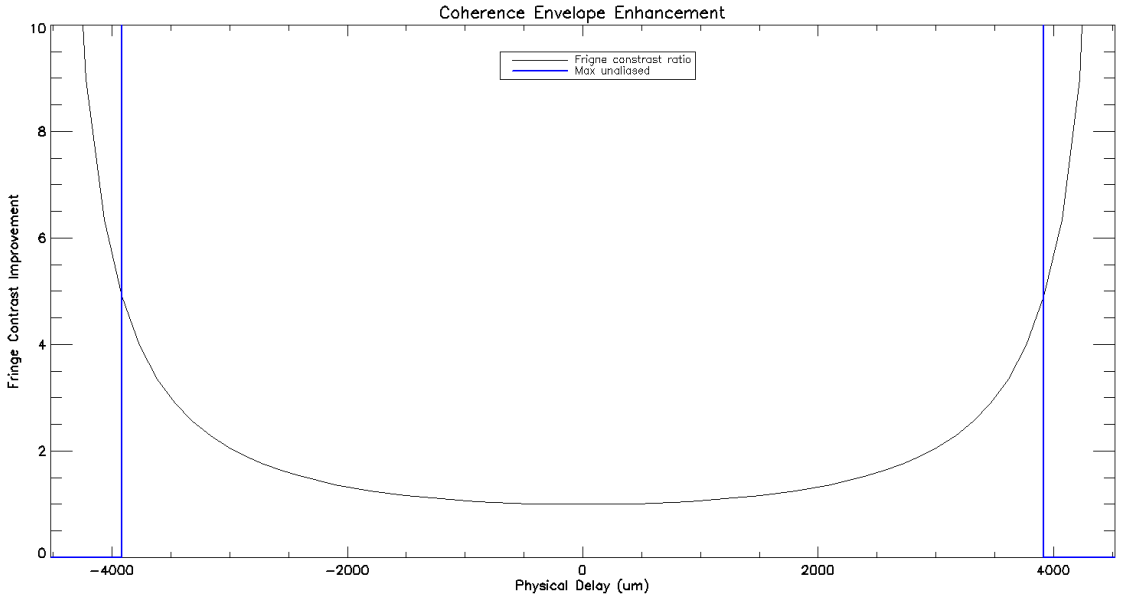

Figure 5.4: A plot showing the ratio of the fringe contrast versus depth relationship for the SD-OCT system with and without the slicer (black solid). Also shown is the location of the unaliased imaging depth.

imaging depths and no worse than the system without a slicer at all imaging depths. The most significant justification, however, is due to the fact that the slicer is able to achieve these results with virtually no loss in light, thereby increasing the practical imaging depth by increasing the SNR relative to a system that would try to achieve the same improvement in resolving power by use of a slit or additional pinhole. In other words, the slicer acts as a virtual slit providing a fundamental improvement to the quality of the spectrograph, and therefore improving the quality of the SD-OCT system.

5.2 Results From the SD-OCT System With and Without the Slicer

The 2X refractive slicer was constructed and tested separately from the SD-OCT system using a custom built spectrograph with calibrated light sources. The performance and results of the slicer were presented in section 4.4. To summarize, the 2X refractive slicer had a 85.58% throughput over a 700 nm to 1000 nm bandpass and was able to achieve a slicing factor of 2.00. This was done by slicing an image of a 50 μm fibre core. The next step was to rebuild the 2X refractive slicer in the SD-OCT system spectrograph and

perform a calibration experiment to measure the fringe visibility versus depth relationship, i.e. the spectral coherence envelope, ψ. The expected results should match the theoretical predictions presented in section 5.1.1. The actual results showed that the SD-OCT system without the slicer performed worse than expected and that the SD-OCT system with the slicer performed even worse than without. A more accurate model and simulation of the SD-OCT system was conducted in order to match and explain the measured data. A more rigorous analysis is able to explain the degraded performance of the SD-OCT system and does indeed show that the implementation of the 2X refractive optical pupil slicer further degrades the performance beyond the non-slicer system.

5.2.1 Physical Implementation

According to the SD-OCT system design depicted in fig. 3.2 the slicer was implemented after the collimating lens and before the diffraction grating in the spectrograph. A diagram of the actual implementation of the slicer in the spectrograph is shown in fig. 5.5. It can be observed that a fold mirror (M1) is located before the entrance into the slicer in order to direct the light towards the diffraction grating. If the fold mirror is removed the light follows through the slicer and then is directed towards the diffraction grating in the same manner as before. The reason for this design is so the system is able to switch quickly and easily between non-slicer mode and slicer mode by either including or removing the fold mirror. The physical space was limited so different parts of the slicer (beam compressor, reformatting mirrors, and beam expander) were placed in different sections and the light was directed by fold mirrors. The additional loss of throughput due to the folding mirrors is acceptable considering this is not a fundamental loss in the slicer design and the physical implementation is non-ideal.

Method of Construction

For the following discussion on the method of construction of the refractive slicer refer to fig. 5.5. A kinematic fold mirror (SFM1) was used to direct the light into the slicer. The kinematic control at this point was necessary to correct for any tip and tilt in the collimated beam induced by imperfect lateral positioning of the spectrograph collimating lens. The beam was reflected off of SFM1 and allowed to propagate unaffected by about 3 metres. The mirror was rotated about the x and y axis using the kinematic control so that the reflected beam was parallel to the optical table and formed a 90° angle with the input beam before SFM1.

The beam compressor was constructed in the beam path following fold mirror SFM1. The collimation, tip, and tilt of the output from the beam compressor was checked in a similar manner as before by allowing the beam to propagate unaffected by about 3

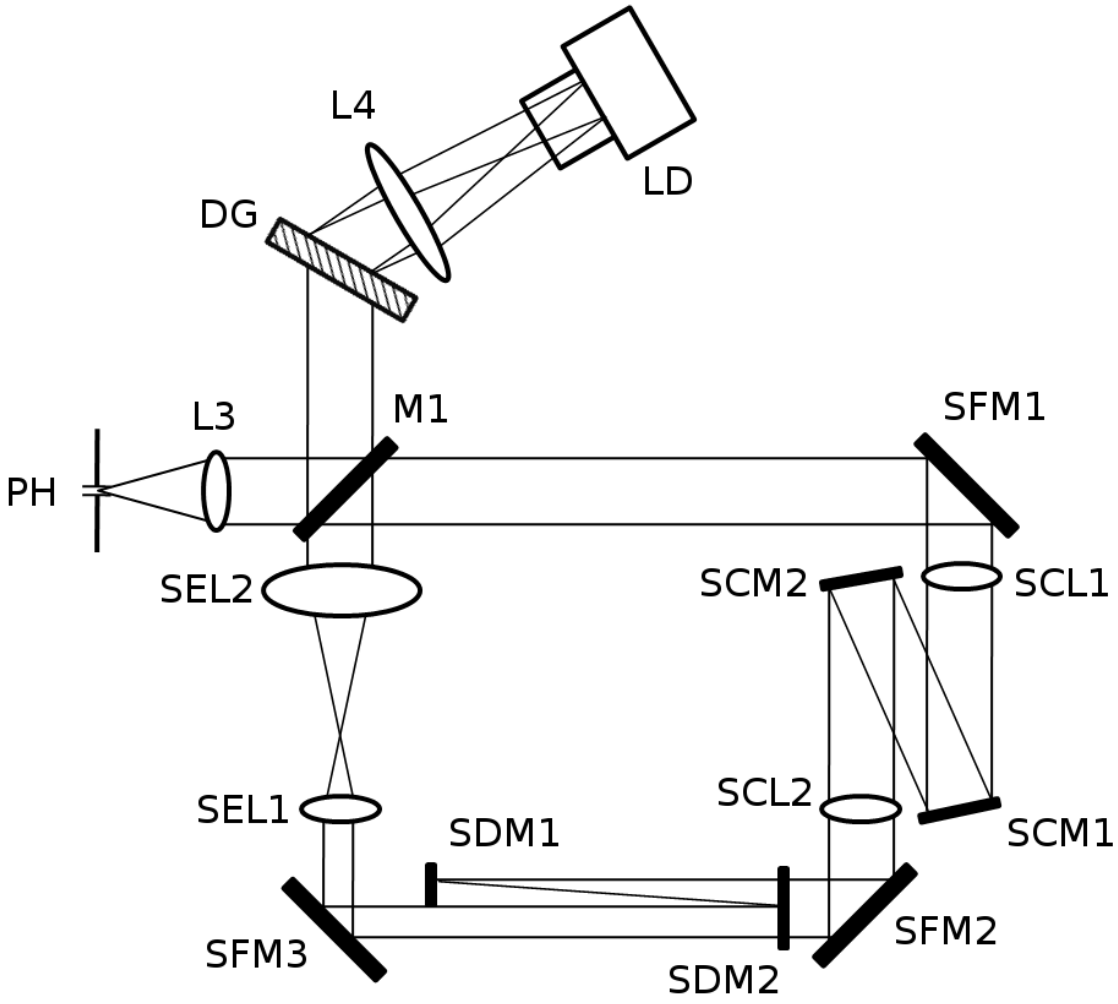

Figure 5.5: A cartoon drawing of the physical implementation of the refractive 2X slicer in the SD-OCT system spectrograph.

metres. The collimation was adjusted by changing the longitudinal location of the second compressor lens (SCL2), and the tip-tilt was corrected by rotating the first compressor fold mirror (SCM1) about the x and y axis using the kinematic control. These adjustments are not independent so an iterative approach was taken, e.g. by adjusting the tip-tilt the collimation was slightly affected.

The light exiting the beam compressor was directed to the reformatting mirrors by another fold mirror (SFM2). This mirror has kinematic control to ensure the reflected beam maintains no tip or tilt through the reformatting section. The kinematic control, however, is not strictly necessary since the reformatting mirrors are also kinematic and can compensate for any small amount of tip or tilt in the beam. For this reason the kinematic control on SMF2 is dubbed optional but preferred.

To align the reformatting mirror section of the slicer the first reformatting mirror (SDM1) is placed in the beam path such that the through beam has half the width. Next, the second reformatting mirror (SDM2) is placed some prescribed distance in front of SDM2. The height is adjusted such that the full through beam just barely passes by it unaffected. The lateral position of SDM2 is adjusted so that the reflected beam from SDM1 lands entirely in the clear aperture region of the mirror. The reformatting mirrors are rotated about their x and y axis such that the reflected beam has the same tip and tilt as the through beam. This is ensured by allowing the beams to propagate unaffected a long distance down the optical table (about 2 metres).

The reformatted pupil is directed towards the beam expander section of the slicer by use of another kinematic fold mirror (SFM3). This fold mirror needs to be kinematic to ensure the beam entering the expander is parallel to the optical table and forms a 90° relative to the input before SFM3. Also the beam needs to have slight shear control to ensure the slicer pupil is coincident with the non-sliced pupil entering the diffraction grating. The beam reflected off of SMF3 was allowed to propagate semi-unaffected by about 2 metres and the mirror was rotated about the x and y axis to eliminate any tip and tilt in the beam. The reason for semi-unaffected is because the beam passes through the grating and the zero order (m=0) is translated by a fixed amount,

$$\Delta x_p = d \cdot n \sin(\theta_i), \tag{5.3}$$

where Δx_p is the translation amount in the x direction, d is the physical thickness of the diffraction grating, n is the index of refraction of the grating, and θ_i is the incident angle. Once the reflected beam was aligned and had no tip or tilt associated with it the beam expander was placed in the path to expand the pupil diameter by a factor of 2. The output from the beam expander is the final output of the slicer and is directed towards the diffraction grating in a coincident manner with the non-sliced beam to ensure equal spatial placement on the detector.

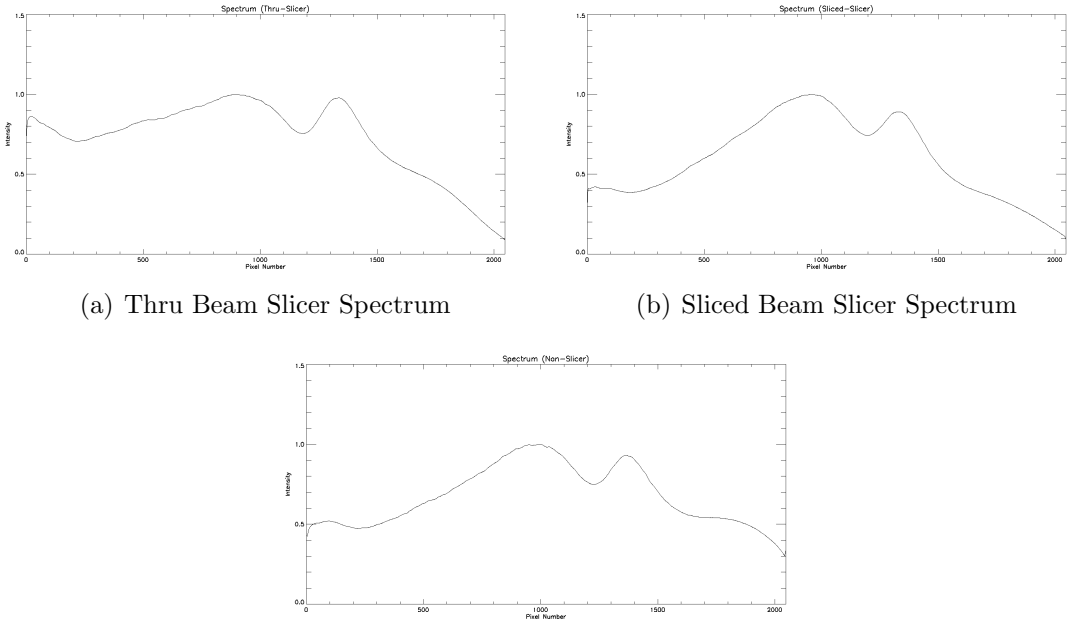

(a) Thru Beam Slicer Spectrum

(b) Sliced Beam Slicer Spectrum

(c) Non-Slicer Spectrum

Figure 5.6: The spectra for the slicer and non-slicer reference arm. The through beam from the slicer is shown in (a), the sliced beam from the slicer is shown in (b), and the non-sliced spectrum is shown in (c).

Method of Alignment

The rough bulk alignment procedure of the slicer was mentioned above. The first step of slicer alignment is to ensure the unformatted through beam is collimated upon exiting the beam expander and focuses down onto the camera to produce the same spectrum as the non-sliced beam albeit with a loss in throughput and increase in spectral resolution. The second step of slicer alignment is to ensure that the reformatted sliced beam is collimated upon exiting the beam expander and focuses down onto the camera to produce the same spectrum as the through beam. These first two steps are done independently at first by blocking the other half of the pupil (through beam or sliced beam). The third step in slicer alignment is to ensure that both spectra from the through beam and sliced beam are indeed on top of one another at the same time.

The through beam did not produce the exact same spectrum as the non-sliced beam. The two spectra can be seen in figs. 5.6(c) and 5.6(a). One of the largest most obvious differences is the overall spectral shape. The through-beam spectrum appears to be much flatter than the non-sliced spectrum and have additional attenuation at the longer wavelengths. This may be due to many additional reflections and transmission losses through

the optical elements that compose the refractive slicer. It is hard to comment on any differences the spectral resolution may induce since we are examining a broadband spectrum with no high resolution features such as narrow emission or absorption lines, however, both spectra seem to have the same resolution. The location of the wavelengths is also not identical between the two spectra. This can be explained physically as not having the exact same incident angle into the diffraction grating, and can be explained practically by noting a fold mirror must go in and out to capture the two different spectra. It is a challenging task to ensure the exact same angle is achieved every time the fold mirror is removed and placed back in the system and inevitably sub-pixel and small pixel number shifts will be seen. This mismatch, however, has a very minor effect on the system performance and may be calibrated out.

The rough alignment of the sliced beam onto the camera was performed through the kinematic control of the reformatting mirrors, most notably the control of SDM2 (see fig. 5.5). The sliced beam spectrum can be seen in fig. 5.6(b). It is observed that this spectrum has slightly lower intensity on the blue end than the through beam spectrum for several reasons. First of all the sliced beam is reflected off of two additional mirrors that each have a specific reflection spectra that will affect the overall spectrum of the sliced beam. Second of all the sliced beam has a different pupil shape and is passing through different locations of the optical components which all contribute minor effects to the overall spectrum.

The most important aspect of aligning the slicer is to ensure the two spectra from both the through beam and the sliced beam fall on top of one another. This means that any single wavelength in both spectra share the same spatial location and this holds for all wavelengths. In first evaluating the performance of the 2X refractive slicer, calibrated high resolution line light sources were used (see section 4.4) which made aligning the two beams relatively easy. In the case of the SD-OCT system the convenience of line sources was not available for several reasons. At first and attempt was made to couple the spectral line sources into the SLD single mode fibre by use of a 1:1 imaging relay system. The output from the light source is a multi-mode fibre so the coupling efficiency was extremely low. Upon propagating through the interferometer and exiting the pinhole, only slightly less than 1 nW of power made it through. This corresponds to at best 4.28×10^9 photons/s. Given the dispersive nature of the spectrometer, the quantum efficiency of the detector (37%), and the efficiency of the grating (90%), this corresponds to at best $695,750$ electrons/s/pixel. The maximum integration time of the camera is 1 ms so this gives us at most 696 electrons/pixel. Given the geometry of the pixels on the camera, only half the light from the sliced spectrograph was captured, so only one quarter of this value was ideally seen for both the through beam and the sliced beam. The read noise of the camera is quoted to be 14 electrons and the photon noise is about 14 electrons (see eqn. 2.69) giving an ideal noise floor at 28 electrons, in reality there are other noise sources

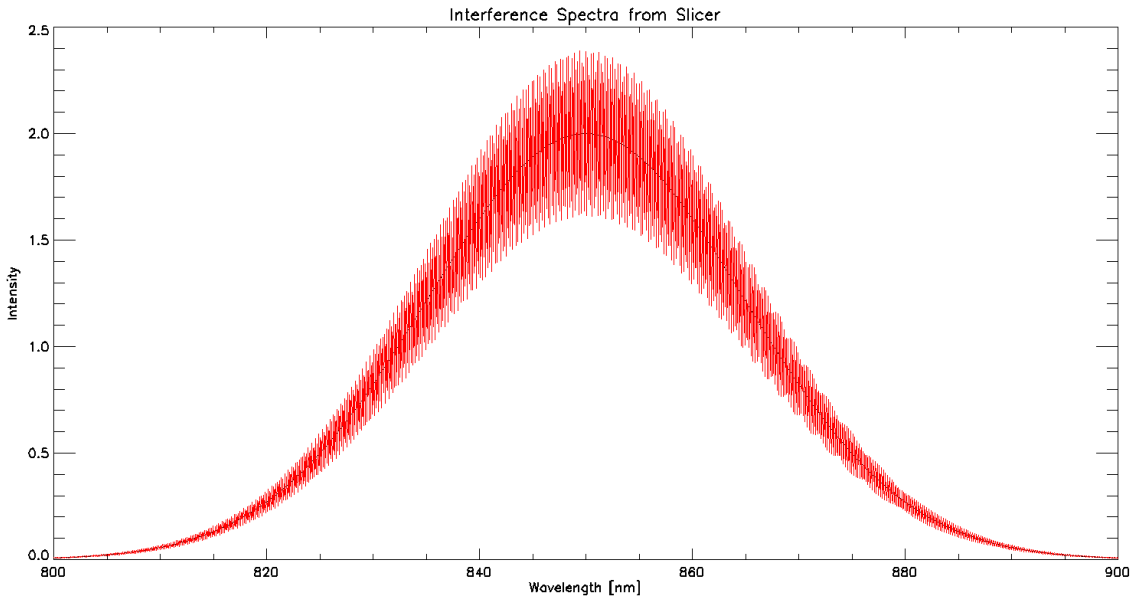

Figure 5.7: The interference spectrum produced from an aligned slicer. The delay introduced is equal to 2 mm. This data is synthetically generated.

so this is a lower bound. This corresponds to a maximum SNR of about 6 in the ideal case. In practise the SNR was observed to be closer to 1 or 2, a value far too small to perform effective fine alignment of the sliced spectrograph using the line source in this method.

A new method of aligning the two spectra from the slicer was devised using the interfered broadband spectrum from the SLD. First the sample and reference arm were allowed to interfere in order to generate chromatic spectral fringes in the spectra. A small delay was introduced in the reference arm in order to observe a few fringes across the bandpass, e.g. 5 to 10. Both spectra from the through beam and sliced beam were incident on the detector at the same time. The sliced beam was adjusted so the fringe peaks lined up with the peaks of the through beam. Next, the delay in the reference arm was increased to produce more fringes across the bandpass. Consequently the fringes were narrower allowing a finer alignment of the sliced beam. This process was continued until the combined spectra were aligned to one another at the highest resolvable fringe frequency. At large fringe frequencies (large delay) if the sliced beam was slightly misaligned a beating pattern was observed in the combined spectra, so it became relatively straightforward to keep the sliced beam aligned. This process is pictorially represented in figs. 5.7 and 5.8, and an example interference spectrum of the aligned slicer is shown in fig. 5.9.

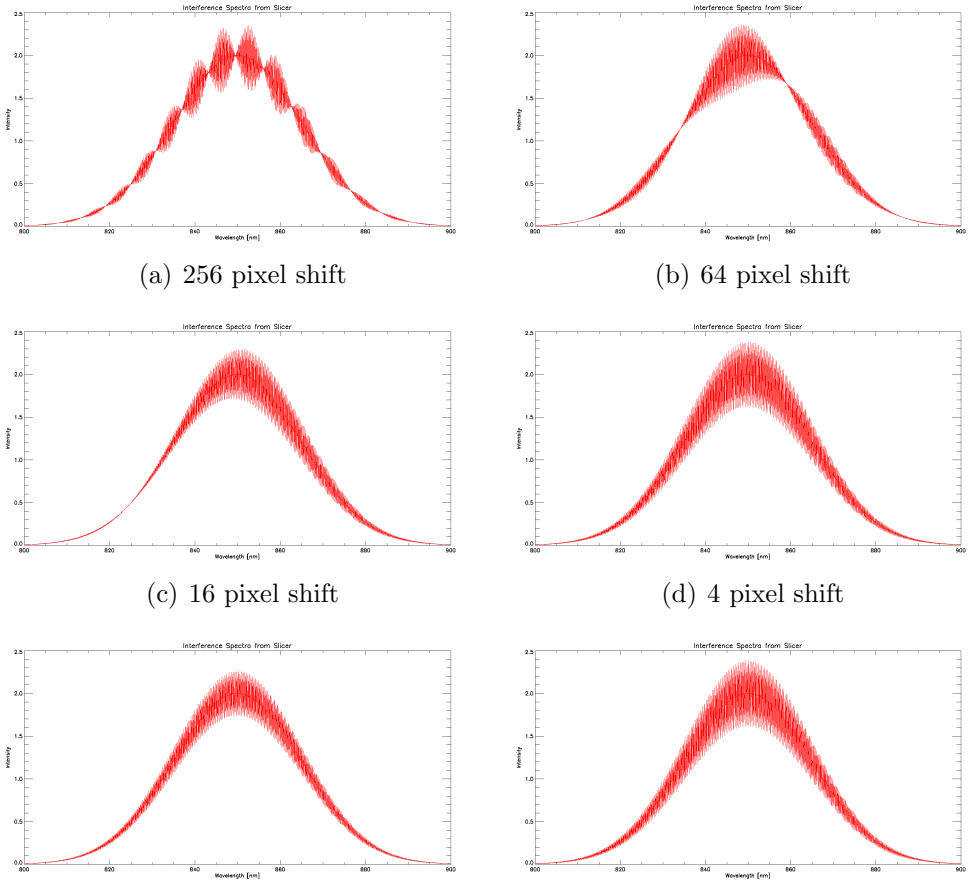

(a) 256 pixel shift

(b) 64 pixel shift

(c) 16 pixel shift

(d) 4 pixel shift

(e) 1 pixel shift

(f) 0.1 pixel shift

Figure 5.8: Plots of the interference spectra collected from a misaligned slicer. The delay introduced is equal to 2 mm. This data is synthetically generated.

5.2.2 Measurement of the Coherence Envelope

In order to measure the coherence envelope of the SD-OCT system simply the interference spectrum as a function of delay needs to be measured. This is readily achieved by placing a flat mirror at the focal point in the sample arm and recording an a-scan for various delay positions induced in the reference arm. As the path length difference between the reference arm and sample arm is increased in magnitude the spectral chromatic fringes will increase in spatial frequency and also decrease in visibility. With proper signal-image processing the spectrum may be converted in a Fourier-like manner to produce an a-scan that is composed of a single spike corresponding to delay position with an intensity proportional to the fringe contrast. This concept is illustrated in fig. 3.1.

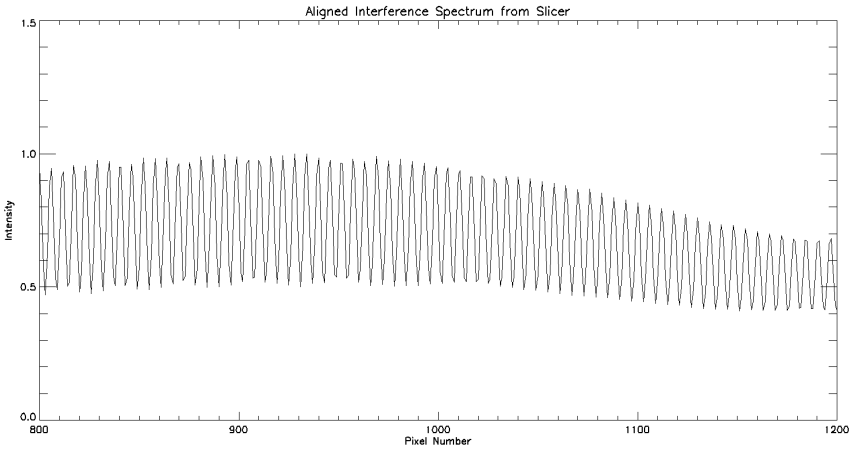

Figure 5.9: A subsection of the interference spectrum passing through the properly aligned slicer. Detector pixels 800 to 1200 were used corresponding to wavelengths 840 nm to 860 nm.

To induce different delay positions in the reference arm with reasonable accuracy and repeatability (50 nm) in a timely fashion, the retro-reflector was placed on the computer controlled sample scanning translation stage (Nanomotion, FB050). The system computer commanded the stage to move a predefined amount a certain number of times, and at each delay position a number of spectra were recorded, that of which the a-scan could be produced.

The a-scan was produced by reducing the recorded spectrum in a more specialized manner than was typically done to produce the OCT image in fig. 3.6(b). Roughly, the procedure was to subtract both the reference arm and sample arm spectra, and then divide by the geometrical average (square root) of the two spectra. Afterwards the spectra was re-sampled to linearize it in wavenumber space as opposed to wavelength space. A Fourier transform was taken and a custom dispersion correction was performed. The custom dispersion correction routine found the best distance parameter in order to maximize the peak in the a-scan. For more on numerical dispersion correction see [23, 60].

Non-Slicer Coherence Envelope

The non-slicer coherence envelope was collected by scanning through a physical delay range of ± 4 mm at 10 μm steps thus producing 800 unique delay positions. At each delay position 1024 spectra were collected which were then averaged together in post-processing to obtain a spectrum with a better SNR by a factor of 32 compared to a singly collected spectrum. A neutral density filter with an optical density of 4.0 at 633 nm (Thor Labs, NE240B) was

placed after the collimating lens in the interferometer to prevent saturation on the detector. The camera was set to have an exposure time of 6.5 μs that caused the peak central fringe signal to be slightly less than the saturation value. A few example interference spectra can be seen in fig. 5.10(a). The processed spectra after subtracting the reference and sample spectra and dividing by the geometrical mean can be seen in fig. 5.10(b).

The data was further processed by re-sampling, taking the Fourier transform, and then applying a custom dispersion correction to each delay position. Only the spectral pixels 800 to 1200 were used in this computation. The peak a-scan value for each delay position was used to generate the plot of the coherence envelope for the non-sliced spectrograph. The resulting plot was smoothed using a 10-point averaging kernel. Afterwards a Gaussian fit routine in IDL was performed to estimate an analytical function describing the coherence envelope. The resulting measured coherence envelope and the Gaussian fit are shown in fig. 5.12(a).

Slicer Coherence Envelope

The slicer coherence envelope was collected in a similar manner to the non-slicer coherence envelope, except only the through beam was used. The scanning physical delay range was $\pm$4 mm with 10 μm steps and 1024 spectra were collected at every delay position. The exposure time was set to 24 μs which resulted in a similar spectral signal strength as the non-sliced case. It is noted that the exposure time is roughly 4 times longer than the non-sliced case, as would be expected from one quarter the amount of light, which is indeed what is expected from the through beam only. A few example interference spectra can be seen in fig. 5.11(a). The processed spectra after subtracting the reference and sample spectra and dividing by the geometrical mean can be seen in fig. 5.11(b).

The sliced data was further processed by re-sampling, taking the Fourier transform, and then applying a custom dispersion correction to each delay position. Only the spectral pixels 800 to 1200 were used in this computation. The peak a-scan value for each delay position was used to generate the plot of the coherence envelope function for the sliced spectrograph. Afterwards a Gaussian fit routine in IDL was performed to estimate an analytical function describing the coherence envelope. The resulting measured coherence envelope and the Gaussian fit are shown in fig. 5.12(b).

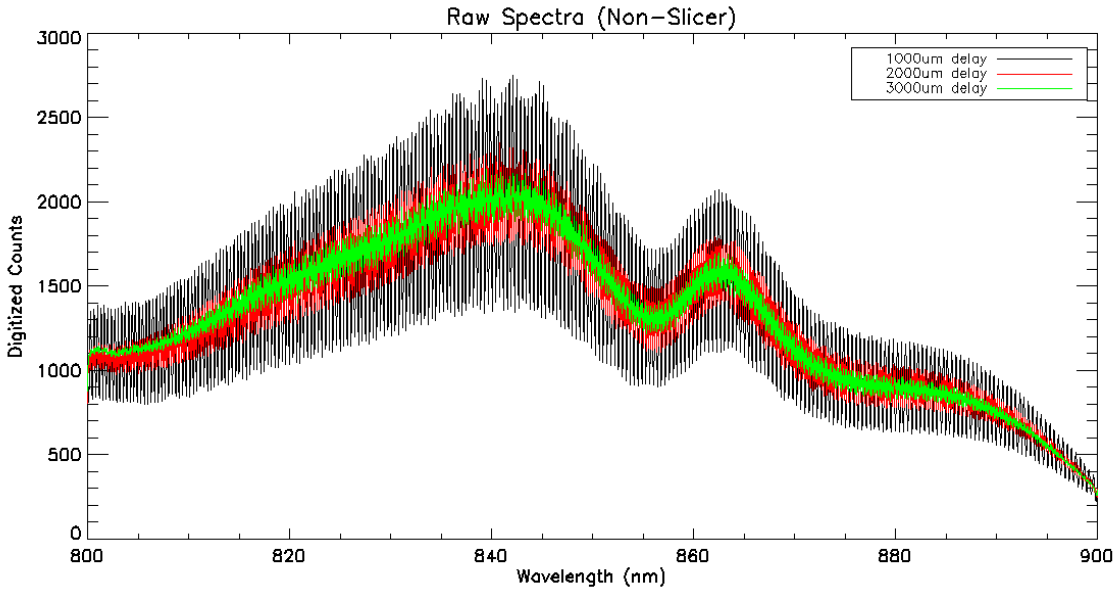

(a) Raw Spectra

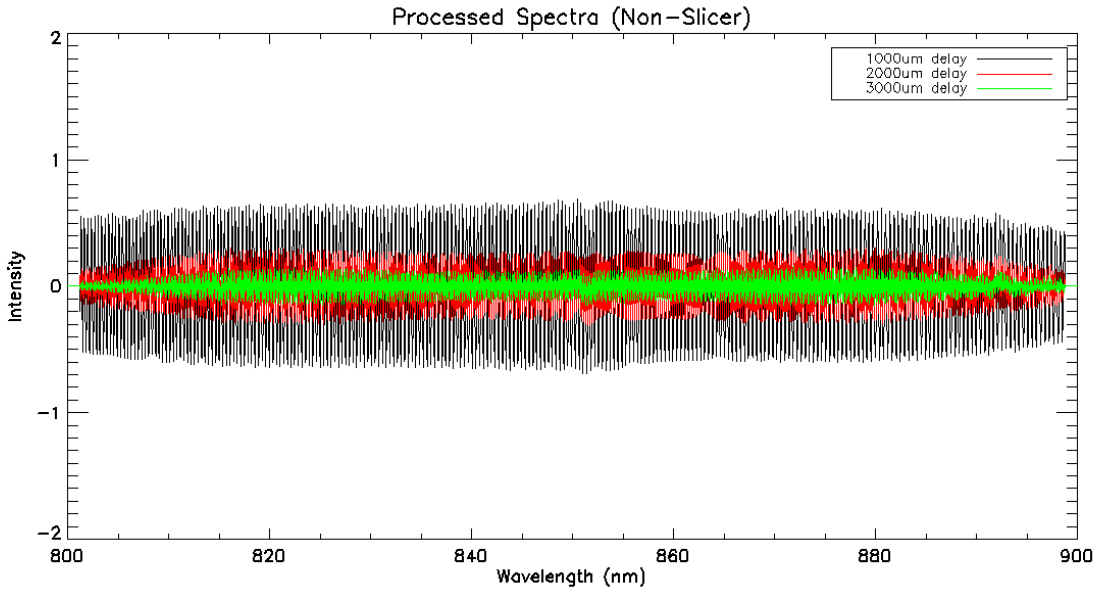

(b) Processed Spectra

Figure 5.10: The raw spectra from 3 delay positions (a) and the processed spectra (b). This is for the non-sliced spectrograph.

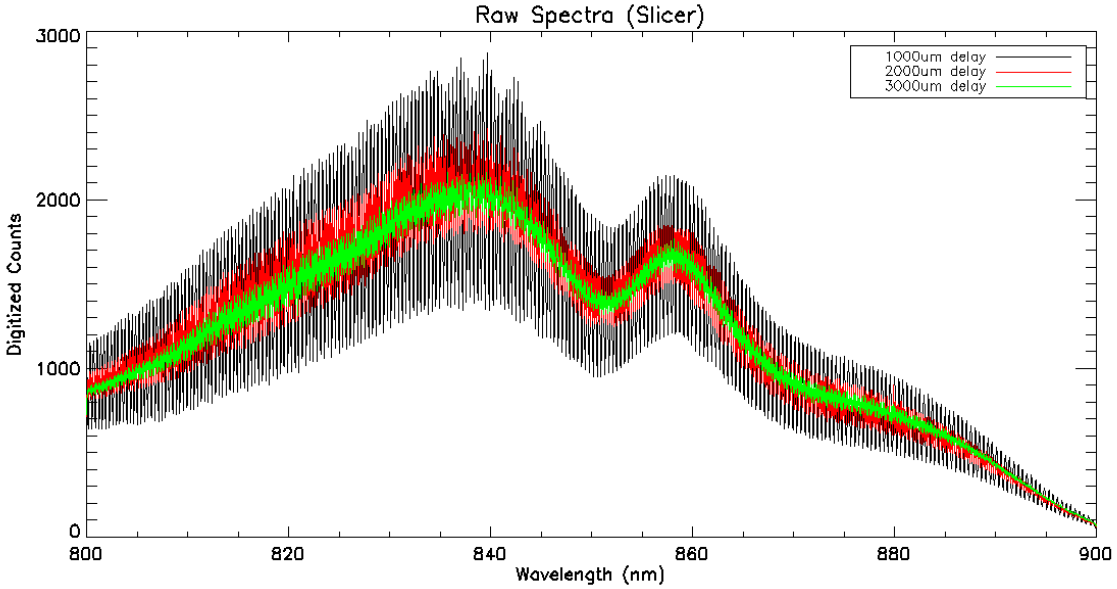

(a) Raw Spectra

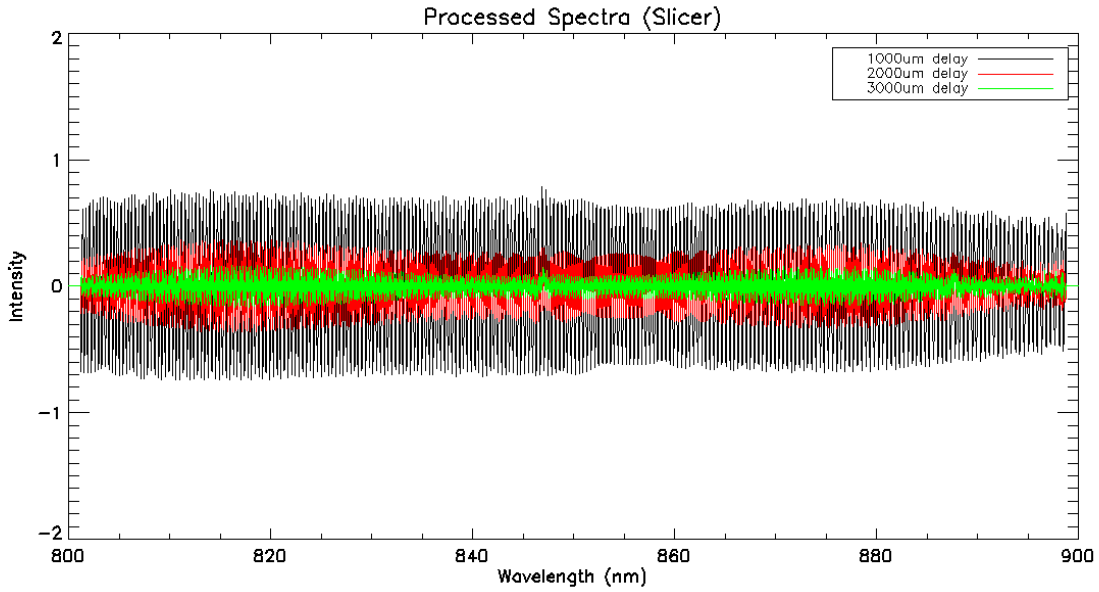

(b) Processed Spectra

Figure 5.11: The raw spectra from 3 delay positions (a) and the processed spectra (b). This is for the sliced spectrograph.

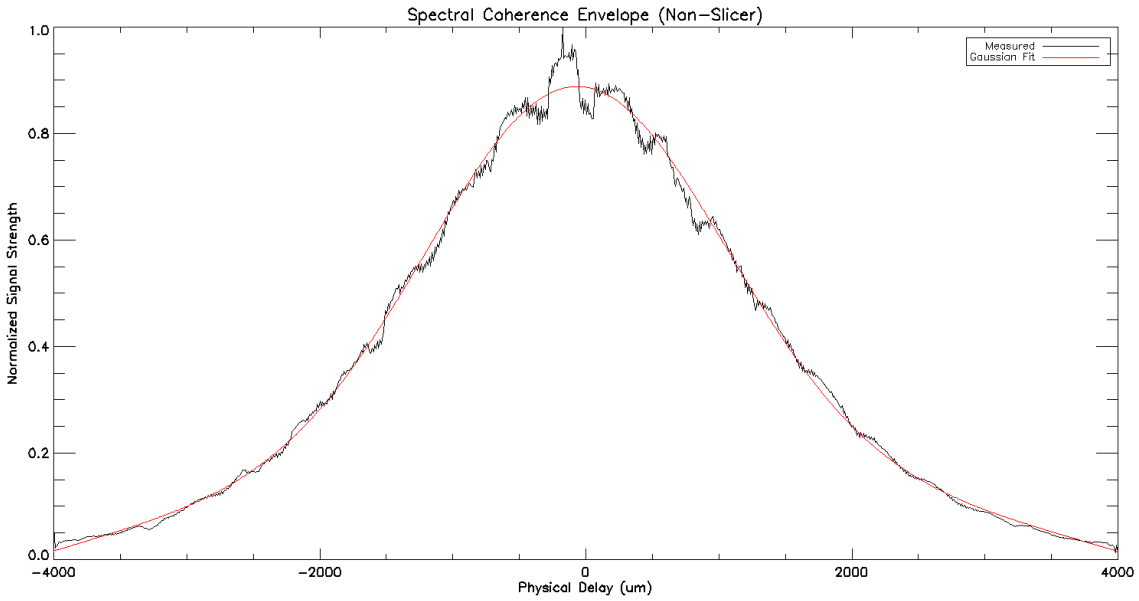

(a) Non-slicer

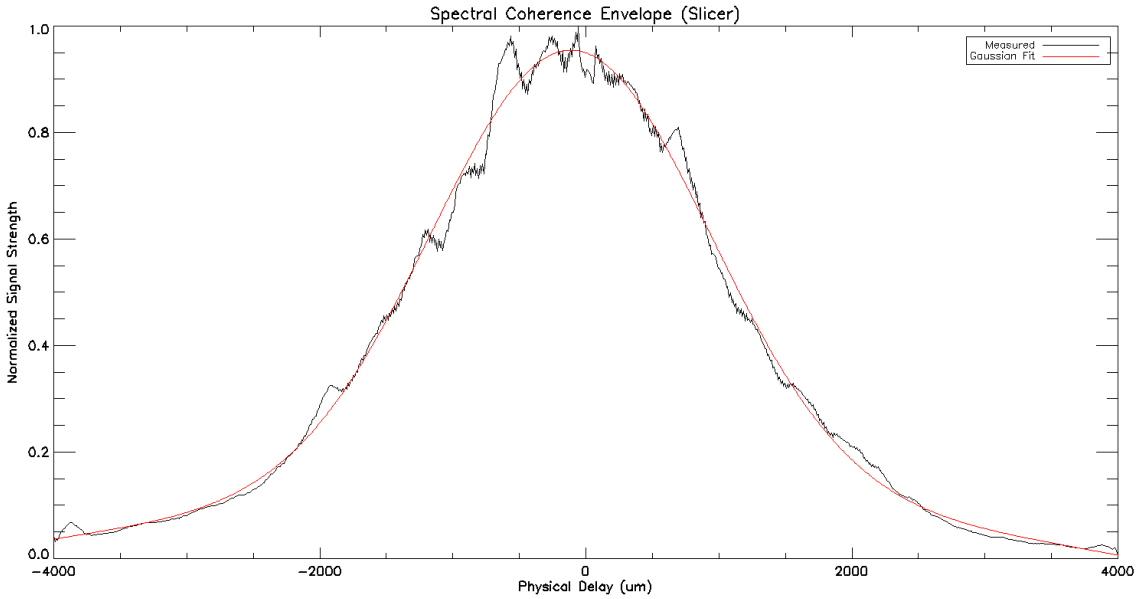

(b) Slicer

Figure 5.12: The spectral coherence envelopes as a function of physical delay. The plots were generated by converting the processed spectra into a-scans and optimizing for peak signal. Over plotted are the Gaussian fits.

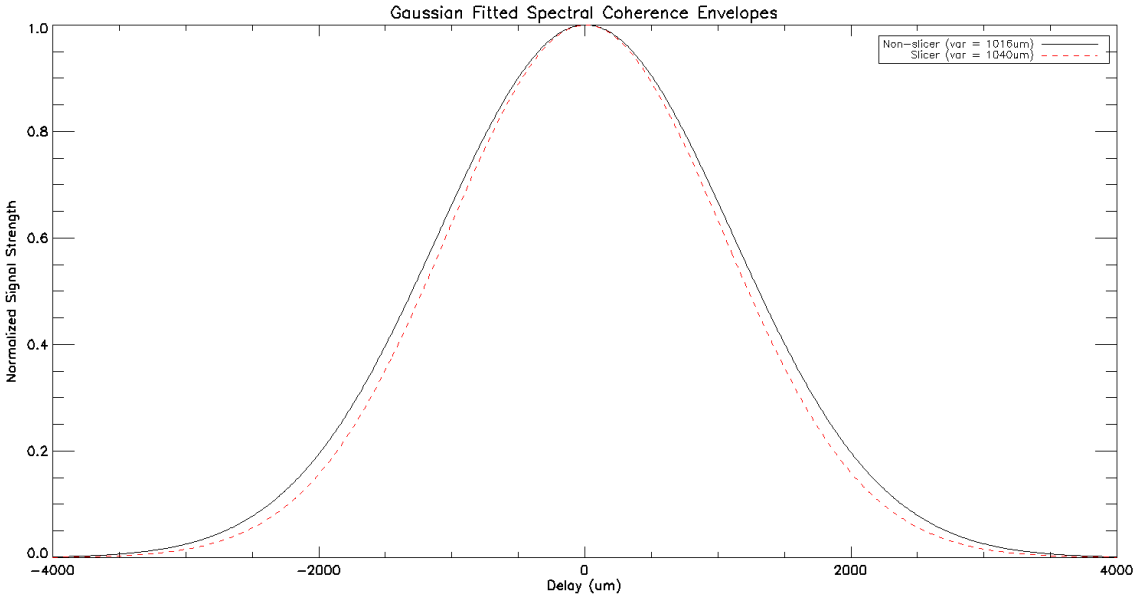

(a) Fitted Gaussian Coherence Envelopes

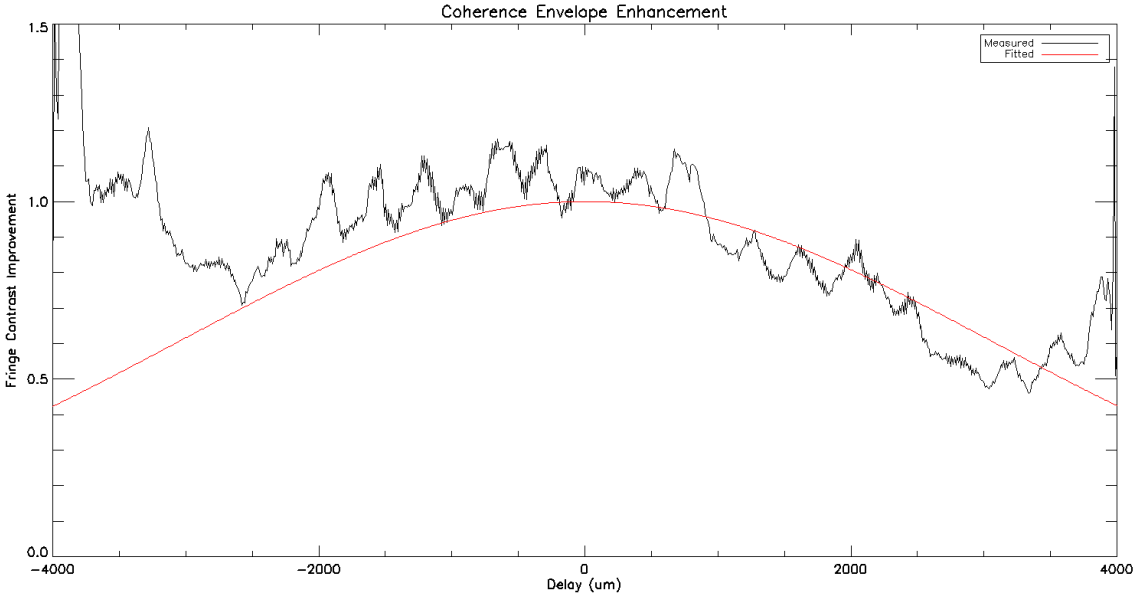

(b) Relative Fringe Contrast Ratio

Figure 5.13: (a) The non-sliced envelope is shown as solid black and the sliced envelope is shown as dashed red. (b) Ratio of Gaussians along with the ratio of the actual data from figs. 5.12(a) and 5.12(b).

Discussion

It is observed that the best fringe visibility for the non-sliced spectra in figs 5.10(b) is in the centre of the detector with pixel numbers 800 to 1200; this region corresponds to approximately 840 nm to 860 nm in the spectrum. This is a critical observation in the SD-OCT system spectrograph and implies that the focused spot size outside this region is larger than expected. The fringe visibility is expected to decrease slightly at shorter wavelengths as compared to the longer wavelengths since the shorter wavelength pixels have a more rapidly decaying spectral coherence envelope. In section 3.1.1 it was assumed each pixel behaves the same, however this is not strictly true in the SD-OCT system used so a restricted spectral window is chosen for evaluation so the higher order effects are minimized. Since the spectral coherence envelope does not depend on the wavelength region chosen insofar as much as several fringes can be observed, this restriction is valid.

The comparison between the non-sliced and sliced spectrograph results is the most important aspect of these data sets. The theoretical prediction states that the sliced spot size should be reduced by a factor of 1.377X compared to the non-sliced spot, that results in a slower decay of the spectral coherence envelope and therefore provides an improvement in the fringe visibility as a function of depth. These predictions are summarized in section 5.1.1. Even though the spectral coherence envelope may not strictly be Gaussian, it is extremely close and the fitting does an excellent job as shown in figs. 5.12(a) and 5.12(b). Also, current literature accepts the Gaussian approximation to the spectral coherence envelope, as was shown in eqn. 3.5 of section 3.1.1. The Gaussian functions have the advantage of providing us with a closed form analytical solution for the spectral coherence envelope. Plotting the Gaussian fits on the same plot will give us a similar comparison to the theoretical predictions, this plot can be seen in fig. 5.13(a).

It is observed that the Gaussian fit for the sliced spectrograph has a smaller variance (narrower function) than the non-sliced spectrograph. This is in fact opposite of what is theoretically predicted and indicates that the SD-OCT system performs worse with a sliced spectrograph than without one. Furthermore, if we compare the measured results after curve fitting (fig. 5.13(a)) to the theoretical predictions shown in fig. 5.3 we note that they do not agree. The non-sliced spectrograph seems to be performing worse than expected, but this is not a huge surprise considering the simulation was highly idealized. A plot of the measured relative fringe contrast improvement is shown in fig. 5.13(b) that was computed by taking the point-by-point ratio of the slice to non-slice data; also included in this comparison is the ratio of the two Gaussian fitted curves. This result can be compared to the theoretical prediction shown in fig. 5.4. It is observed that the ratio decreases as physical delay is increased, which again emphasizes the point that the SD-OCT system behaves worse with a sliced spectrograph than without one.

The reason why the data for the slicer was collected for the through beam only and

not both beams combined, as would be the normal mode of operation, is because the sliced beam, for all intensive purposes, is identical to the through beam and only offers a throughput advantage. The effect of spectral resolution increase is inherent in both beams of the slicer so it is only necessary to demonstrate the principle using one of the beams with the understanding that the same effect will be observed with both beams combined and properly aligned. Another point to mention is that by using only one of the beams a more direct comparison can be made to the non-slicer spectrograph because the possibility of subtle effects due to misalignment and non-equality between the through and sliced beam may be eliminated.

The results conclude that the 2X refractive slicer does not offer any improvement to the SD-OCT system as compared to the non-sliced spectrograph. This is because the slicer is not behaving ideally (perfect 2X reduction in spot width) in the regime the SD-OCT system spectrograph is operating in; however, this does not imply that the slicer is not working properly. The only possible explanation of the behaviour of the slicer is that the optical elements contained within the slicer cause a degradation in the étendue such that the resulting spot size after being focused by the camera lens ends up being the same as the original spot size, i.e. the 2X refractive slicer has a working slicing factor less than 1X. In section 4.4 the étendue for the spectrograph was $\Xi = 298.556$ [μm^2 sr], but for the SD-OCT spectrograph the étendue is $\Xi = 2.62$ [μm^2 sr], over two orders of magnitude smaller. An in depth optical model and ray trace of the refractive slicer is necessary to confirm this hypothesis.

5.2.3 Zemax Model of the Slicer

The concluding result from the data collected to measure the spectral coherence envelopes for the sliced and non-sliced spectrograph in the SD-OCT system is that the 2X refractive slicer offered no fringe contrast improvement, and it was hypothesized that the reason for this is because the focused spot size after passing through the slicer ends up being about the same as the original spot size without the slicer. The idealized theoretical predictions were unable to foresee this effect because the model was too simplistic and did not take into account the effects of optical aberrations. The discussions of optical aberration theory in section 2.1.4 alluded to the point that the most effective way to fully analyze an optical system is to put it through a ray tracing software package. By modelling the 2X refractive slicer in a ray tracing environment the exact distribution of light incident on the detector may be found, which of course gives the ultimate focused spot size.

The ray tracing software package ZEMAX®, herein referred simply as Zemax, was used to model the 2X refractive slicer. Zemax is an optical modelling software package that allows for ray tracing to analyze a complex optical system [64]. The general design of the 2X refractive slicer as described in section 4.3 including the spectrograph collimating lens

and camera lens were input into the Zemax program. The actual lens prescriptions and coatings were available to download from the Thor Labs website so the real lens model was used. A 3D model of the 2X refractive slicer can be seen in fig. 4.7. The most powerful tool in Zemax, for our application, will be to compute the final focused spot shape of the 10 μm circular pinhole object after it passes through the slicer, and compare this to the final focused spot shape if no slicer were present. For these purposes the spot diagram analysis tool and the image simulation tool were used.

Spot Diagram Analysis

The spot diagram analysis tool produces a map of the locations of a starting ray bundle after it passes through the prescribed optical system; this procedure is executed by employing the ray tracing equations (eqns. 2.10 and 2.11). For our purposes it is desirable to examine the spot diagrams for the three extreme wavelengths in the SD-OCT system (800 nm, 850 nm, and 900 nm). We also wish to produce spot diagrams for a bundle of rays starting in the centre of the pinhole, at the edge of the pinhole (10 μm), and at the radial location corresponding to half the area (7.07 μm). The spot diagrams for these various conditions, both with and without the slicer, are shown in figs. 5.14-5.19. A list summarizing the diffraction limited spot size and the aberrated spot sizes for the sliced and non-sliced spectrograph is given in table 5.2.

The spot diagrams indicate that the focused spot shape is largely affected by aberrations and especially for the extreme wavelengths of 800 nm and 900 nm. The extreme wavelengths pass through the camera focusing lens at angles of $\pm 4^{\circ}$, therefore showing that the off-axis performance of the single achromatic doublet camera lens is quite poor. The differences in the spot diagrams between different areas of the 10 μm diameter object are negligible compared with the size of the spot diagram, as can be visually observed in figs. 5.14-5.19.

For the on-axis case (850 nm) for the slicer and non-slicer, the spot diagrams appear to be only slightly larger than the diffraction limit, meaning that most of the imaged rays from the ray trace fall within the Airy diameter. For the off-axis case for the slicer and non-slicer, the spot diagrams show that the aberrations caused by the camera focusing lens result in focused rays spreading much further out from the Airy diameter. The most significant aberrations affecting the spot size in the off-axis case are coma and astigmatism, a summary of these aberrations are described in section 2.1.4. The rays are spread out much more horizontally than vertically because the horizontal tilt angle is $\pm 4^{\circ}$ while the vertical tilt angle is 0°. In the sliced spectrograph the rays are not spread out as much vertically as they are in the non-sliced spectrograph, as can be seen by observing figs. 5.14, 5.17, 5.16, and 5.19.

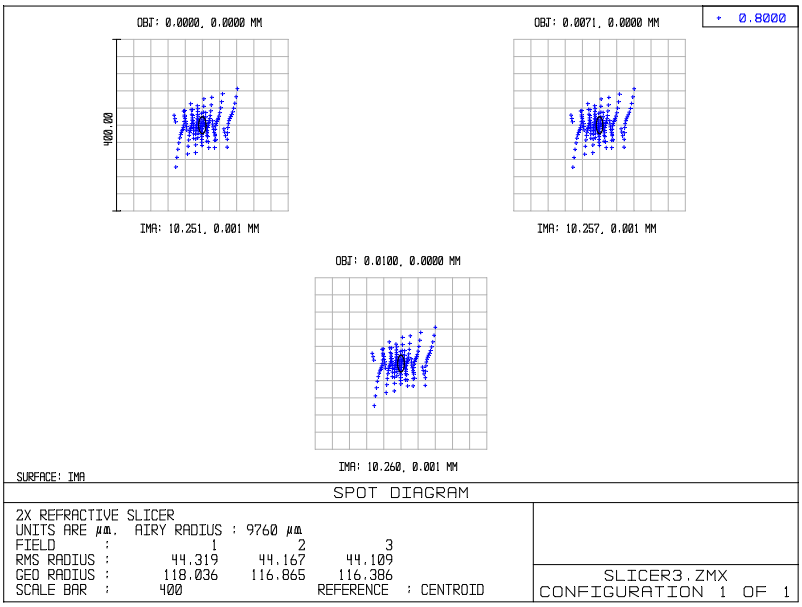

Figure 5.14: Spot diagram for the 10 μm extended source imaged through the sliced spectrograph for 800 nm light.

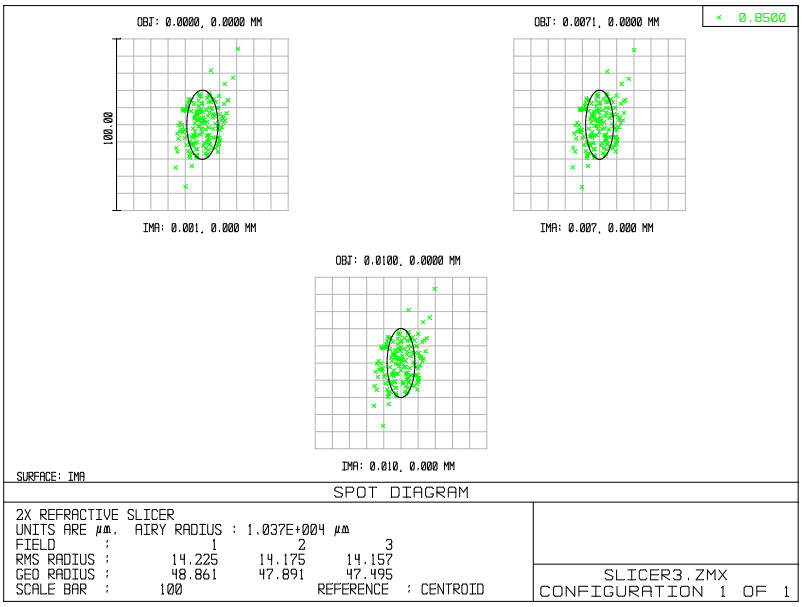

Figure 5.15: Spot diagram for the 10 μm extended source imaged through the sliced spectrograph for 850 nm light.

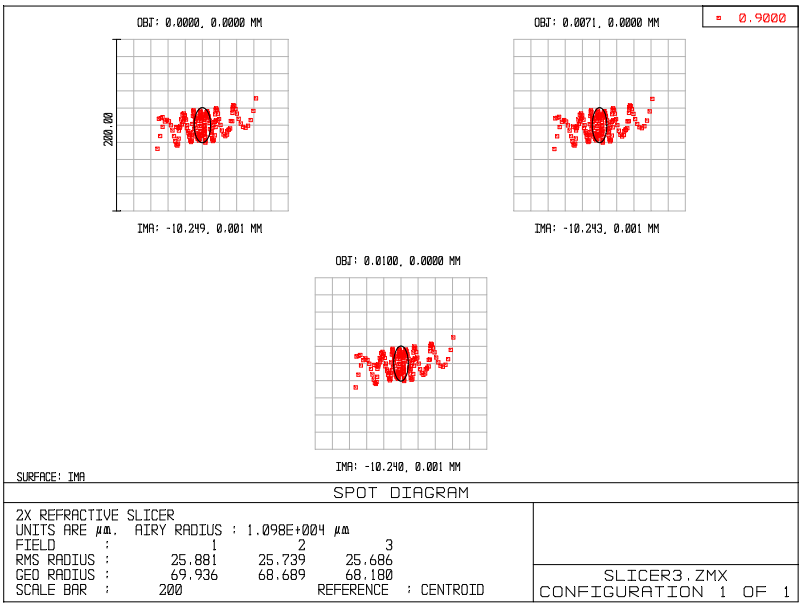

Figure 5.16: Spot diagram for the 10 μm extended source imaged through the sliced spectrograph for 900 nm light.

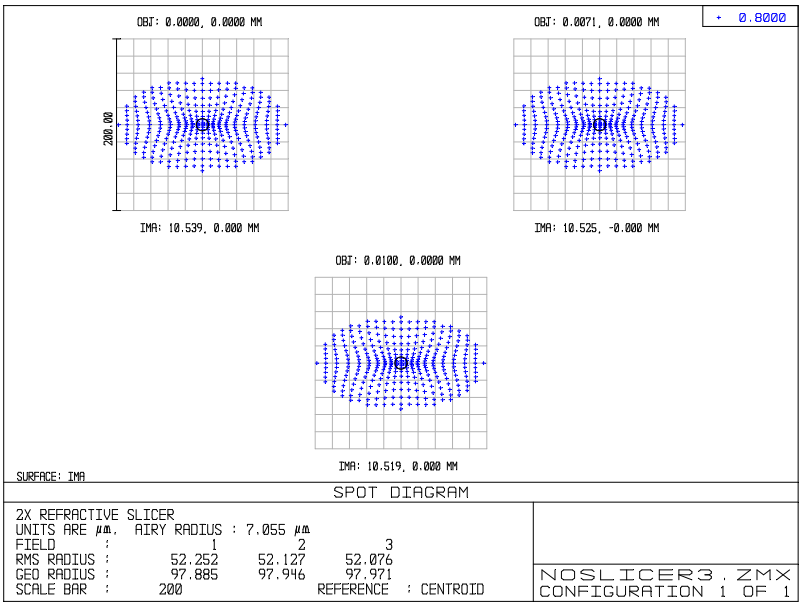

Figure 5.17: Spot diagram for the 10 μm extended source imaged through the non-sliced spectrograph for 800 nm light.

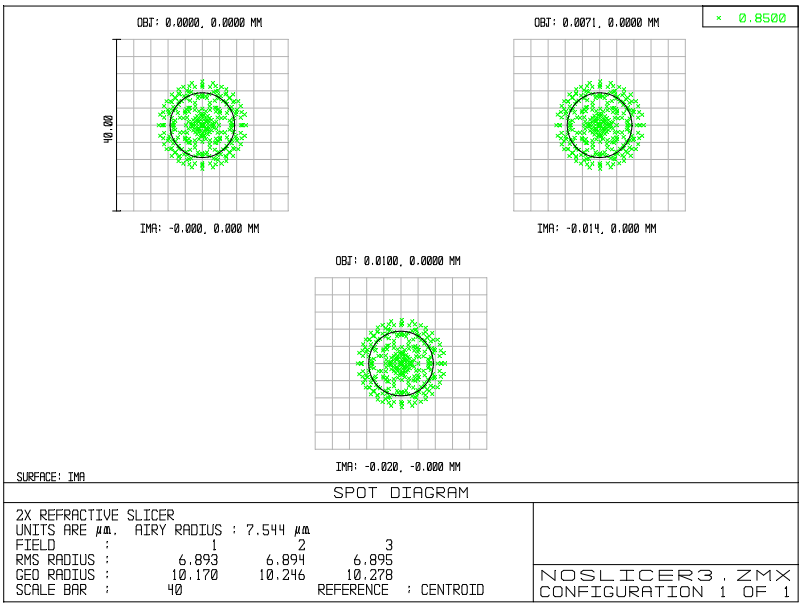

Figure 5.18: Spot diagram for the 10 μm extended source imaged through the non-sliced spectrograph for 850 nm light.

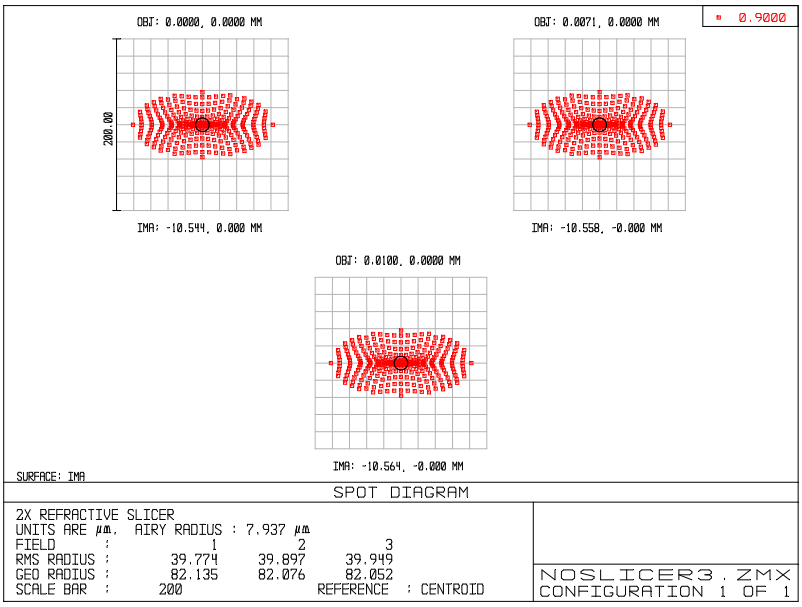

Figure 5.19: Spot diagram for the 10 μm extended source imaged through the non-sliced spectrograph for 900 nm light.

Theoretical Spot Diagram Results				
	Non-Slicer		Slicer	
Wavelength	**Airy Diam.**	**Spot size**	**Airy Diam.**	**Spot size**
800 nm	14.11 μm	200 μm	20 μm	160 μm
850 nm	15.09 μm	20.5 μm	20 μm	30 μm
900 nm	15.87 μm	160 μm	20 μm	120 μm

Table 5.2: A table listing the approximate diffraction limited Airy diameter as well as the aberrated spot size diameter for the 10 μm extended pinhole source using the sliced and non-sliced spectrograph in the SD-OCT system. The diameters are in the dispersive x-direction only.

Image Simulation Analysis

The image simulation tool in Zemax extends upon the ray tracing procedure to produce an actual simulated image of a user defined input object. Essentially the tool produces a spot diagram for every point in an object. The actual implementation and variables that go into this tool are beyond the scope of this thesis and the reader is referred to the program documentation [64]. The input parameters to run the image simulation tool, as well as the starting object image, can be found in table 5.3 and fig. 5.20. The resulting simulated images of the pinhole object relevant to the SD-OCT system both with and without a slicer in the spectrograph can be found in fig. 5.21. The widths were calculated by vertically binning the spot images, and then measuring the FWHM of a Gaussian fit to the curve, these plots can be seen in fig. 5.22. A list giving the measured FWHM spot sizes for the non-sliced and sliced spectrograph can be found in table 5.4.

The spot images for the non-sliced and sliced spectrograph shown in fig. 5.21 agree well with the spot diagram images in figs. 5.14-5.19. The images, however, show the density of rays more clearly so they provide a better understanding on how the non-sliced and sliced spectrograph behave. In the spot diagrams the horizontal spreading of the rays away from the Airy diameter appeared to be quite significant, but the generated images show that these rays do not contribute towards a significant fraction of the total amount of light. Before with the spot diagrams the widths in table 5.2 were given in terms of the maximal horizontal extent, however, with the simulated images a FWHM may easily be computed, which provides a better metric for the spot size width.

The FWHM values for the sliced images is less than the non-sliced images for all wavelengths, as is shown in table 5.4. For the on-axis case of 850 nm the simulated images show the slicer provides a width reduction by a factor of 1.27, but the off-axis cases for 800 nm and 900 nm show reduction factors of 1.01 and 1.27; clearly the slicer does not provide much improvement at the shorter wavelengths near 800 nm. This is partly due

to the fact that even the non-sliced spectrograph has much worse performance at these wavelengths compared to the longer wavelengths, which is an indication of large chromatic aberration.

Conclusions

In section 5.1.1 using the idealized simulation a slicing factor of 1.377X was predicted. From the measured simulated images a slicing factor of 1.27X was seen for wavelengths 850 nm to 900 nm and with virtually no improvement for 800 nm light. The Zemax simulation for on-axis light is only slightly worse than the ideal IDL simulation, however both of these results indicate that some improvement in the coherence envelope should be observed in the SD-OCT system—this was not the case. The measured data presented in section 5.2.2 show that the slicing factor is less than 1X so there appears to be a mismatch between theoretical predictions and measured results. The goal is then to develop a more accurate theoretical model of the sliced and non-sliced spectrograph to match the measured results.

Image Simulation Input Parameters	
Parameter	**Value**
Field size	10 μm
Image Size	600 μm
# Rays	5×10^6
# Pixels	600 x 600

Table 5.3: A table listing the input parameters to the geometric image simulation tool in Zemax.

Image Simulation Spot Widths		
Wavelength	**Non-slicer**	**Slicer**
800 nm	45.125 μm	44.625 μm
850 nm	20.500 μm	16.125 μm
900 nm	34.875 μm	27.500 μm

Table 5.4: A table listing the spot widths from the simulated images for the non-sliced and sliced spectrograph. The widths are measured by FWHM.

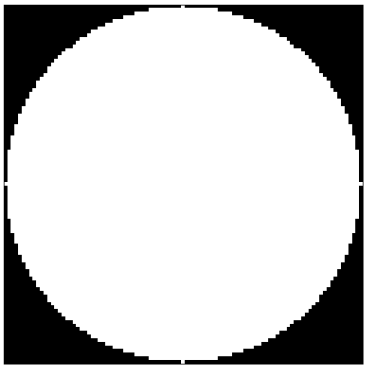

Figure 5.20: The circle image used as the starting object in the Zemax geometric image simulation tool.

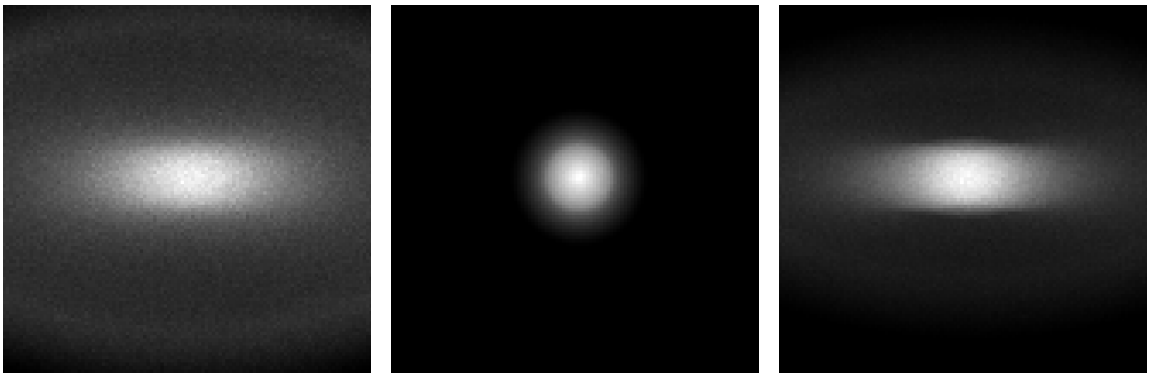

(a) 800 nm (b) 850 nm (c) 900 nm

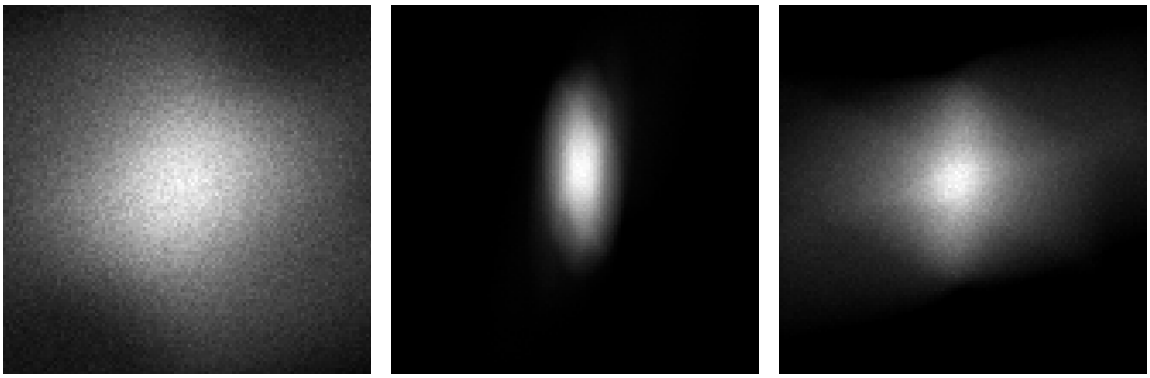

(d) 800 nm (e) 850 nm (f) 900 nm

Figure 5.21: The resulting spot images from the Zemax image simulation tool. Figs. (a)-(c) are without the slicer, and figs. (d)-(f) are with the slicer.

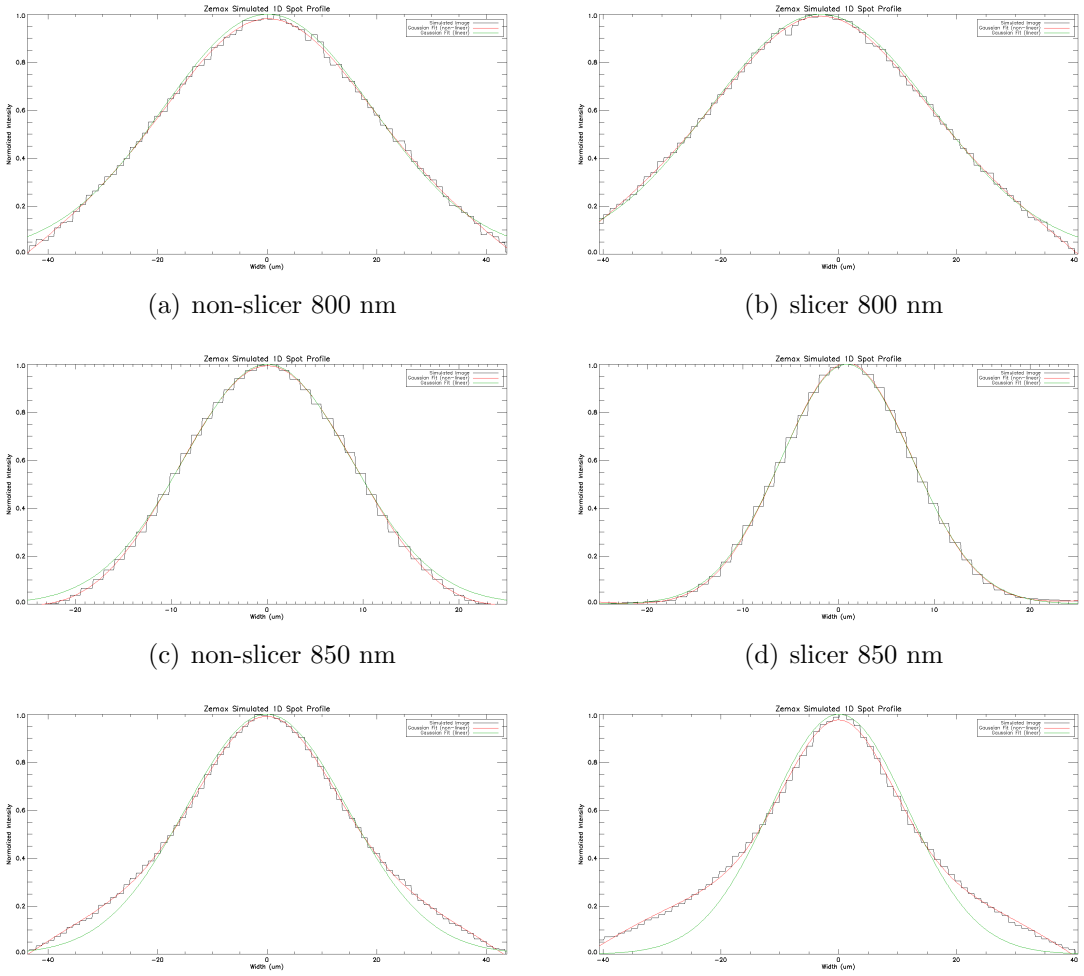

(a) non-slicer 800 nm

(b) slicer 800 nm

(c) non-slicer 850 nm

(d) slicer 850 nm

(e) non-slicer 900 nm

(f) slicer 900 nm

Figure 5.22: The vertically binned pinhole images generated using Zemax for the non-sliced and sliced spectrograph. Over-plotted are a non-linear and linear Gaussian curve fit to the image simulation results.

5.2.4 Updated Simulation

In the previous simulation we had assumed the pinhole object formed a perfect image in the focal plane of the camera lens and we did not take into account any aberrations. We have seen from ray tracing results in section 5.2.3 that the pinhole image is largely affected by aberrations, in both the sliced and non-sliced case. In order to properly explain the measured results presented in section 5.2.2 the effect of the aberrated image must be taken into account in the simulation model. The other assumption of using the same Airy pattern

for both the slicer and non-slicer must also be re-examined.

The most important thing to change in the simulation is the shape and size of the pinhole image function. We can no longer assume a perfect image, as was shown in fig. 5.2, rather we must construct an image that accurately represents the image simulation results given in section 5.2.3. The vertically binned 1D images from the Zemax simulated pinhole images shown in fig. 5.21 are shown in fig. 5.22 along with a linear and non-linear Gaussian curve fit. We wish to use these data sets to construct the imaging PSFs in the updated simulation. Since the measured results for the coherence envelope were only done using the on-axis data due to poor off-axis performance, the updated simulation will only generate imaging PSFs using the Zemax simulation results for the on-axis 850 nm light.

The updated pinhole images were constructed by generating Gaussian functions with FWHM values matching the values in table 5.4 for the on-axis 850 nm light only. These two pinhole images, one for the slicer and one for the non-slicer, were convolved with vertically binned Airy patterns with diameters taken from table 5.2 in order to generate the updated imaging PSFs. Since the goal of the updated simulation is to match the measured results, the FWHM values used to generate the Gaussian pinhole images were allowed to increase or decrease. Once final values are obtained, as is indicated by a close match between theory and experiment, the resulting spot widths may be compared to directly measured spot widths.

Updated Simulation Results

Using the two new pinhole images shown in fig. 5.23, the rest of the simulation may be performed unaltered. The resulting FWHM values for the aberrated pinhole images are 20.5 μm and 21.5 μm. The imaging PSFs are convolved with the spatial pixel response function to generate the overall average pixel bandpass for the non-sliced and sliced spectrograph. These bandpass functions are then Fourier transformed to generate the coherence envelopes that describe the fringe visibility versus depth relationship for the two types of spectrographs. The resulting coherence envelopes can be seen in fig. 5.24(a) and the relative improvement between sliced and non-sliced spectrograph in SD-OCT can be seen in fig. 5.24(b).

Discussion of Updated Simulation Results

The updated simulation now matches the measured results very closely, as can be seen by comparing the coherence envelopes in figs. 5.24(a) and 5.13(a), and the coherence envelope enhancement functions shown in figs. 5.24(b) and 5.13(b). Both simulation and measurement show a small width reduction in the coherence envelope for the sliced SD-OCT system and the ratio of the coherence envelopes shows a downward trend in fringe

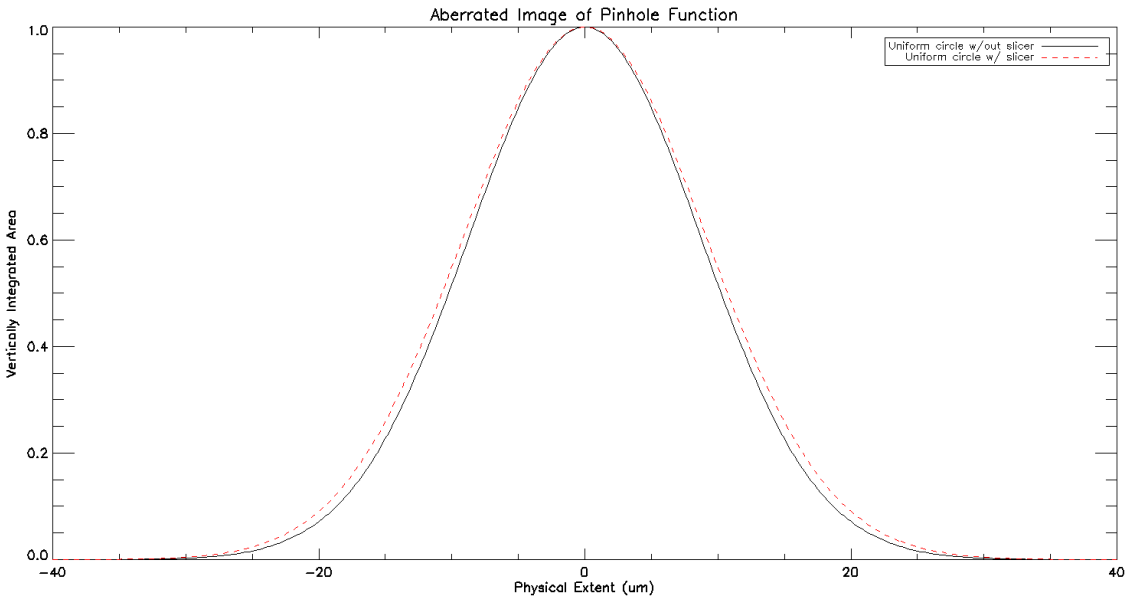

Figure 5.23: A plot showing the vertically integrated aberrated image of the pinhole on the camera focal plane. The plot shows the results for both without (black solid) and with (red dashed) a slicer in the system. These functions are to be convolved with the Airy pattern to form the imaging PSFs.

visibility improvement factor with a degrading factor of slightly less than 0.5X at 3.7 mm of imaging depth.

The Gaussian pinhole images have FWHM values of 20.5 μm and 21.5 μm. These values may be compared to the widths of the directly imaged focused spots from the sliced and non-sliced spectrograph for on-axis 850 nm light. Images of the directly imaged spots are shown in fig. 5.25. The same camera focusing lens and a high quality web-cam with 6 μm by 6 μm square pixels was used to generate these images. The images are highly pixelated because the spot size should be on the order of 20 μm, which only corresponds to between 3 and 4 pixels. A non-linear Gaussian function was fit to the vertically binned image in order to measure the FWHM of the spot. The resulting values are summarized on table 5.5. Because so few pixels were used in this method the accuracy is not very high so large error bars of ± 3 μm (half a pixel width) are applied to the uncertainty in these measurements. The simulation FWHM values of 20.5 μm and 21.5 μm are within the error bar so the results seem reasonable. The sliced spot size increase from the Zemax simulated result of 16.125 μm to the updated matched measurement simulation of 21.5 μm means that the slicer is performing 33% worse than expected in practise.

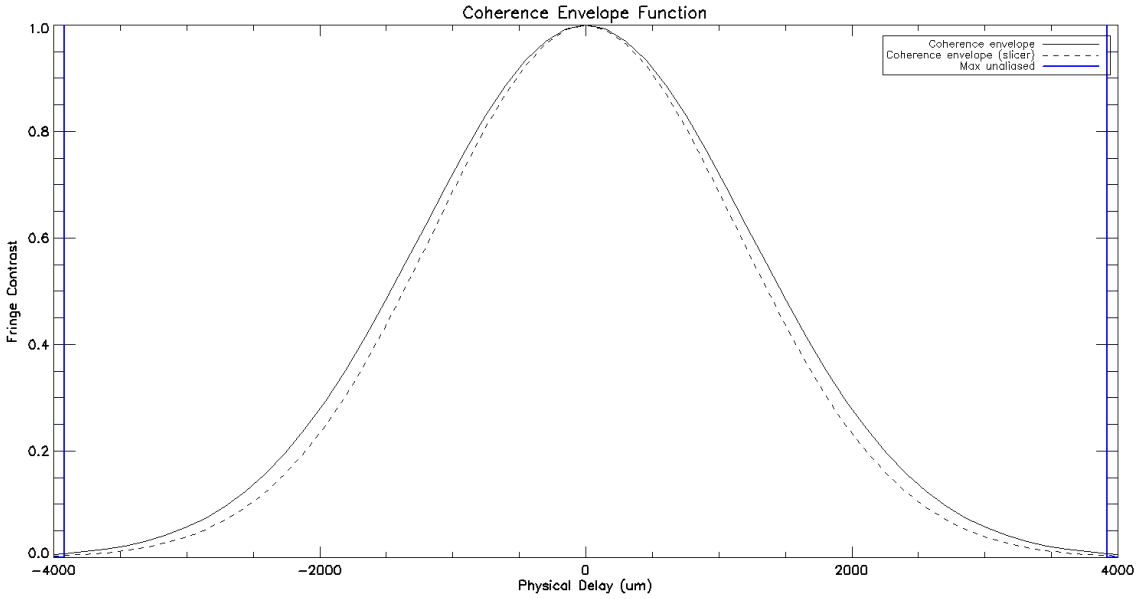

(a) Spectral Coherence Envelopes

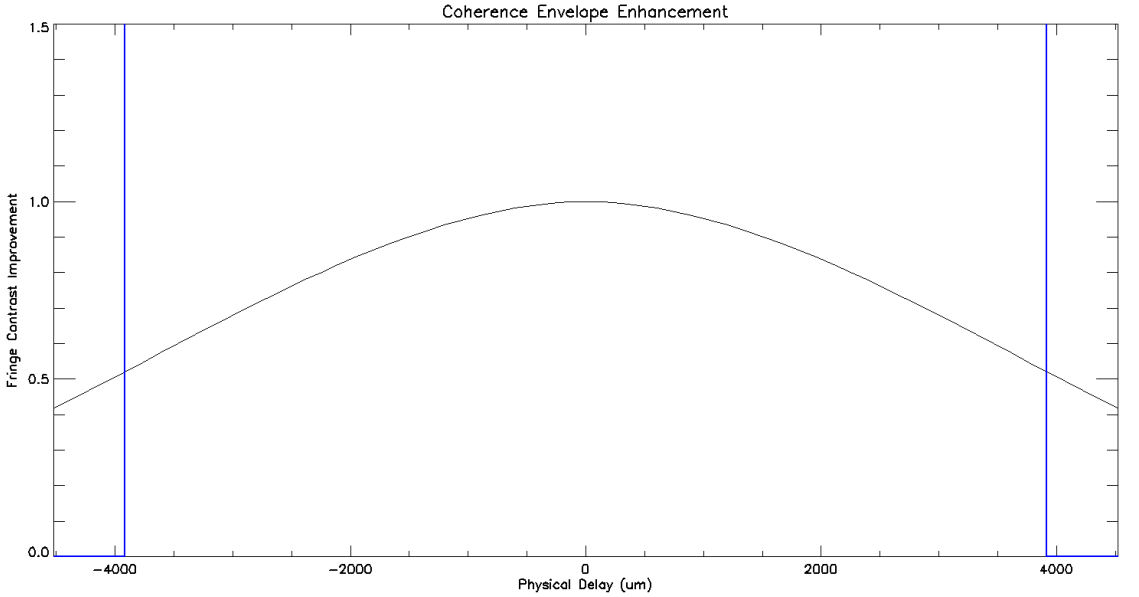

(b) Relative Fringe Contrast Ratio

Figure 5.24: (a) The non-sliced envelope is shown as solid black and the sliced envelope is shown as dashed black. (b) Ratio of coherence envelopes showing the effect of the slicer on the SD-OCT system.

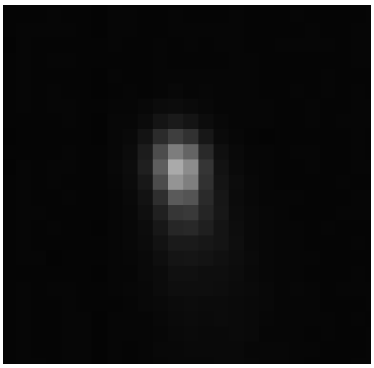

(a) Non-Slicer

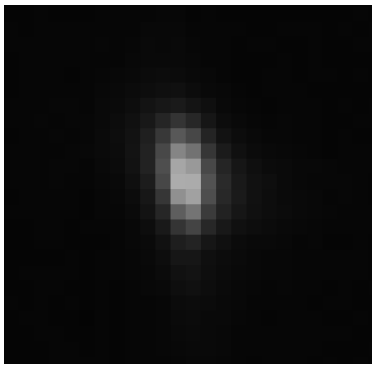

(b) Slicer

Figure 5.25: An image of the non-sliced and sliced spot imaged directly.

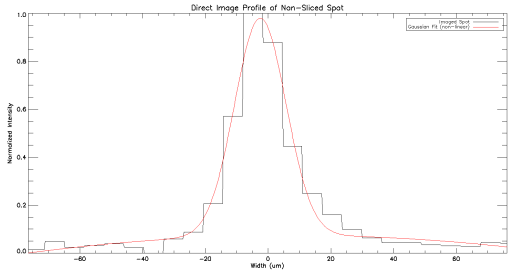

(a) Non-slicer

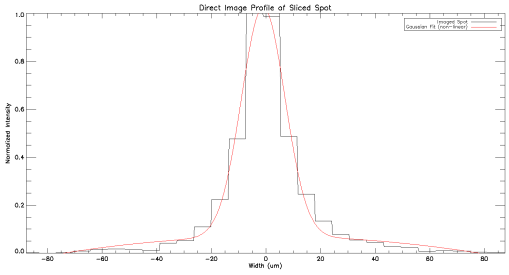

(b) Slicer

Figure 5.26: The vertically binned profiles of the direct imaged spots from (a) the non-sliced spectrograph and (b) the sliced spectrograph

Direct Spot Image Widths	
Non-Slicer	**Slicer**
20.2±3.0 μm	19.3±3.0 μm

Table 5.5: The widths of the directly imaged spots for the slicer and non-slicer in the SD-OCT system. These values are measured by FWHM from the non-linear Gaussian fitted functions in figs. 5.26(a) and 5.26(b).

5.3 Necessary Improvements Required in the SD-OCT System

The current implementation of the SD-OCT system spectrograph introduces significantly strong aberrations, therefore limiting the performance. The largest aberrations are introduced by sending the light through the camera lens at the dispersion angles of about $\pm 4^{\circ}$ from the diffraction grating. If the aberrated spot size is larger than the perfect pinhole image then slicing the image will have a smaller effect, therefore reducing the working slicing factor (WSF). It is with this point in mind that in order to use a slicer effectively, in general, the object of interest should be significantly larger than the aberrations introduced. In the current implementation of the SD-OCT system spectrograph the aberrated spot size plus the diffraction limit, 15 μm, varies between 21.4 μm for 850 nm light on-axis to 45.7 μm and 35.5 μm for 800 nm and 900 nm light off-axis. The aberrated spot size plus the diffraction limit, 20 μm, from the refractive 2X slicer was shown to be 18.0 μm, 45.6 μm, and 28.8 μm for the wavelengths 850 nm, 800 nm, and 900 nm. Dividing the two results gives the working slicing factor for the SD-OCT system spectrograph, calculated to be 1.19X for 850 nm, 1.00X for 800 nm, and 1.23X for 900 nm. These results are summarized in table 5.6. Also shown are the WSF values if the 33% increase in sliced spot size is taken into account, that was proposed in section 5.2.4. Each of those resulting values are less than 1.

The relative effect of the aberrations on the spot size introduced by the base spectrograph may be taken by dividing the measured aberrated spot widths in table 5.4 by 20 μm. Similarly the relative effect of aberrations on the spot size introduced by the slicer may be computed by dividing the sliced spot widths by 10 μm and dividing out the aberrations introduced by the base spectrograph alone. These results are summarized in table 5.7.

Both the base spectrograph and the 2X refractive slicer induce too many aberrations and limit the performance of the SD-OCT system. The aberrations induced by the spectrograph limit the off-axis performance and make the ideal WSF (2.0X) smaller than desired, and the aberrations induced by the refractive slicer continue to worsen this effect. In order to make a substantial improvement to the system a better performing base spectrograph is needed that is able to provide diffraction limited performance. A better performing slicer is also needed since the 2X refractive slicer induces many aberrations theoretically, and practically the aberration factor is larger than 2, meaning the sliced spot is always larger than the non-sliced spot.

Aberrated Slicing Results					
Wavelen.	**Non-Slicer**	**Slicer**	**Slicer+33%**	**WSF**	**WSF-33%**
800 nm	45.68 μm	45.56 μm	60.28 μm	1.0026	0.7578
850 nm	21.48 μm	18.04 μm	23.04 μm	1.1907	0.9323
900 nm	35.52 μm	28.80 μm	37.72 μm	1.2333	0.9417

Table 5.6: The spot widths of the spectrograph using the values from table 5.4 and taking into account the Airy diameters given in table 5.2. The ratio between the widths gives the working slicing factor.

Aberration ratios				
Wavelength	**Spect.**	**Spec.+Slicer**	**Slicer**	**Slicer+33%**
800 nm	2.2562	4.4625	1.9778	2.6371
850 nm	1.0250	1.6125	1.5731	2.0975
900 nm	1.7437	2.7500	1.5770	2.1027

Table 5.7: The aberration factor introduced by the base spectrograph, base spectrograph and the slicer, and the aberration factor introduced by the slicer itself. The values were computed by dividing the spot widths in table 5.4 by the ideal unaberrated spot width. These values do not take into account diffraction.

5.3.1 Improvements Needed in the Spectrograph

The performance of the base spectrograph will affect the overall depth imaging performance of the SD-OCT system. The large aberration factors presented in table 5.7 show that the off-axis performance of the spectrograph induces aberrations increasing the spot widths on the order from 75% to 125%, with the shorter wavelengths being affected more than the longer wavelengths. This type of performance is unacceptable to construct a high-performance SD-OCT system and will limit the practical imaging depth since the coherence envelope is quite narrow, or will mean trading off imaging depth for axial resolution since only the centre 20 nm gives acceptable performance. Choosing the latter option is a waste of resources since the source bandwidth is 100 nm and a high-quality diffraction grating is used with a large area detector. The best way to improve the performance of the base spectrograph is to use a camera lens that is designed to reduce the off-axis aberrations, such as coma, astigmatism, and field curvature, and also reduce the on-axis aberrations such as spherical and chromatic—a description of these aberrations can be found in section 2.1.4.

A complex three element lens oriented in an image telecentric configuration (XP located at infinity) was designed with off-the-shelf parts. This lens design was based off of a previous prescription used in other SD-OCT systems [18]. The complex lens uses two achromatic doublet lenses placed in a symmetric configuration (flint-crown, crown-flint),

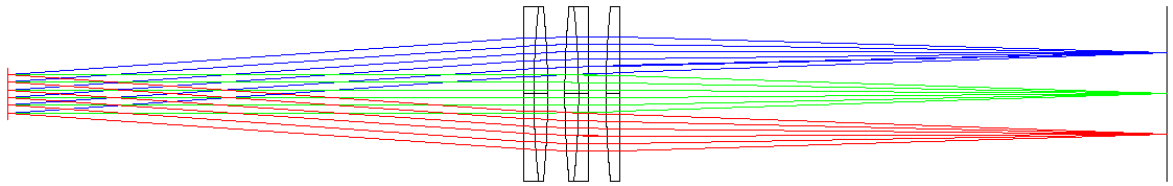

Figure 5.27: The design of the complex three element lens to upgrade the performance of the SD-OCT system spectrograph.

Spectrograph Lens Prescription			
Surface	**Radius**	**Thickness**	**Material**
1	Infinity	3.000 mm	N-SF6HT
2	234.470 mm	4.000 mm	N-BAF10
3	-261.187 mm	5.000 mm	AIR
4	261.187 mm	4.000 mm	N-BAF10
5	-234.470 mm	3.000 mm	N-SF6HT
6	Infinity	5.000 mm	AIR
7	254.920 mm	4.000 mm	N-BK7

Table 5.8: The general prescription for the custom complex three element camera lens design. Surfaces 1-5 are the two achromatic doublet lenses and surfaces 6-7 is the convex-plano singlet lens.

followed by a convex-plano singlet lens. Each of the lens elements were separated by 5 mm since this is the standard size of two 2" retaining rings (Thor Labs, SM2RR). The achromatic doublets used in the design are 2" in diameter and have a 500 mm focal length with design wavelengths of 706.5 nm, 855 nm, and 1015 nm (Thor Labs, AC508-500-B), and the convex-plano lens used is 2" in diameter and has a 500 mm focal length and is made of N-BK7 glass (Thor Labs, LA1380-B). The general prescription is given in table 5.8 and the lens design is shown in fig. 5.27.

The upgraded camera lens has an effective focal length of 169.6 mm and a diameter of 2". The lens is placed 151.6 mm after the diffraction grating so that the system is telecentric in image space. Image space telecentric means that the exit pupil is located at infinity so the chief ray is also located at infinity (see section 2.1.3). This design configuration reduces the off-axis aberrations (coma, astigmatism, field curvature, etc), and decouples image magnification from defocus. Aberrations are further reduced from the multiple element design employing advanced lens design techniques of symmetry, lens-breaking, and field correctors [27].

Upgraded Performance Results

In order to evaluate the performance of the upgraded spectrograph an identical procedure of generating aberrated spot images that was employed in section 5.2.3 was used. From the simulated images generated using Zemax the FWHM of the spots can be calculated from the vertically binned spot profiles. The FWHM values can furthermore be used in the updated IDL simulation to produce the spectral coherence envelope. The resulting simulated images from Zemax for the upgraded non-sliced spectrograph can be seen in fig. 5.28, the resulting vertically binned spot profiles are shown in fig. 5.29, and the FWHM values for the spot widths are summarized in table 5.9.

The spot images generated from using the upgraded spectrograph show much better off-axis performance compared with the single camera lens spectrograph. The simulated spot images do not show idealized results partly due to the fact that the three element lens design is not a complete custom lens design and the design wavelengths for the achromats do not match the system wavelengths. However, the simplicity of this design make up for a small amount of performance sacrificed. Another thing to note about the results is that the spot width on-axis is larger than the spot widths off-axis, contrary to what might normally be expected for an off-axis optical system. This is a classic result in lens design for off-axis systems where some on-axis performance is sacrificed in order to boost the performance off-axis [27].

5.3.2 Improvements Needed in the Slicer

The performance of the 2X refractive slicer in the SD-OCT system was shown to introduce aberrations that increase the spot size to be larger than the non-sliced spot size. In an ideally performing 2X refractive slicer the final focused spot size should have been less than the non-sliced spot size, as are indicated by the WSFs in table 5.6, however the performance of the 2X refractive slicer is not perfect and was shown to perform 33% worse than expected; given the 33% degradation the WSFs are reduced to below 1.00. The refractive slicer contains singlet cylindrical lenses for the beam compressor section which introduces significant chromatic aberrations and results in poor collimation for the design wavelengths for the SD-OCT system. The beam expander section of the refractive slicer does contain achromatic doublet lenses, but the design wavelengths are 706.5 nm, 855 nm, and 1015 nm, which do not match the SD-OCT design wavelengths of 800 nm, 850 nm, and 900 nm. This will induce secondary chromatic aberration effects and further degrade the refractive slicer performance. In all cases of the refractive slicer spherical lenses are used (surfaces with spherical curvature), which induce spherical aberrations. A higher performing 2X slicer is needed that reduces the effect of the aberrations significantly to the point where the slicer is diffraction limited.

There are two major improvements than can be made in order to boost the performance of the 2X slicer significantly. First, all reflective elements can be used to eliminate chromatic aberration. Second, parabolic surfaces can be used to reduce spherical aberrations; it is a well known result in lens design that parabolic surfaces can reduce spherical aberration [27]. With these ideas in mind a 2X reflective diffraction limited slicer was designed. The results from this upgraded slicer are presented here but the details of the design are included in section 5.4.

Upgraded Performance Results

In a similar fashion to the upgraded spectrograph results presented in section 5.3.1, the upgraded slicer was modelled in Zemax and simulated images of the focused spot in the upgraded spectrograph were generated. These images were vertically binned and the FWHM values were computed. The FWHM values can be used to generate the spectral coherence envelope of the predicted SD-OCT system. The resulting simulated images from Zemax for the upgraded sliced spectrograph can be seen in fig. 5.28, the resulting vertically binned spot profiles are shown in fig. 5.29, and the FWHM values for the spot widths are summarized in table 5.9.

The spot widths for the upgraded slicer placed in the upgraded spectrograph are narrower than the spot widths with the refractive slicer in the single lens spectrograph. The off-axis performance is greatly enhanced due to the upgraded spectrograph lens and because the reflective slicer does not have any chromatic aberration. The off-axis performance is not ideal, but this is not inherently due to the slicer, but rather the upgraded spectrograph lens, as was discussed in section 5.3.1.

Image Simulation Spot Widths				
	Non-Slicer		**Slicer**	
Wavelength	**Width**	**Airy Diam.**	**Width**	**Airy Diam.**
800 nm	23.000 μm	17 μm	13.625 μm	21 μm
850 nm	25.125 μm	17 μm	10.250 μm	21 μm
900 nm	21.750 μm	17 μm	18.875 μm	21 μm

Table 5.9: A table listing the spot widths from the simulated images for the upgraded spectrograph and slicer. The widths are measured by FWHM. Also included is the diffraction limited Airy diameter.

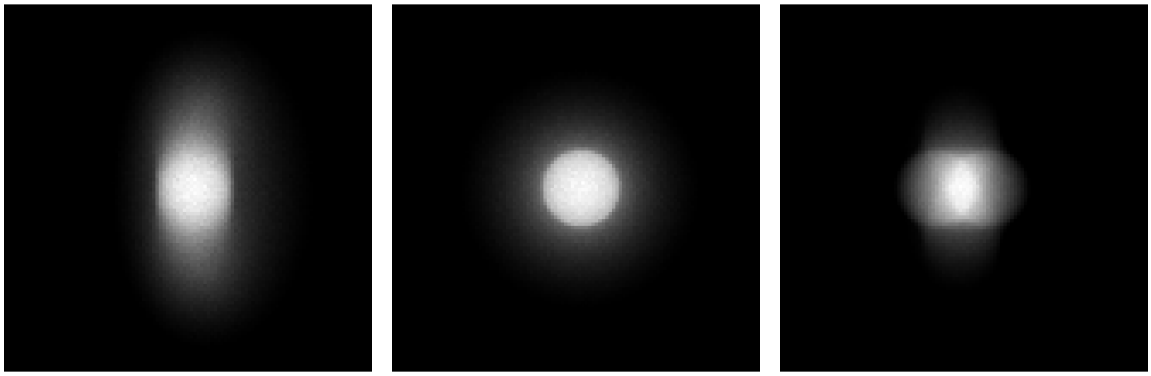

(a) 800 nm (b) 850 nm (c) 900 nm

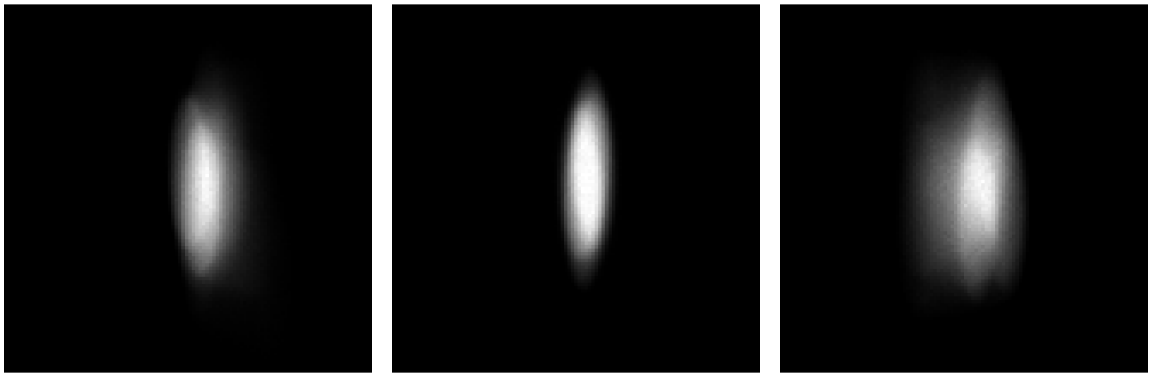

(d) 800 nm (e) 850 nm (f) 900 nm

Figure 5.28: The resulting spot images from the Zemax image simulation tool for the upgraded spectrograph (a)-(c), and with the upgraded slicer (d)-(f).

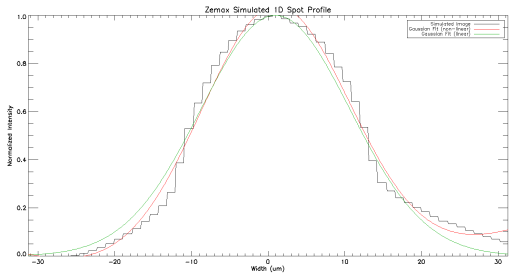

(a) non-slicer 800 nm

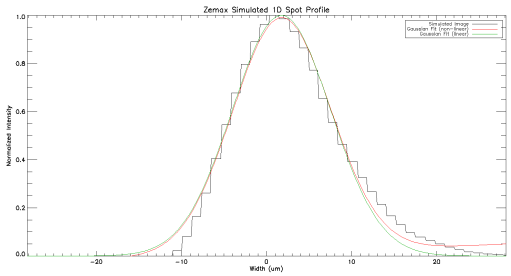

(b) slicer 800 nm

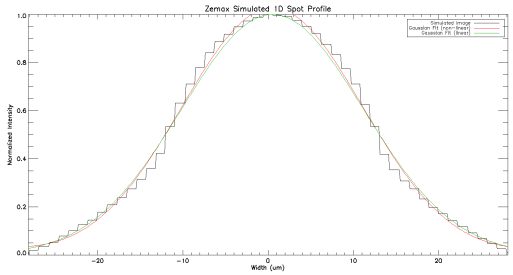

(c) non-slicer 850 nm

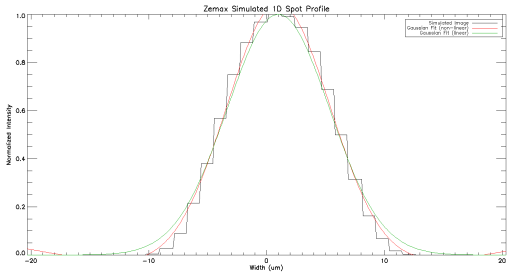

(d) slicer 850 nm

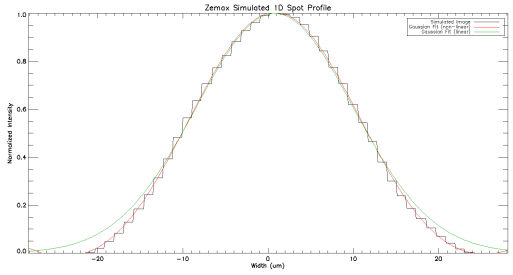

(e) non-slicer 900 nm

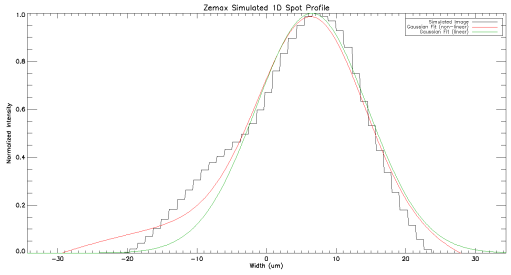

(f) slicer 900 nm

Figure 5.29: The vertically binned pinhole images generated using Zemax for the upgraded spectrograph and upgraded slicer. Over-plotted are a non-linear and linear Gaussian curve fit to the image simulation results.

Aberrated Slicing Results					
Wavelen.	**Non-Slicer**	**Slicer**	**Slicer+33%**	**WSF**	**WSF-33%**
800 nm	24.12 μm	16.00 μm	20.08 μm	1.5075	1.2012
850 nm	26.16 μm	13.20 μm	16.04 μm	1.9818	1.6310
900 nm	22.92 μm	20.72 μm	26.68 μm	1.1061	0.8591

Table 5.10: The spot widths of the upgraded spectrograph using the values from tables 5.9 taking into account the Airy diameters. The ratio between the widths gives the working slicing factor.

Aberration ratios				
Wavelength	**Spect.**	**Spect.+Slicer**	**Slicer**	**Slicer+33%**
800 nm	1.0171	1.2050	1.1848	1.5797
850 nm	1.1111	0.9065	0.8159	1.0879
900 nm	0.9618	1.6693	1.7356	2.3142

Table 5.11: The aberration factor introduced by the upgraded spectrograph, upgraded spectrograph and the upgraded slicer, and the aberration factor introduced by the upgraded slicer itself. The values were computed by dividing the spot widths in table 5.9 by the ideal unaberrated spot width. These values do not take into account diffraction.

5.3.3 Predicted SD-OCT System Performance with the Upgraded Spectrograph and Slicer

The final spot size taking into account the diffraction Airy spot is used to predict the working slicing factor (WSF). The final focused spot sizes for the upgraded non-sliced spectrograph with an Airy diameter of 17 μm are 24.1 μm, 26.2 μm, and 22.9 μm for the wavelengths 800 nm, 850 nm, and 900 nm. Similarly for the reflective slicer with an Airy diameter of 21 μm the final focused spot widths are 16.0 μm, 13.2 μm, and 20.7 μm for the wavelengths 800 nm, 850 nm, and 900 nm. The ratio of the spot widths gives the WSF which are calculated to be 1.51, 1.98 and 1.11 for 800 nm, 850 nm, and 900 nm. The measured results from the refractive slicer showed a 33% increase in spot widths, taking this as a worse-case scenario for the upgraded reflective slicer the WSFs are calculated to be 1.20, 1.63, and 0.86. With the exception of 900 nm light, even in a worse-case scenario the upgraded slicer will still show an improvement. It is not believed that a 33% error will be observed in the upgraded slicer because very high precision optical components are used in the design (see section 5.4). The upgraded slicing results are summarized in table 5.10.

The relative effect of the aberrations introduced by the upgraded spectrograph may be taken by dividing the measured aberrated spot widths in table 5.9 by 22.61 μm (imaging

magnification is 2.26 with a 10 μm pinhole). Similarly the relative effect of the aberrations introduced by the upgraded slicer may be computed by dividing the sliced spot widths in table 5.9 by 11.30 μm and dividing out the aberrations introduced by the upgraded spectrograph alone. These results are summarized in table 5.11.

In both the cases for the 900 nm light in the upgraded spectrograph and the 850 nm light in the upgraded slicer, the values in table 5.11 imply that the amount of aberrations introduced is making the spot size FWHM less than the unaberrated spot size. This result is perfectly acceptable because Gaussian functions are being used to model the vertically binned spot profiles and the FWHM does not equate to the full spot size width; a Gaussian has infinite extent but the aberrated spot image must have finite extent. For this reason the values presented in table 5.11 should be understood qualitatively, rather than quantitatively.

Comparing the aberration ratios in tables 5.11 and 5.7 it can be seen that the amount of aberrations introduced by the upgraded spectrograph and upgraded reflective slicer are much less. Even with a 33% estimated worst-case scenario for the reflective slicer the aberrations cause the spot size from the slicer to be less than the non-sliced beam in the upgraded spectrograph, with the exception of 900 nm light. This is indeed what is desired for the upgraded system.

Spectral Coherence Envelopes

As was performed in the updated simulation in section 5.2.4, the FWHM spot size from the upgraded spectrograph and the upgraded reflective slicer are used to generate the spectral coherence envelopes for the upgraded SD-OCT system. The envelope functions can be divided by one another to show an improvement factor in the signal as a function of imaging depth. A 33% increase in sliced spot size was used in order to model a worst-case scenario upgraded SD-OCT system. The values used for the spot widths are 25.125 μm for the non-sliced spectrograph and 13.7 μm for the sliced spectrograph. Also, Airy diameters of 17 μm and 21 μm were used. The resulting aberrated spot profile plots are shown in fig. 5.30, the coherence envelopes are shown in fig. 5.31(a), and the ratio showing the improvement factor is shown in fig. 5.31(b).

The maximum unaliased imaging depth has been increased from 3.767 mm to 4.273 mm because a longer focal length camera lens has been used and the wavelength separation, $\Delta\lambda$, between pixels has been decreased (see eqn. 4.3). Also to note that the aberrated pinhole spot profile for the sliced system is much narrower than the non-sliced system. The spectral coherence envelope for the sliced system is much broader than the non-sliced system indicating that an improvement in signal strength versus imaging depth will be seen with the sliced SD-OCT system. The ratio of the coherence envelopes shows that a very large improvement over the non-sliced SD-OCT system is observed. A 2.75X improvement

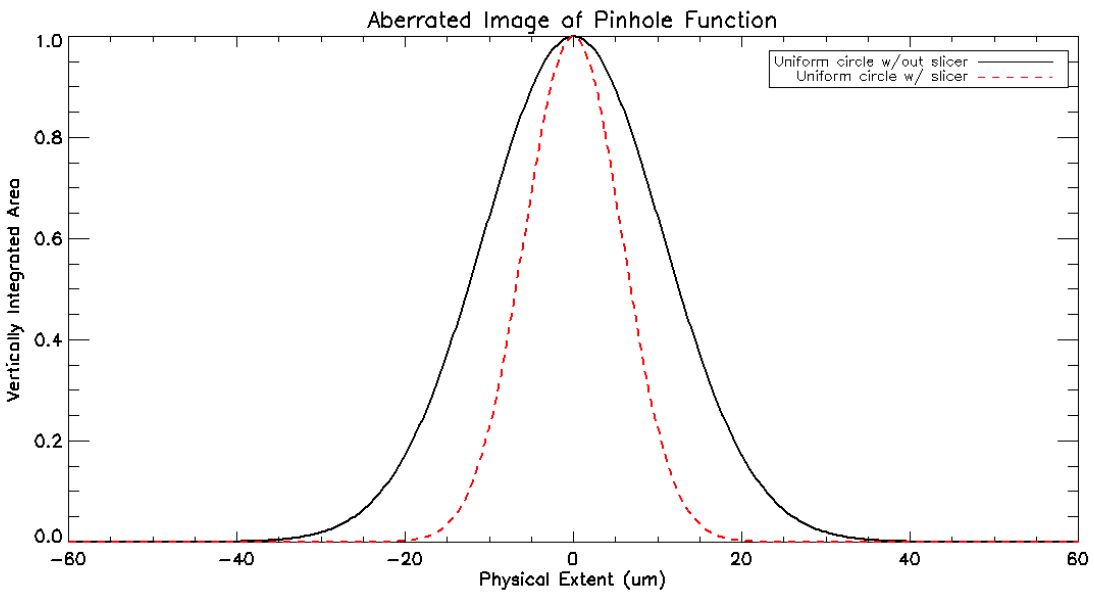

Figure 5.30: A plot showing the vertically integrated aberrated image of the pinhole on the camera focal plane. The pinhole is modelled as a uniform circular function. The plot shows the results for both without (black solid) and with (red dashed) a slicer in the system.

in fringe contrast at around 2.2 mm, a 7.0X improvement at around 3.1 mm, and at most a 42.6X improvement at the theoretical maximum unaliased imaging depth of 4.2 mm. Keep in mind is this all for physical delay in a vacuum, in a typical tissue with an index of 1.4 these distances become 1.57 mm, 2.21 mm, and 3.05 mm.

5.4 Design of the Diffraction Limited Reflective Slicer

The chromatic, spherical, and other higher order aberrations introduced by the optical elements in the refractive-based 2X slicer caused the focused spot size FWHM to be enlarged by 6-7 μm. In the custom spectrograph used to test the performance of the refractive slicer initially in section 4.4 the starting spot size was on the order of 50 μm, while as for the SD-OCT system the starting spot size is on the order of 10 μm. The amount of aberrations introduced by the refractive slicer in the SD-OCT system is about 50% of the desired focused spot size while in the testing spectrograph it is about 10%. In the former case the aberrations introduced are catastrophic to the system performance, while in the latter case the effects are barely significant. It is also worth mentioning that the Airy diameter in the SD-OCT system was on the order of 20 μm while for the testing spectrograph it was on the order of 14 μm. The aberrated spot shape is convolved with the Airy pattern

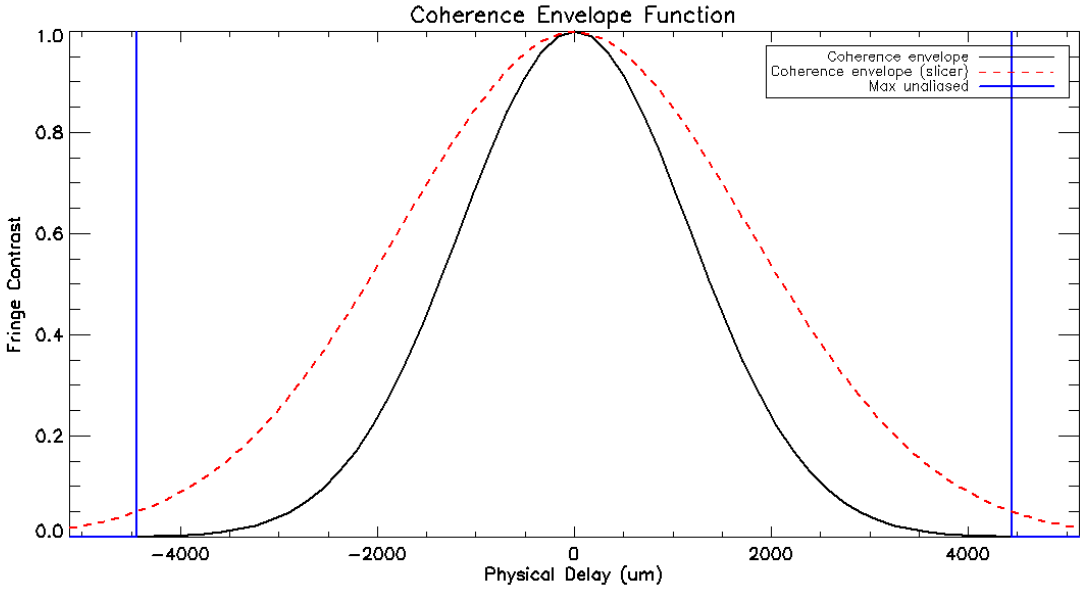

(a) Spectral Coherence Envelopes

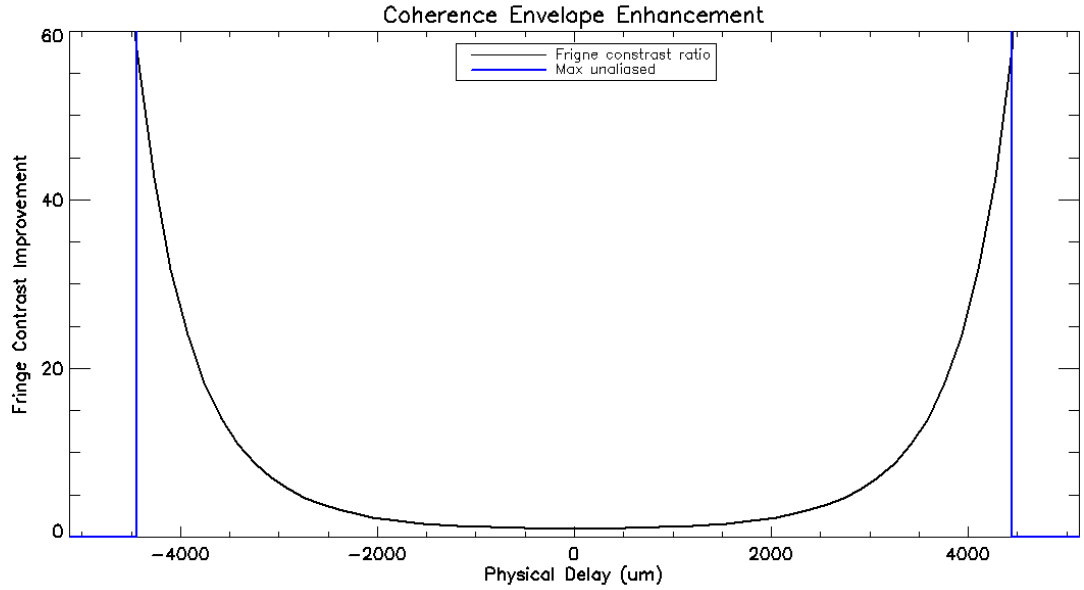

(b) Relative Fringe Contrast Ratio

Figure 5.31: (a) The non-sliced envelope is shown as solid black and the sliced envelope is shown as dashed red. (b) Ratio of coherence envelopes showing the effect of the upgraded slicer on the upgraded SD-OCT system.

so in a perfect slicer that reduces the width of the spot shape by a factor of 2X exactly, a factor of 2X in final focused spot width reduction is never truly realized. In the ideal case of on-axis 850 nm light the focused spot widths for before and after the 2X refractive slicer are 21.48 μm and 18.04 μm giving an ideal slicing factor of only 1.19X (see table 5.6). For the testing spectrograph the spot sizes FWHM were measured to be 81.6 μm and 40.8 μm giving a slicing factor of 2.00. Of course these measurements are FWHM, which may not be the best indicator for actual reduction factor, but FWHM measurements are typically the values that are performed in optical measurements and provide a standard metric. The Airy diameter for the SD-OCT system is larger than the desired spot width by nearly a factor of 2, while for the testing spectrograph it was only about 25%. The main conclusion of this analysis is that if a slicer is used to reduce the width of something that is close to the size of the diffraction limit then the working slicing factor (WSF) may be much less than the designed slicing factor. Furthermore, if the width of the spot is very small, then the aberrations introduced by the slicer may be a large percentage of the spot width and this will further reduce the WSF. In the case of the SD-OCT system both the spot size is on the order of the Airy diameter and the aberrations introduced by the slicer are a significant percentage of the spot width. In order to increase the WSF for the SD-OCT system the aberrations induced by the slicer have to be decreased significantly and a "diffraction limited" design needs to be employed.

The chromatic aberrations in the refractive slicer is quite significant. In order to eliminate the chromatic aberration an all reflective design may be employed. Reflective optical elements (mirrors) when used as lenses do not have a focal length that is dependent on wavelength. Recall from section 2.1.3 that the wavelength dependence on focal length is due to glass being a dispersive medium so the index of refraction is dependent on wavelength, and the focal length is dependent on the index of refraction. With a mirror the light is not travelling through any glass so there is no dispersion (except due to the air, which is minimal) and therefore no wavelength dependence on focal length.

One of the challenges of working with reflective lenses is that typically the light is obscured by other optical elements, as is the case for many reflective telescopes, or the light must enter off-axis. In the former case there is a significant loss of throughput as a trade-off for a straight line, on-axis design. In the latter case the throughput efficiency is very high but an off-axis design is complex and sometimes introduces more aberrations [27]. The goal of the newly designed diffraction limited slicer is to reduce the aberrations as much as possible without sacrificing much throughput. An on-axis design would be able to keep aberrations to a minimum, but would be too costly in terms of throughput, so an off-axis reflective design was chosen for the diffraction limited slicer.

The spherical and other higher order aberrations in the refractive slicer were also quite significant in addition to the chromatic aberrations. Similar aberrations would still be present in the reflective design if spherical surfaces are used for the lens elements. Recall

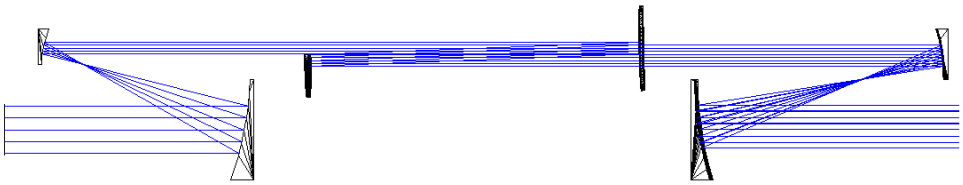

(a) Side View

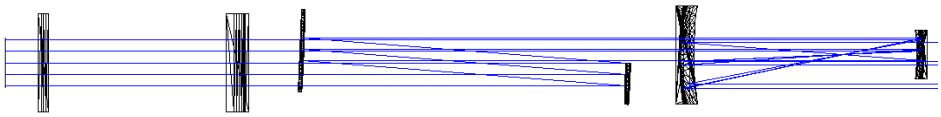

(b) Top view

Figure 5.32: The Zemax model of the 2X reflective slicer as shown from the top and side. Figure protected under United States patent [44].

from section 2.1.4 that spherical aberration is due to the surface of an optical element having spherical curvature, and that this aberration can be eliminated by using a parabolic surface instead. For a spherical surface the rays of light incident close to the centre of the optical element will come to a focus at a different point than the rays incident further away from the centre of the optical element. If the surface is parabolic then all the rays come to a focus at the same point.

Having reflective parabolic lenses is arguably one of the most ideal designs since there are no chromatic or spherical aberrations. However, using the elements off-axis still introduce other aberrations such as coma, astigmatism, field curvature, distortion, and so on. These higher order aberrations are still very small and ultimately result in the newly designed reflective slicer to be diffraction limited. The newly designed slicer employs a reflective off-axis parabolic set-up. The final design can be seen in fig. 5.32 and an annotated 3D representation is seen in fig. 5.33

The first two elements of the diffraction limited slicer serve as the beam compressor and are off-axis parabolic mirrors with curvature only in one dimension, hence they are dubbed off-axis parabolic cylindrical mirrors. The focal lengths, dimensions, and off-axis distances (OAD) are summarized in table 5.12. The incident light reflects off of the first mirror, CM1, and is focused to a line in-front and above the mirror. The second mirror, CM2, is placed above and in-front of mirror CM1 such that the focal planes coincide. The light from CM1 reflects collimated off of CM2 and continues along the same light input direction but sheared upwards. The compressor mirrors are oriented parallel to one another and centred about the input optical axis. This orientation makes it quite easy to construct in a final instrument since the mirrors can be specified by rectangular coordinates and 90°

angles. The orientation of the compressor mirrors are summarized in table 5.13.

The second two elements of the diffraction limited slicer are the pupil re-arranging mirrors, DM1 and DM2, that work in a similar manner to the mirrors in the refractive design (see section 4.3). The orientations of the re-arranging mirrors are summarized in table 5.13. The light after the re-arranging mirrors is centred slightly below and sheared slightly horizontally from the light before the re-arranging mirrors.

The last two elements of the diffraction limited slicer serve as the beam expander and are off-axis parabolic mirrors with curvature in both dimensions, hence they are circularly symmetric and simply called off-axis parabolic mirrors. The focal lengths, dimensions, and off-axis distances are summarized in table 5.12. The light emerging from the re-arranging mirrors is reflected off of the first expander mirror, EM1, that is sheared slightly horizontally. The reflected light is focused to a point below, in-front, and sheared horizontally from EM1. The light continues to diverge from the focal point and is reflected collimated off of the second expander mirror, EM2. The second expander mirror is oriented below, in-front, and sheared horizontally from EM1. The orientation of the expander mirrors are summarized in table 5.13. The horizontal shears of mirrors EM1 and EM2 cause the output collimated beam from the diffraction limited slicer to be centred with the same lateral coordinates as the input beam, i.e. input and output are the same location. This a highly desirable effect because it means the diffraction limited slicer can be integrated into a spectrograph a lot easier than any current slicer design. Also, the series effect of stacking slicers is more easily realized (see section 4.2).

The orientation and sizes of the focusing mirrors in the new slicer are designed so that all the mirrors may be specified with 90° angles and the bases of the mirrors lie on the same horizontal plane. This results in the construction of the slicer being quite simple since there are no tilted components in the system with the exception of the re-arranging mirrors, but that point is trivial.

A spot diagram of the off-axis parabolic slicer was produced in Zemax to demonstrate the diffraction limited off-axis performance. Perfect collimating and focusing lenses were used to model the spectrograph so the only aberrations introduced would be from the slicer. This is compared against a spot diagram produced in the same way but using the refractive slicer. Simulated images of the focused spots were also produced. The resulting spot diagrams are shown in fig. 5.35 and the simulated images are shown in fig. 5.34. The spot diagrams clearly show that the reflective slicer is diffraction limited while the refractive slicer has rays that focus well outside the Airy diameter, hence the off-axis parabolic reflective slicer is diffraction limited. The resulting simulated images shows that the reflective slicer produces a much cleaner spot profile than the refractive design.

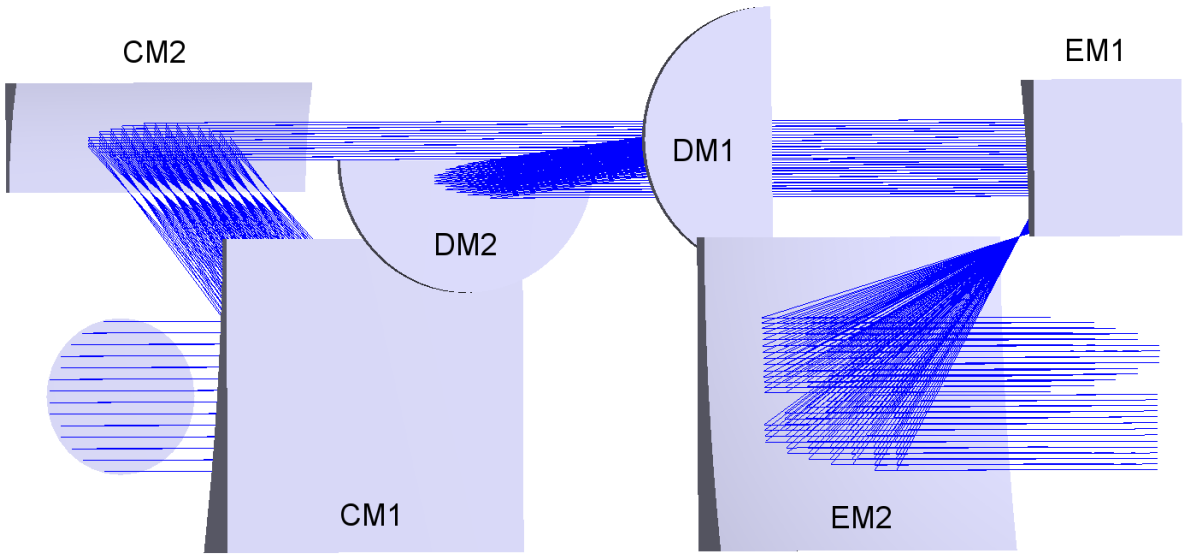

Figure 5.33: The Zemax model of the 2X reflective slicer shown as a 3D shaded model. Figure protected under United States patent [44].

Reflective Slicer Element Parameters				
Element	**FL (mm)**	**Width (mm)**	**Height (mm)**	**OAD (mm)**
CM1	50	30	30	4.5
CM2	12.5	30	10.5	0.0
DM1	∞	12.7	25.4	N/A
DM2	∞	25.4	12.7	N/A
EM1	25	15	15	0.0
EM2	50	30	30	0.0

Table 5.12: The focal lengths, widths, heights, and the off-axis distance of the individual elements in the reflective diffraction limited 2X slicer design. Information protected under United States patent [44].

Orientation of the Slicer Elements					
Element	**X (mm)**	**Y (mm)**	**Z (mm)**	**Tilt X**	**Tilt Y**
CM1	0.0	0.0	0.0	0.0	0.0
CM2	0.0	24.375	-62.5	0.0	0.0
DM1	0.0	24.375	15.0	-1.08°	-2.2°
DM2	3.75	22.5	115.0	-1.08°	-2.2°
EM1	2.5	22.5	200	0.0	0.0
EM2	1.25	0.0	125	0.0	0.0

Table 5.13: The locations of the elements in the reflective slicer. Measurements are referenced to the centre of CM1, which coincides with the centre of the input beam. All measurements are to the centre of the optical element except the re-arranging mirrors. The the measurement locations for DM1 and DM2 are the centre of the vertical straight edge. Information protected under United States patent [44].

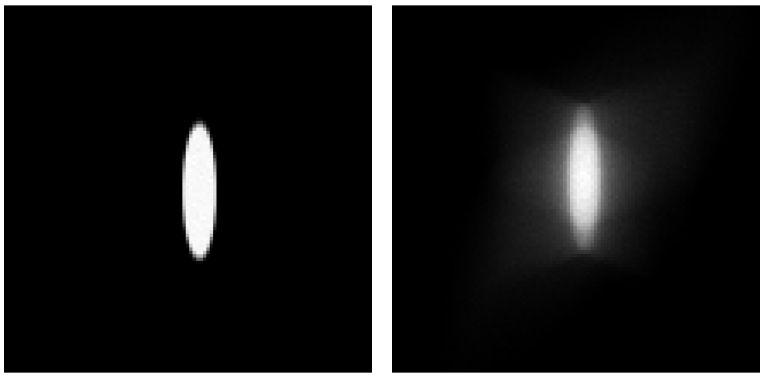

(a) Reflective Slicer (b) Refractive Slicer

Figure 5.34: The simulated images produced in Zemax for the reflective 2X slicer and the refractive 2X slicer. The wavelength is 850 nm and a 10 μm source diameter was used. Image simulation input parameters are taken from table 5.3.

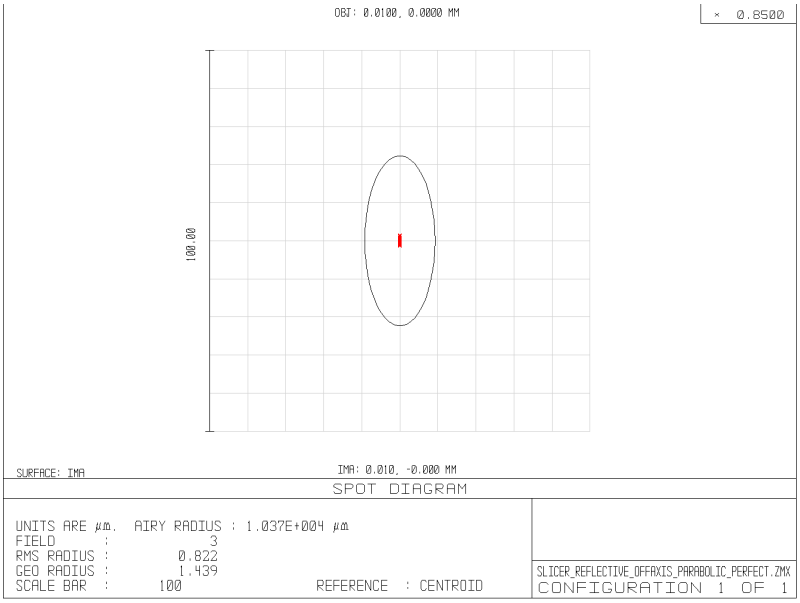

(a) Reflective Slicer

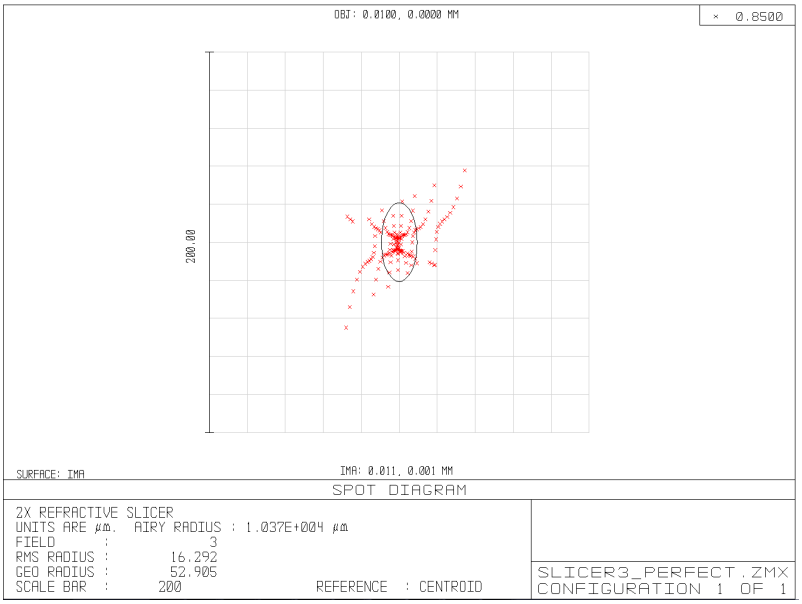

(b) Refractive Slicer

Figure 5.35: The spot diagrams produced in Zemax for the reflective 2X slicer and the refractive 2X slicer. The wavelength is 850 nm and a 10 μm source diameter was used.

Chapter 6

Conclusions

In chapter 3 the general theory of spectral domain optical coherence tomography (SD-OCT) was presented and the image signal was derived in eqn. 3.3. It was seen that the interference term gives rise to sinusoidal fringes across the spectrum where the frequency is dependent and proportional on the probe depth in a sample. The relative amplitude of the fringes is defined to be the visibility, and it was seen that the visibility decreases as the frequency of the fringes increases—this is due to the spectral coherence of the spectrograph. The function that describes the visibility decrease was presented in eqn. 3.5 and is is known as the spectral coherence envelope, and it depends on the wavelength separation between the pixels, $\Delta\lambda$, and the bandwidth per pixel, $\delta\lambda$, which is also the spectral resolution. The coherence envelope serves as the sensitivity for the SD-OCT system, which determines the signal-to-noise ratio of the OCT image.

A refractive-based optical pupil slicer with a design slicing factor of 2X was constructed and the performance was evaluated in chapter 4. It was shown that the slicer is able to reduce the spectral resolution, $\delta\lambda$ by a factor of 2.00, as measured by FWHM. The slicer is also able to maintain an 85.58% throughput efficiency. By definition of a spectrograph quality factor in eqn. 4.6 the slicer is able to increase the quality of a dispersive spectrograph by a factor of 1.7112.

The expected impact of the slicer in the SD-OCT system was initially modelled in IDL and the results were presented in the beginning of chapter 5. It was shown that the slicer could boost the sensitivity of the SD-OCT instrument by a factor of 5X at the maximum unaliased imaging depth of 3.7 mm and therefore provide an increase to the SNR of the OCT image. The resulting measurement of the spectral coherence envelopes of the SD-OCT system, both with and without the slicer, showed a worse than expected performance. The coherence envelope for the sliced SD-OCT system ended up showing a decrease in sensitivity because the amount of optical aberrations introduced by the slicer combined with the fact that the source image is about the same size as the diffraction

limited spot size, resulted in the fact that the slicer increased spot width. The increased spot width increases the spectral resolution and bandwidth per pixel, $\delta\lambda$, which was shown in eqn. 3.5 to have a negative impact on the SD-OCT signal sensitivity.

In section 5.3 two proposed upgrades to the SD-OCT system and the optical pupil slicer were presented. First, a complex lens system for the spectrograph focusing lens was shown to be required for good off-axis performance. This custom lens design uses three off-the-shelf lenses oriented in a telecentric image space configuration. While this design takes up a reasonable amount of space, it is cost-effective and easy to implement. The second upgrade proposed is a reflective-based diffraction-limited optical pupil slicer with a design slicing factor of 2X. This design offers superior optical performance compared to the refractive-based design, and is also easier to construct because all the components may be fixed in place specified with 90° angles. The expected results of the upgraded SD-OCT system spectrograph with the reflective slicer were modelled in IDL and sensitivity improvements on the order of 40X were shown.

6.1 List of Contributions

A list summarizing the unique contributions of this thesis are as follows:

- Presents results demonstrating that inducing additional delay in the reference arm of the SD-OCT system provides sensitivity depth selection and shows imaging depths beyond traditional standards of up to 3.3 mm (see fig. 3.6).
- Presents a useful metric, called the spectrograph quality factor, Q, that can aid in the design of dispersive spectrographs (see section 4.1).
- Provides an SD-OCT spectrograph simulation model to calculate the spectral coherence envelope (see section 5.1.1). This type of simulation model is not seen in the current literature.
- Presents an optical design of a refractive-based pupil slicer with a design slicing power of 2X (see section 4.3).
- Provides a unique alignment procedure for implementing a pupil slicer into an SD-OCT system by measurement of spectral beating (see section 5.2.1).
- Proposes an upgraded reflection-based diffraction-limited in-line optical design of a pupil slicer with a design slicing factor of 2X (see section 5.4).

6.2 Relevance to Other Fields

Historically slicers first appeared in the field of astronomy in order to boost the resolving power of spectrographs without sacrificing throughput. In astronomy light is extremely limited and telescope time is quite expensive therefore throughput is valued very high on astronomical instruments. The relevance of slicers in astronomy still holds today so presenting a unique optical design for a new kind of slicer is quite relevant to current astronomers.

The optical pupil slicer has value not only in SD-OCT, but in other dispersive spectroscopic based instruments as well. It was seen in chapter 4 that the optical pupil slicer can fundamentally improve the quality factor of dispersive-based spectrographs. Instruments and applications that are primarily limited based on the performance of the spectrograph typically demand high-resolution as well as high-speed. SD-OCT instruments used in ophthalmology typically fall into this category and researchers are attempting to boost the performance of these systems [12, 48]. Raman-based spectrographs are another excellent example where high-speed and high-resolution are needed–these systems would also benefit from an optical pupil slicer.

Perhaps one of the nicest features of the optical pupil slicer is that it operates in pupil-space as opposed to image-space, i.e. collimated light versus focused light. The entire optical pupil slicer can be modelled as a black-box that takes an input beam of a given diameter corresponding to a given focused spot width, and outputs a beam of roughly the same diameter that now corresponds with a spot width some factor smaller than the original—these factors may be upwards of several. Optical pupil slicers can easily and quickly be implemented in pre-existing spectrographs with minimal alterations to the system layout but provide improvements upwards of 200% or more. Optical pupil slicers may also be arranged in a series to provide a multiplicative effect on this improvement factor.

6.3 Future Work

The complete subject of optical pupil slicers in SD-OCT is not contained within the scope of this document, nor is all the work finished on the subject. This research has paved the way for identifying some of the pitfalls and limitations of optical pupil slicers in spectrographs already operating close to the diffraction limit. It was shown that the original design for the refractive 2X slicer was not good enough to provide an improvement in the particular SD-OCT system outlined in chapter 3; in fact it made the system perform worse. This result was not expected given the performance results of the 2X refractive slicer in a custom-built spectrograph presented in chapter 4, although the spectrograph was quite low performance

to begin with. The results of this research also have pioneered the topic of optical pupil slicers in SD-OCT instruments and provided useful methods of construction as such.

The reflective-based diffraction-limited in-line optical pupil slicer has never been built nor tested. This is a direction of future research that is essential to implement optical pupil slicers in pre-existing diffraction limited spectrographs.

There are numerous improvements that can be made to the SD-OCT system design, most notably in the spectrograph section of the instrument. A custom camera lens design was proposed, but has not been constructed and implemented. This upgrade is viewed as essential in lieu of the off-axis performance results of the current SD-OCT system spectrograph. A more complex custom camera lens, and even collimating lens, may be implemented also in order to reduce the aberrations introduced in the spectrograph.

The study of optical pupil slicers implemented into dispersive-based spectrographs in general could benefit from defining a performance characteristic region. In this research only two points in this region were shown. The first was when the image size was much larger than the diffraction limit (chapter 4), and the second was when the image size is about the same size as the diffraction limit (SD-OCT). The slicer was shown to perform well in the first region but poorly in the second region. An aberration analysis provided additional insight to these results. Extrapolating these results over a much more general parameter space taking into account various degrees of aberrations, diffraction limited spot sizes, and slicing factors can provide a useful engineering tool for implementing optical pupil slicers in any dispersive-based spectrograph.

APPENDICES

Appendix A

Derivation of the Maximum Unaliased Imaging Depth in SD-OCT

Consider the general OCT interference condition:

$$I(k) = I_r(k) + I_s(k) + 2\sqrt{I_r(k)I_s(k)}\cos(kd), \tag{A.1}$$

where k is the wavenumber, d is the optical path difference (OPD), I_r and I_s are the optical power spectra from the reference and the sample arm respectively. Consider the reference and sample arm to be completely known. The phase difference, $\Delta\phi$, at two difference sampled wave numbers is given by,

$$\Delta\phi = d(k_1 - k_2). \tag{A.2}$$

In taking the Fourier transform (FT) of the interference spectrum over a sample bandwidth, $\Delta\Lambda$, the separation between samples in the Fourier transform is given as $[1/\Delta\Lambda]$. If the spectrograph has J pixels then the domain in the FT goes from [0] to $[(J-1)/\Delta\Lambda]$. At each FT sample location the domain has units of cycles per bandwidth, $\Delta\Lambda$. A cycle is defined as a full 2π of phase. The minimal phase that can be distinguished between FT samples, $\delta\phi_{min}$ is given as the phase difference in the two extreme wavenumbers in the source, k_{max} and k_{min}. Using eqn. A.2 this minimal detectable phase difference per FT sample is given as,

$$\delta\phi_{min} = d(k_{max} - k_{min}). \tag{A.3}$$

The sampling units in the FT are given as,

$$\left[\frac{\delta\phi_{min}}{2\pi\Delta\Lambda}j\right], \tag{A.4}$$

where j is the sample number and has range [0] to $[J-1]$. Using the definition of wavenumber as $k = 2\pi/\lambda$, the sampling units in eqn. A.4 can be expressed as,

$$\left[\frac{\delta\phi_{min}}{2\pi\Delta\Lambda}j\right] = \left[\frac{d}{\lambda_0^2 - \frac{\Delta\Lambda^2}{4}}j\right], \tag{A.5}$$

where λ_0 is the central wavelength in the interference sample bandwidth. In order to express the FT sample units in terms of OPD, or d, eqn. A.5 must be solved for d so it is seen that samples have spacing given by

$$\lambda_0^2 - \frac{\Delta\Lambda^2}{4}. \tag{A.6}$$

As a reasonable approximation the second term in eqn. A.6 may be neglected and it is seen that the conversion from the FT sample space units to OPD is given by multiplying by the squared central wavelength in the sample band λ_0^2.

For a real interference spectrum collected with no phase information over J pixels, the FT is unable to distinguish between positive and negative frequencies. Due to Nyquist sampling criteria, the maximum number of cycles that can be detected unaliased with J pixels is $J/2$. This means that the unaliased imaging domain in the FT goes from $[(1-J)/2\Delta\Lambda]$ to $[J/2\Delta\Lambda]$. The maximum unaliased OPD can be solved by,

$$d_{max} = \frac{J}{2\Delta\Lambda}\left(\lambda_0^2 - \frac{\Delta\Lambda^2}{4}\right) \simeq \frac{J\lambda_0^2}{2\Delta\Lambda}. \tag{A.7}$$

As a reasonable approximation the wavelength separation between each pixel, $\Delta\lambda$, is equal to the sample bandwidth, $\Delta\Lambda$, divided by the number of pixels, J, i.e. $\Delta\lambda = \Delta\Lambda/J$. Using this relation the maximum OPD becomes

$$d_{max} = \frac{\lambda_0^2}{2\Delta\lambda}. \tag{A.8}$$

Since the OPD is twice the sample probe depth ($d = 2z$), eqn. A.8 can be expressed in terms of the maximum unaliased imaging depth in SD-OCT as,

$$z_{max} = \frac{\lambda_0^2}{4\Delta\lambda}. \tag{A.9}$$

Appendix B

Proof of the Wiener-Khintchine Theorem

We may define a complex random process in time as $z(t)$. The function may be said to be stationary if the random fluctuations in time, t, do not depend on the value of t, and hence the expectation value of $z(t)$ also does not depend on t, nor a coordinate shift. Mathematically this may be represented as

$$\langle z(t-t_0)\rangle_e = \langle z(t)\rangle_e = \int zPr(z,t)d^2z = \int zPr(z)d^2z. \tag{B.1}$$

The two-time autocorrelation function for $z(t)$ is defined as,

$$\Gamma(t_1,t_2) = \langle z^*(t_1)z(t_2)\rangle_e. \tag{B.2}$$

If $z(t)$ is a stationary process then we may induce a time coordinate shift of value $\tau = t_2 - t_1$, hence

$$\begin{aligned}\langle z^*(t_1)z(t_2)\rangle_e &= \int z_1^* z_2 Pr(z_2,t_2;z_1,t_1)d^2z_1d^2z_2 \\ &= \int z_1^* z_2 Pr(z_2,t+t_2-t_1;z_1,t)d^2z_1d^2z_2 \\ &= \langle z^*(t)z(t+t_2-t_1)\rangle_e = \Gamma(\tau).\end{aligned} \tag{B.3}$$

It is seen that the autocorrelation function is also independent of time, t.

If and ensemble average of a random process carries the same statistical information as a time average of a single ensemble, the random process is said to be ergodic. Simply, the time average is equal to the ensemble average–this is generally the case for optical fields.

Wiener showed that for a complex random process $z(t)$ the power spectrum may be given as [59],

$$S(\omega) = \frac{1}{2\pi} \int_{-\infty}^{\infty} \Gamma(\tau) \exp(i\omega\tau) d\tau, \tag{B.4}$$

where

$$\Gamma(\tau) = \langle z^*(t) z(t+\tau) \rangle_t. \tag{B.5}$$

We may define the Fourier transform of the complex random process $z(t)$ as $z(\omega)$. The ensemble average of $z^*(\omega)z(\omega')$ may be given as,

$$\langle z^*(\omega) z(\omega') \rangle_e = \frac{1}{4\pi^2} \iint_{-\infty}^{\infty} \langle z^*(t) z(t') \rangle_e \exp(i(\omega' t' - \omega t)) dt dt', \tag{B.6}$$

where eqn. B.6 is expressed as a Fourier transform. If the complex random process $z(t)$ is stationary then the two-time autocorrelation function inside the double integral is only dependent on time difference $\tau = t' - t$, i.e. $\Gamma(\tau) = \langle z^*(t) z(t') \rangle_e$. We may then express eqn. B.6 as

$$\begin{aligned} \langle z^*(\omega) z(\omega') \rangle_e &= \left[\frac{1}{2\pi} \int_{-\infty}^{\infty} \exp(i(\omega' - \omega)) dt \right] \left[\frac{1}{2\pi} \int_{-\infty}^{\infty} \Gamma(\tau) \exp(i\omega'\tau) d\tau \right] \\ &= \Gamma(\omega) \delta(\omega - \omega'). \end{aligned} \tag{B.7}$$

Furthermore if $z(t)$ is ergodic then the time and ensemble average are equal so the autocorrelation function is equal to the time average, i.e. $\Gamma(\tau) = \langle z^*(t) z(t') \rangle_t$. From Wiener's statement on the power spectrum expression (see eqns. B.4 and B.5) we see that $S(\omega) = \Gamma(\omega)$ and we may express the power spectrum of $z(t)$ as

$$S(\omega) = \frac{1}{2\pi} \int_{-\infty}^{\infty} \Gamma(\tau) \exp(i\omega\tau) d\tau. \tag{B.8}$$

Equation B.8 states that if a complex random process is stationary and ergodic then the power spectrum may be given as the Fourier transform of the autocorrelation of the random process, and its inverse statement also holds. Although we have followed the work of Wiener in this proof, a similar result was shown by Khintchine using a different approach a few years after Wiener, and hence the theorem is credited to both parties.

Bibliography

[1] Lenny Abbey. The Complete Amateur Astronomer: The Limits of Telescope Performance. `http://labbey.com/Articles/Limits/Limits.html` [2010, December 16]. 56

[2] P.E. Andersen, L. Thrane, H.T. Yura, A. Tycho, T.M. Jørgensen, and M.H. Frosz. Advanced modelling of optical coherence tomography systems. *Phys. Med. Biol.*, 49:1307–27, 2004. 40, 50

[3] I.K. Baldry, J. Bland-Hawthorn, and J.G. Robertson. Volume Phase Holographic Gratings: Polarization Properties and Diffraction Efficiency. *PASP*, 116:403–14, 2004. 22, 58

[4] Harrison H. Barrett and Kyle J. Myers. *Foundations of Image Science*. Wiler-Interscience: John Wiley & Sons, Inc., New York, New York, USA, 2004. 14, 17, 31, 68

[5] B. Behr, A.R. Hajian, A.T. Cenko, M. Murison, R.S. McMillan, R. Hindsley, and J. Meade. Stellar astrophysics with a dispersed Fourier transform spectrograph. I. Instrument description and orbits of single-lined spectroscopic binaries. *The Astrophysical Journal*, 705:543, 2009. 3

[6] Roy S. Berns. *Billmeyer and Saltzman's Principles of Color Technology*. John Wiley & Sons, Inc., New York, New York, USA, third edition, 2000. 55

[7] M.A. Bershady. 3D Spectroscopic Instrumentation. `http://adsabs.harvard.edu/abs/2009arXiv0910.0167` [2009, October]. 22, 58

[8] Max Born and Emil Wolf. *Principles of Optics*. Cambridge University Press, Cambridge, UK, seventh expanded edition, 1999. 8, 14, 17, 19, 21, 22, 42, 59, 60

[9] I.S. Bowen. The Image Slicer, a device for reducing loss of light at slit of stellar spectrograph. *ApJ*, 88:113–24, 1938. 66

[10] M.E. Brezinski, G.J. Tearney, S.A. Boppart, E.A. Swanson, J.F. Southern, and J.G. Fujimoto. Optical biopsy with optical coherence tomography: feasibility for surgical diagnostics. *J. of surgical research*, 71:32–40, 1997. 3

[11] A.T. Cenko. *Automatic Interferometic Alignment of an Optical Coherence Tomography System*. PhD thesis, University of Waterloo, Waterloo, Ontario, Canada, 2011. 46

[12] B. Cense and N.A. Nassif. Ultrahigh-resolution high-speed retinal imaging using spectral-domain optical coherence tomography. *Optics Express*, 12(11):2435–47, 2004. 3, 78, 133

[13] M.A. Choma, M.V. Sarunic, C. Yang, and J.A. Izatt. Sensitivity advantage of swept source and Fourier domain optical coherence tomography. *Optics Express*, 11(18):2183–9, 2003. 3, 34

[14] J.F. de Boer, B. Cense, B.H. Park, M.C. Pierce, G.J. Tearney, and B.E. Bouma. Improved signal-to-noise ratio in spectral-domain compared with time-domain optical coherence tomography. *Optics Letters*, 28(21):2067–9, 2003. 3, 34

[15] F. Diego. Confocal Image Slicer. *Applied Optics*, 32:6284–7, 1993. 67

[16] C. Dorrer, N. Belabas, J-P. Likforman, and M. Joffre. Spectral resolution and sampling issues in Fourier-transform spectral interferometry. *JOSA B*, 17:1795–1802, 2000. 38

[17] W. Drexler. Ultrahigh-resolution optical coherence tomography. *Journal of Biomedical Optics*, 9:47–74, 2004. 3

[18] Wolfgang Drexler and James G. Fujimoto, editors. *Optical Coherence Tomography - Technology and Applications*. Springer, New York, New York, USA, 2008. 1, 3, 34, 38, 40, 41, 50, 114

[19] D.J. Erskine. An externally dispersed interferometer prototype for sensitive radial velocimetry: theory and demonstration on sunlight. *PASP*, 115:255–69, 2003. 3

[20] D.J. Erskine and J. Ge. A prototype fringing spectrograph for sensitive extra-solar planet searches and astroseismology studies. *American Astronomical Society*, 31:837, 1999. 3

[21] D.J. Erskine and J. Ge. Novel interferometer spectrometer for sensitive stellar radial velocimetry. *APS Conference*, 195:501–7, 2000. 3

[22] A.F. Fercher, W. Drexler, C.K. Hitzenberger, and T. Lasser. Optical coherence tomography - principles and applications. *Rep. Prog. Phys.*, 66:239–303, 2003. 3, 34, 41

[23] A.F. Fercher, C.K. Hitzenberger, M. Sticker, and R. Zawadzki. Numerical dispersion compensation for partial coherence interferometry and optical coherence tomography. *Optics Express*, 9(11):610–5, 2001. 42, 93

[24] Richard P. Feynman. *QED: The Strange Theory of Light and Matter*. Princeton University Press, Princeton, New Jersey, USA, 1985. 21

[25] J.G. Fujimoto, M.E. Brezinski, G.J. Tearney, S.A. Boppart, B. Bouma, M.R. Hee, J.F. Southern, and E.A. Swanson. Optical biopsy and imaging using optical coherence tomography. *Nature Medicine*, 1:970–2, 1995. 3

[26] J.G. Fujimoto, C. Pitris, S.A. Boppart, and M.E. Brezinski. Optical coherence tomography: an emerging technology for biomedical imaging and optical biopsy. *Nature America: Neoplasia*, 2:9–25, 2000. 3

[27] Joseph M Geary. *Introduction to Lens Design With Practical ZEMAX® Examples*. Willmann-Bell, Inc., Richmond, Verginia, USA, 2002. 14, 115, 116, 117, 124

[28] Joseph W. Goodman. *Introduction to Fourier Optics*. Roberts & Company, Greenwood Village, Colorado, USA, third edition, 2005. 23, 24, 37, 42

[29] John E. Greivenkamp. *Field Guide to Geometrical Optics*. SPIE - The International Society for Optical Engineering, Bellingham, Washington, USA, 2004. 10, 11, 12, 18

[30] I. Grulkowski, M. Gora, M. Szkulmowski, I. Gorczynska, D. Szlag, S. Marcos, A. Kowalczyk, and M. Wojtkowski. Anterior segment imaging with Spectral OCT using a high-speed CMOS camera. *Optics Express*, 17(6):4842–58, 2009. 3

[31] A.R. Hajian. A high throughput modified FTS - a new direction in astronomical spectroscopy. *American Astronomical Society*, 30:859, 1998. 3

[32] A.R. Hajian, B.B. Behr, A.T. Cenko, R.P. Olling, D. Mozurkewich, J.T. Armstrong, B. Pohl, S. Petrossian, K.H. Knuth, R.B. Hindsley, M. Murison, M. Efroimsky, R. Dantowitz, M. Kozubal, D.G. Currie, T.E. Nordgren, C. Tycner, and R.S. McMillan. Initial results from the USNO dispersed Fourier transform spectrograph. *The Astrophysical Journal*, 661:616–33, 2007. 3

[33] A.R. Hajian and T.N. Nordgren. A New Instrument for Detecting Earth-Mass Planets. *USNO press release*, 1998. 3

[34] Roger F. Harrington. *Time-Harmonic Electromagnetic Fields*. John Wiley & Sons, Inc., New York, New York, USA, 2001. 19, 20

[35] G. Hausler and M.W. Linder. 'Coherence Radar' and 'Spectral Radar' - New Tools for Dermatological Diagnosis. *Journal of Biomedical Optics*, 3:21–31, 1998. 1, 34

[36] Thomas M. Haylock, Andrew T. Cenko, Lev M. Chifman, Peter B. Christensen, Farnoud Kazemdadeh, Arsen R. Hajian, Jan Hendrikse, and Jeff T. Meade. Positioning System for High Resolution Tissue Imaging. *Proc. SPIE*, 7890, 2011. 47

[37] ITT. IDL Homepage. `http://www.idl-envi.com/idl-home`. 79

[38] S-W. Lee, H-W. Jeong, Y-C. Ahn, W. Jung, Z. Chen, and B-M. Kim. Axial resolution and depth range of high-resolution spectral domain optical coherence tomography at 1.3μm. *Proc. of SPIE*, 7168, 2009. 1, 34

[39] R. Leitgeb, C.K. Hitzenberger, and A.F. Fercher. Performance of Fourier domain vs. time domain optical coherence tomography. *Optics Express*, 11(8):889–94, 2003. 1, 3, 34

[40] Lodish, Berk, Kaiser, Krieger, Scott, Bretscher, Ploegh, and Matsudaira. *Molecular Cell Biology*. W.H. Freeman and Company, New York, New York, USA, sixth edition, 2008. 2

[41] Leonard Mandel and Emil Wolf. *Optical Coherence and Quantum Optics*. Cambridge University Press, Cambridge, UK, 1995. 21, 25, 26, 27, 28

[42] Jeff T. Meade, Bradford B. Behr, Andrew T. Cenko, Peter Christensen, Arsen R. Hajian, Jan Hendrikse, and Frederic D. Sweeney. Fundamental Performance Improvement to Dispersive Spectrograph Based Imaging Technologies. *Proc. SPIE*, 7890, 2011. 71

[43] Jeff T. Meade, Andrew T. Cenko, Arsen R. Hajian, and Jae K. Kim. Apparatus and Methods for Optical Coherence Tomography and Confocal Microscopy. International Application No. PCT/US2010/001598, 2010. 77

[44] Jeff T. Meade, Arsen R. Hajian, Bradford B. Behr, and Andrew T. Cenko. Optical Slicer for Improving the Spectral Resolution of a Dispersive Spectrograph. United States Provisional Application No. 61/350,264, 2010. 69, 70, 125, 127, 128

[45] F.T. Nguyen, A.M. Zysk, E.J. Chaney, J.G. Kotynek, U.J. Oliphant, F.J. Bellafiore, K.M. Rowland, P.A. Johnson, and S.A. Boppart. Intraoperative evaluation of breast tumor margins with optical coherence tomography. *Cancer Research*, 69:8790–6, 2009. 3

[46] Optics and Biomedical Engineering Laboratory (OBEL). Introduction to oct. `http://obel.ee.uwa.edu.au/research/oct/intro/` [2010, December 16]. 2

[47] Christopher Palmer and Erwin Loewen. *Diffraction Grating Handbook*. Newport Corporation, Rochester, New York, USA, sixth edition, 2005. 22, 23, 59

[48] B. Potsaid, I. Gorczynska, V.J. Srinivasan, Y. Chen, J. Jiang, A. Cable, and J.G. Fujimoto. Ultrahigh speed Spectral/Fourier domain OCT ophthalmic imaging at 70,000 to 312,500 axial scans per second. *Optics Express*, 16(19):15149–69, 2008. 3, 78, 133

[49] S.A. Prahl, M. Keijzer, S.L. Jacques, and A.J. Welch. A Monte Carlo Model of Light Propagation in Tissue. *SPIE Inst. Ser.*, IS 5:102–11, 1989. 30, 43, 50

[50] Yu. Ralchenko, A.E. Kramida, J. Reader, and NIST ASD Team. NIST Atomic Spectra Database (ver. 4.0.1), [Online]. `http://physics.nist.gov/asd` [2010, November 22]. 73

[51] J.W. Severinghaus and Y. Honda. History of Blood Gas Analysis. VII. Pulse Oximetry. *J. Clin. Monit.*, 3:135–8, 1987. 54

[52] H. Suto and H. Takami. Waveguide Image Slicer. *Applied Optics*, 36:4582–6, 1997. 67

[53] N.C. Thomas. The Early History of Spectroscopy. *J. Chem. Educ.*, 68(8):631–4, 1991. 64

[54] L. Thrane, H.T. Yura, and P.E. Andersen. Calculation of the maximum obtainable probing depth of optical coherence tomography in tissue. *Proc. of SPIE*, 3915, 2000. 40, 43, 50, 53

[55] P.H. Tomlins and R.K. Wang. Theory, developments and applications of optical coherence tomography. *J. Phys. D: Appl. Phys.*, 38:2519–35, 2005. 1

[56] T. Walraven and J.H. Walraven. Some features of the Leiden radial velocity instrument. *Proc. of the Conf. on Aux. Instr. for Large Telescopes*, 1972. 66

[57] Lihong V. Wang and Hsin i Wu. *Biomedical Optics - Principles and Imaging*. John Wiley & Sons Inc., Hoboken, New Jersey, USA, 2007. 29, 30, 43

[58] G. Wiedermann, D.E. Jennings, R.H. Hanel, V.G. Kunde, S.H. Moseley, G. Lamb, M.D. Petroff, and M.G. Stapelbroek. Postdispersion system for astronomical observations with Fourier transform spectrometers in the thermal infrared. *Applied Optics*, 28:189–45, 1989. 3

[59] Norbert Wiener. Generalized Harmonic Analysis. *Acta Mathematica*, 55:117–258, 1930. 140

[60] M. Wojtkowski, V.J. Srinivasan, T.H. Ko, J.G. Fujimoto, A. Kowalczyk, and J.S. Duker. Ultrahigh-resolution, high-speed, fourier domain optical coherence tomography and methods for dispersion compensation. *Optics Express*, 12(11):2404–22, 2004. 42, 93

[61] Emil Wolf. *Introduction to the Theory of Coherence and Polarization of Light*. Cambridge University Press, Cambridge, UK, 2007. 25, 26, 27

[62] W.H. Wollaston. A Method of examining refractive and dispersive Powers, by prismatic Reflection. *Phil. Trans. Roy. Soc. Lond.*, 92:365–80, 1802. 64

[63] S.H. Yun, G.J. Tearney, B.E. Bouma, B.H. Park, and J.F. deBoer. High-speed spectral-domain optical coherence tomography at 1.3μm wavelength. *Optics Express*, 11:3598–604, 2003. 1, 38

[64] ZEMAX® Development Corporation, Bellevue, Washington, USA. *ZEMAX® Optical Design Program User's Manual*, April 2010. 11, 100, 105